THE VARIATION OF CLIMATE SENSITIVE TIDAL OCEAN-DYNAMO SIGNALS ON SUB-DECADAL AND SEASONAL TIME SCALES

Kumulative Dissertation
zur Erlangung des Doktorgrades
"doctor rerum naturalium"
(Dr. rer. nat.)

eingereicht am Fachbereich Geowissenschaften
der Freien Universität Berlin
im November 2021

vorgelegt von JOHANNES PETEREIT

Johannes Petereit: *The variation of climate sensitive tidal ocean-dynamo signals on sub-decadal and seasonal time scales*

1. GUTACHTER: Prof. Dr. rer. nat. Maik Thomas
2. GUTACHTER: Prof. Dr. rer. nat. Claudia Stolle

DISPUTATION: 9. Februar 2022

It always seems impossible until it's done.

— Nelson Mandela

ABSTRACT

Motional induction describes the induction of electric currents through charged particles moving perpendicular to an ambient magnetic field. A well-known device that uses motional induction to induce electric currents is the bicycle dynamo. The induction of electric currents in the ocean due to the motion of saltwater within the ambient geomagnetic field is, by contrast, lesser-known; this phenomenon is called the ocean-dynamo effect which indicates the similarity of both phenomena. The electromagnetic field signals emitted by ocean-dynamo induced electric currents are primarily sensitive to three factors: 1. the number of moving charged particles, 2. the magnetic field strength of the ambient field, and 3. the velocity with which the particles move perpendicular to said magnetic field.

The amount of electrically charged particles in the seawater, a saline solution, is measured with the electrical seawater conductivity σ. σ is determined by the saline solution's chemical equilibrium, which in return is predominantly defined by the physical properties of seawater temperature and salinity. Thus, changes in the spatial distribution of seawater temperature and salinity cause changes in the spatial distribution of electrical seawater conductivity, which in return affect the ocean-dynamo signals. In theory, ocean-dynamo signals are therefore suitable for ocean observation applications.

Out of all ocean-induced electromagnetic signals, signals induced by ocean tides play a unique role. The signatures of the periodic tidal flow are the only ocean-dynamo signals that have been successfully observed in magnetometer observations, space-borne and land-based. In addition to the proven measurability, the signals are also modelled with sufficient accuracy so that, on a global scale, observed tidal ocean-dynamo signatures agree well with model predictions. These two preconditions allow for an investigation of the relationship between ocean dynamics and tidal ocean-dynamo signals, a much-needed advancement towards practical ocean observation applications. In the past, sensitivity studies of tidal ocean-dynamo signals have focused mainly on changes on long time scales. By contrast, the present cumulative thesis examines the influence of ocean dynamics on tidal ocean-dynamo signals on short and intermediate time scales. In par-

ticular, it investigates the mechanisms and effects of ocean dynamics and recent seawater temperature and salinity changes on tidal ocean-dynamo signals. Furthermore, it investigates the detectability and measurability of short-term variations of said signals in magnetometer observations.

Out of the presented three research studies, the first is a model-based characterization of tidal ocean-dynamo amplitude variations attributed to the El Niño/Southern Oscillation (ENSO). The study shows that tidal ocean-dynamo signal changes precede the onset of warm and cold ENSO phases and attributes these findings to the underlying oceanic processes. Furthermore, the study provides an assessment of the measurability of ENSO-induced tidal ocean-dynamo amplitude variations. The second study covers a time series analysis of modeled tidal ocean-dynamo amplitudes on a global scale. Here, the amplitudes were modeled based on existing oceanic seawater temperature and salinity observations. Based on the analysis of the underlying in-situ data, the study assesses recent developments in signal amplitudes to resolve a conflict between existing model-based sensitivity studies. Furthermore, the study identifies the heightened sensitivity of coastal tidal ocean-dynamo signals and provides a physical explanation for this fact. The third study focuses on local ocean phenomena and analyses time series of coastal island magnetometer observations. It presents evidence for seasonal amplitude variations and trends in amplitudes and phases of tidal ocean-dynamo signals.

The advancements in the field contribute to the transition from retrospective or model-based analysis to an actual inference of the oceanic temperature and salinity dynamics from magnetometer observations.

KURZFASSUNG

Die Induktion elektrischer Ströme durch geladene Teilchen, welche sich senkrecht zu einem sie umgebenden Magnetfeld bewegen, wird als Bewegungsinduktion bezeichnet. Eine bekannte Anwendung des zugrunde liegenden Wirkprinzip der Bewegungsinduktion ist der Fahrraddynamo. Weniger bekannt ist dagegen die Induktion elektrischer Ströme im Ozean durch den Fluss des salzigen Meerwasser innerhalb des Erdmagnetfelds; wegen der Ähnlichkeit zum Fahrraddynamo wird dieses Phänomen auch als Ozeandynamo-Effekt bezeichnet. Im Allgemeinen gilt: elektrische Ströme strahlen elektromagnetische Felder ab. Die elektromagnetischen Signale, die von den durch den Ozeandynamo induzierten elektrischen Strömen ausgesendet werden, hängen vor allem von drei Faktoren ab: 1. die Anzahl der sich bewegenden geladenen Teilchen, 2. die Magnetfeldstärke des Umgebungsfeldes und 3. die Geschwindigkeit, mit der sich die Teilchen senkrecht zum Magnetfeld bewegen.

Die elektrische Leitfähigkeit des Meerwassers ist ein Maß für die Menge der geladenen Teilchen in der Salzlösung. Die elektrische Leitfähigkeit des Meerwassers wird durch das chemische Gleichgewicht der Salzlösung bestimmt, welches wiederum in erster Linie durch die physikalischen Eigenschaften Meerwassertemperatur und -salzgehalt bestimmt wird. Veränderungen in der räumlichen Verteilung dieser physikalischen Größen führen also zu Veränderungen in der räumlichen Verteilung der elektrischen Leitfähigkeit des Meerwassers, was sich wiederum auf die Ozeandynamosignale auswirkt. Theoretisch eignen sich die Ozeandynamosignale daher für die Fernerkundung des Ozeans.

Von allen ozeaninduzierten elektromagnetischen Signalen spielen die von den Gezeiten induzierten Signale eine besondere Rolle. Die Signatur des periodischen Gezeitenstroms ist das einzige Ozeandynamosignal, das erfolgreich aus in Daten von satellitengestützten und terrestrischen Magnetometerbeobachtungen identifiziert wurde. Zusätzlich zur erwiesenen Messbarkeit können die Signale auch mit ausreichender Genauigkeit modelliert werden, so dass, global betrachtet, die beobachteten Gezeitensignaturen des Ozeandynamos gut mit ihren Modellvorhersagen übereinstimmen. Diese beiden Voraussetzungen ermöglichen eine Untersuchung der

Beziehung zwischen der Ozeandynamik und den Signalen des Gezeitendynamos, ein dringend benötigter Schritt auf dem Weg zur praktischen Ozeanbeobachtung mittels dieser Signale. In der Vergangenheit haben sich Sensitivitätsstudien von Gezeitendynamosignalen hauptsächlich auf Veränderungen auf langen Zeitskalen konzentriert. Im Gegensatz dazu wird in der vorliegenden kumulativen Dissertation der Einfluss der Ozeandynamik auf Gezeitendynamosignale auf kurzen und mittleren Zeitskalen untersucht. Sie untersucht die Mechanismen und Auswirkungen der Ozeandynamik und der jüngsten Änderungen der Meerwassertemperatur und des Salzgehalts auf die Signale des Gezeitendynamos. Darüber hinaus wird die Detektierbarkeit und Messbarkeit von Schwankungen dieser Signale auf kurzen Zeitskalen in Magnetometerbeobachtungen untersucht.

Von den drei vorgestellten Forschungsstudien ist die erste eine modellbasierte Charakterisierung der Amplitudenschwankungen des Gezeitendynamos, welche sich auf natürliche Temperatur- und Salzgehaltvariationen aufgrund der El Niño/Southern Oscillation (ENSO) zurückführen lassen. Die Studie zeigt, dass die Veränderungen der Gezeitendynamosignale dem Einsetzen von warmen und kalten ENSO-Phasen vorausgehen, und führt diese Ergebnisse auf die zugrunde liegenden ozeanischen Prozesse zurück. Darüber hinaus liefert die Studie eine Bewertung der Messbarkeit von Amplitudenschwankungen gezeiteninduzierter Ozeandynamosignale. Die zweite Studie befasst sich, auf globaler Skala, mit einer Zeitreihenanalyse modellierter Gezeitendynamo-Amplituden. In der Studie wurden Amplituden auf der Grundlage vorhandener Beobachtungen von Temperatur und Salzgehalt des Meerwassers modelliert. Aufgrund der zugrundeliegenden In-situ-Daten bewertet die Studie die jüngsten Entwicklungen bei den Signalamplituden, um einen Konflikt zwischen bestehenden modellbasierten Sensitivitätsstudien zu lösen. Darüber hinaus zeigt die Studie die erhöhte Empfindlichkeit von Signalen des Gezeitendynamos in Küstengebieten auf und liefert eine physikalische Erklärung für diese Tatsache. Die dritte Studie konzentriert sich auf lokale Ozeanphänomene und analysiert Zeitreihen von Magnetometerbeobachtungen an Inselküsten. Sie liefert Beweise für jahreszeitliche Amplitudenschwankungen und Trends in den Amplituden und Phasen von Gezeitendynamosignalen.

Die gemachten Fortschritte tragen zum Übergang von der retrospektiven oder modellbasierten Analyse zu einer tatsächlichen Ableitung der ozeanischen Temperatur- und Salzgehaltsdynamik aus Magnetometerbeobachtungen bei.

PUBLICATIONS

The present dissertation is comprised of the research results of the following publications and data releases.

Articles

Petereit, J., J. Saynisch-Wagner, C. Irrgang, and M. Thomas (2019a). "Analysis of Ocean Tide-Induced Magnetic Fields Derived From Oceanic In Situ Observations: Climate Trends and the Remarkable Sensitivity of Shelf Regions." In: *Journal of Geophysical Research: Oceans* 124.11, pp. 8257–8270. DOI: 10.1029/2018JC014768.

Contribution of Johannes Petereit to article:

- Co-conception of the study together with J. Saynisch-Wagner and C. Irrgang
- Updating the computation pipeline of Petereit et al. 2018 to provide an increased grid resolution and correct handling of coastal regions
- Analysis, visualization, interpretation and discussion of resulting data
- Writing, editing and updating the complete manuscript with correctional feedback from all co-authors

.

Petereit, J., J. Saynisch, C. Irrgang, T. Weber, and M. Thomas (2018). "Electromagnetic characteristics of ENSO." In: *Ocean Science* 14.3, pp. 515–524. DOI: 10.5194/os-14-515-2018.

Contribution of Johannes Petereit to article:

- Co-Conception of the study together with J. Saynisch and C. Irrgang
- Complete implementation of the EM-modelling pipeline using the provided oceanic input data of T. Weber
- Analysis, visualization, interpretation and discussion of the resulting data

- Writing, editing and updating the complete manuscript with correctional feedback from all co-authors

.

Petereit, P., J. Saynisch-Wagner, A. Morschhauser, L. Pick, and Thomas. M. (2021). "On Temporal Variations of Coastal Tidal Ocean-Dynamo Signals." In: *Earth, Planet and Space*. submitted

Contribution of Johannes Petereit to article:

- Leading the conception of the study together with all co-authors
- Implementing the automated pipeline for downloading, screening and preprocessing of magnetometer data
- Analysis, visualization, interpretation and discussion of results
- Writing, editing and updating the complete manuscript with correctional feedback from all co-authors

.

Rigaud, R., M. Kruglyakov, A. Kuvshinov, K. J. Pinheiro, J. Petereit, J. Matzka, and E. Marshalko (2021). "Exploring effects in tippers at island geomagnetic observatories due to realistic depth- and time-varying oceanic electrical conductivity." In: *Earth, Planets and Space* 73.3. DOI: 10.1186/s40623-020-01339-3.

Contribution of Johannes Petereit to article:

- Providing the underlying timeseries of 3D ocean conductivity data and expertise about its creation process

.

Sachl, L., Z. Martinec, J. Velímský, C. Irrgang, J. Petereit, J. Saynisch, D. Einspigel, and N. R. Schnepf (2019). "Modelling of electromagnetic signatures of global ocean circulation: physical approximations and numerical issues." In: *Earth, Planets and Space* 71.1, p. 58. DOI: 10.1186/s40623-019-1033-7.

Contribution of Johannes Petereit to article:

- Co-conception of the study together with all co-authors
- Computing results using the provided input data for study cases with varying complexity

.

Saynisch-Wagner, J., J. Petereit, C. Irrgang, and M. Thomas (2020). "Phase Changes of Electromagnetic Oceanic Tidal Signals." In: *Journal of Geophysical Research: Oceans* 125.4. e2019JC015960 10.1029/2019JC015960, e2019JC015960. DOI: https://doi.org/10.1029/2019JC015960.

Contribution of Johannes Petereit to article:

- Adopting the modelling infrastructure of Petereit et al. (2019a) and computing EM results based on the provided experimental design instructions

.

Saynisch, J., J. Petereit, C. Irrgang, A. Kuvshinov, and M. Thomas (2016). "Impact of climate variability on the tidal oceanic magnetic signal - A model-based sensitivity study." In: *Journal of Geophysical Research: Oceans* 121.8, pp. 5931–5941.

Contribution of Johannes Petereit to article:

- Computing EM results using the provided input data

.

Saynisch, J., J. Petereit, C. Irrgang, and M. Thomas (2017). "Impact of oceanic warming on electromagnetic oceanic tidal signals: A CMIP5 climate model-based sensitivity study." In: *Geophysical Research Letters* 44.10, pp. 4994–5000.

Contribution of Johannes Petereit to article:

- Computing EM results using the provided input data

.

Datasets

Petereit, J., J. Saynisch, C. Irrgang, and M. Thomas (2019b). *Monthly complex amplitudes of global M2 ocean tide induced electromagnetic field signals from 1990 to 2016. V. 1.0*. DOI: 10.5880/GFZ.1.3.2019.001.

Contribution of Johannes Petereit to article:

- Setup of the computational pipeline and subsequent computation
- Documentation and publication

.

CONTENTS

Part I

Foundation

1

MOTIVATION — LINKING OCEAN OBSERVATION AND TIDAL OCEAN-DYNAMO SIGNALS

The importance and complexity of the impact the ocean has on our lives are easy to misjudge. For example, the ocean is the main source of water vapor, a greenhouse gas, in the atmosphere which influences our weather and climate (Cline, 1991; Mitchell, 1989) and plays a crucial role in tropical cyclone formation (Emanuel, 2018). The ocean also captures and stores heat which is redistributed predominantly from the equatorial region to the poles (Bryden et al., 2001; Ferrari et al., 2011; Macdonald et al., 2013). Without the ocean, Earth would barely be habitable.

Additionally, the ocean played a significant role in life's evolution on Earth and still is the habitat of a plethora of species, many of which are of economic or nutritional value to a vast number of people (Cochran et al., 2019). The ocean impacts life on Earth in miscellaneous ways and a better understanding of the ocean will lead to a more accurate estimation of how its role is impacted by the effects of the ongoing man-made climate changes, e.g. sea-level rise (Pugh et al., 2014), increase in ocean heat content (Abraham et al., 2013) or the ongoing acidification of the ocean (Tilbrook et al., 2019).

Ocean dynamics are non-linear, i.e. small influences have an ever-growing impact on the entire dynamical system with time. An extensive understanding of the evolution of ocean dynamics with time and the subsequent influence on global climate formation will only become attainable with sufficient observation and modelling capacities. Unfortunately, the deficit in available ocean in-situ observations is still large (Ocean Studies Board, 2000).

Fortunately, spatial and temporal coverage of ocean observations is ever-increasing. Nevertheless, the huge extent of the ocean in all three dimensions, extreme conditions like high pressure, aggressive salinity or its opacity for electromagnetic waves make it laborious and expensive to collect in-situ observations. Furthermore, point and linewise observations like those obtained from Argo floats (Roemmich et al., 2009), drifters or towed and moored buoys (e.g. the TAO/TRITON, PIRATA or RAMA program), can

observe only a tiny fraction of the ocean at once. With satellite observations (e.g. the satellite missions of Jason 1-3, GRACE, CHAMP or Swarm), it is possible to obtain two-dimensional images of the ocean. Satellite altimetry for example allows for the observation of sea-level rise (Pugh et al., 2014), surface currents (Phillips, 1963) or the temporal variation of oceanic tides (Egbert et al., 1994). A relatively new technique to observe oceanic seawater temperature and salinity variations and therefore the impact of climate change on the ocean (Irrgang et al., 2019; Saynisch et al., 2016, 2017) utilizes magnetic field observations.

The flow of seawater in the ocean drives an electromagnetic induction process whose resulting electromagnetic currents emit measurable electromagnetic field signals. The underlying physical principle is called motional induction and describes the interaction of moving charged particles, e.g. seawater, within an ambient magnetic field such as Earth's core field (c.f. chapter 2.1). Out of the various causes for seawater movements, tidal ocean currents are the only ocean phenomenon whose magnetic field signal has been successfully extracted from terrestrial (Maus et al., 2004; Schnepf et al., 2014, 2018) and space-borne magnetometer observations (Sabaka et al., 2016, 2015; Tyler et al., 2003). Tidal ocean currents unite fast large-scale seawater movements inducing relatively strong magnetic field signals ($\mathcal{O}(10^0$ nT)) with a predictable periodic regularity. This allows for both reliable modelling (Thomas, 2002) and prediction, and for frequency filtering of magnetometer observations. In theory, the observation of changes in the magnetic field amplitudes and phases allows conclusions to be drawn about changes in the induction process predominantly attributed to changes in the electrical seawater conductivity.

The thesis at hand advances the interdisciplinary field of ocean observations through tidal ocean-dynamo signals (TODS). It investigates the effect of changes in seawater temperature and salinity distributions on tidal ocean-dynamo signals on short and intermediate time scales and evaluates the quality of existing extraction techniques. To achieve this goal, the thesis is structured into three parts. Part I comprises the scientific foundation of the thesis. It presents the underlying physical and oceanographic phenomena that guide the presented arguments. Additionally, Part I gives an overview of the present state of research in the field, it carves out open questions that have motivated the scientific advancements presented in the second part (Part II). Since the presented dissertation is a cumulative thesis, part II presents the scientific advancements in the form of already pub-

lished or submitted scientific papers. The publications are aggregated into a holistic body of knowledge with linking chapters that clarify implications and the relation of the individual publications towards each other. The final part (Part III) summarizes the advances in the field to draw conclusions and bring the implications into the context of the existing body of knowledge to motivate further scientific advances.

2

SCIENTIFIC BACKGROUND

Chapter Summary

This chapter provides the necessary scientific background knowledge about electromagnetic induction processes to explain the formation of tidal ocean-dynamo signals as well as its characteristics. Furthermore, it reviews the characteristic three-dimensional spatial signal distribution. Based on these two aspect, variations in signal amplitudes, due to various influencing factors, are identified and compared to each other. The comparison motivates the upcoming studies and helps to place their findings in a larger context. The chapter concludes with a section on the characterization of tidal ocean-dynamo signals in comparison to other existing magnetic field signals. When extracting tidal ocean dynamo signals, additional magnetic field signals have to be taken into consideration.

2.1 EMERGENCE OF TIDAL OCEAN-DYNAMO SIGNALS (TODS)

For a profound understanding of the characteristics of tidal ocean-dynamo signals, it is necessary to examine the underlying processes that lead to the induction of electric currents in the ocean. There are two fundamental principles responsible for the induction of electric currents: motional induction and magnetic induction. Motional induction describes the induction of electric currents through the interaction of moving charge carriers within an ambient magnetic field and can be explained with the effect of the Lorentz force. Motional induction is the working principle of generators and dynamos which transform kinetic energy into electricity. The name ocean-dynamo indicates the similarity to the dynamo principle. However, there are some fundamental differences. Since seawater is a saline solution rich in free charge carriers in the form of salt ions, the ocean-dynamo is driven by said ions instead of electrons which are driving the dynamo effect in metal coil spinning generators. In the presence of the external magnetic field of Earth's core, all oceanic transport processes causing seawater movements

induce electric currents. The second induction mechanism, the magnetic induction, induces currents in electrically conducting media by flux density changes of the ambient magnetic field. In the ocean, this mechanism induces electric currents through naturally occurring temporal variations of external magnetic fields. Examples of phenomena that induce electric currents in the ocean through magnetic induction are processes in the ionosphere (e.g. solar quiet (SQ) variation, polar and equatorial electro jets) and magnetosphere (e.g. solar storms) (Kuvshinov, 2008). Both mechanisms will here be treated separately to focus the argumentation and to illustrate how the tide induced electric currents emerge. However, please note that both are essentially two expressions of the same underlying physical principle and can be unified with the help of Einstein's special relativity (Griffiths, 2005).

A general definition for electric currents is the transport of charge carriers. The movement of seawater and therefore salt ions qualifies as a stream of charged particles. The resulting electric current however is zero. The electric currents of positive and negative ions moving into the same direction cancel each other out since the integrated charge of seawater is zero. This changes when considering the principles of motional induction. The Lorentz Force acts on charge carriers with the charge q and can be described as:

$$\vec{F}_{\text{Lorentz}} = \vec{F}_{\text{E}} + \vec{F}_{\text{M}} = q \cdot \vec{E} + q \cdot \left(\vec{v} \times \vec{B} \right). \tag{2.1}$$

Here, $\vec{F}_{\text{E}}$ describes the electric force imposed by an external electric field $\vec{E}$. $\vec{F}_{\text{M}}$ describes the magnetic force, the force caused by a charge carrier moving with the velocity $\vec{v}$ within an ambient magnetic field $\vec{B}$. An effect of the Lorentz force which can also be deduced from its mathematical description is that positive and negative salt ions moving into the same direction are deflected into different directions (cf. figure 2.1). The consequence is the induction of a non-zero electric current.

The initial induction of electric currents is the first step in the process of generating measurable electromagnetic fields through these currents. The complete description of electrodynamics and the coupling of electric currents and their accompanying electromagnetic fields can only be achieved with the help of both Maxwell's equations and the Lorentz force (Griffiths, 2005; Jackson, 2009).

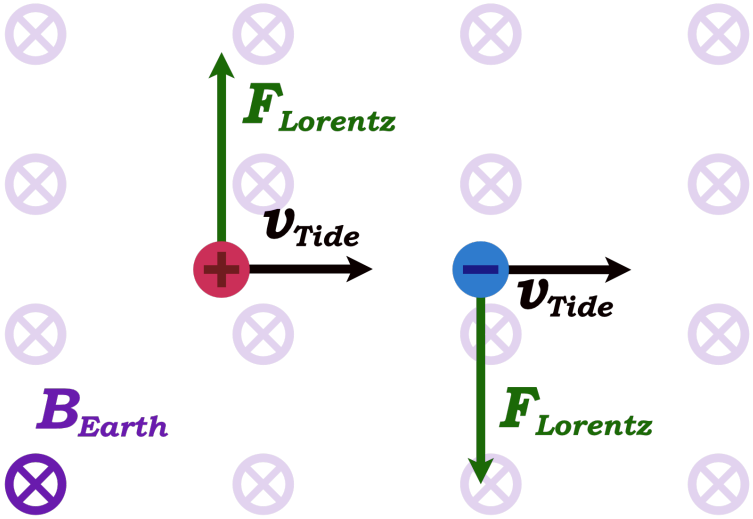

Figure 2.1: Schematic visualization of the magnetic force (a part of the Lorentz force) breaking the symmetry of negative and positive charge carriers that are moved by tidal currents through the ambient magnetic field of Earth's core (Orientation: facing into the paper plane). This process leads to the induction of electric currents which emits measurable electromagnetic field signals.

$$
\begin{aligned}
&\text{1. Ampère's circuital law} && \vec{\nabla} \times \vec{B} = \mu_0 \left(\vec{j} + \epsilon_0 \frac{\partial \vec{E}}{\partial t} \right) \\
&\text{2. Maxwell-Faraday equation} && \vec{\nabla} \times \vec{E} = -\frac{\partial \vec{B}}{\partial t} \\
&\text{3. Gauss's flux theorem} && \vec{\nabla} \cdot \vec{E} = \frac{\rho}{\epsilon_0} \\
&\text{4. Gauss's law for magnetism} && \vec{\nabla} \cdot \vec{B} = 0
\end{aligned}
\tag{2.2}
$$

From Maxwell's equations follows that motional induced electric currents emit EM fields whose field strength is proportional to its current strength.

The signal strength of these EM fields is inversely proportional to the distance to the source ($1/r^2$). One consequence is that the detectability of motionally induced signals in the ocean depends on the spatial scale of the induced electric current. Signals of slow seawater movements on a large-scale and fast movements on a small-scale can generate comparably strong signals. However, only large-scale signals will be measurable in space. For example, the signals of Tsunamis and ocean tides generate signals of a few

nanotesla at sea level. But, when measured in space, the small-scale signals of Tsunamis reach only a signal strength of 0.2 nT while the large-scale TODS and ocean circulation signals still achieve signals strengths of up to 2 nT locally.

An additional aspect in the generation of TODS is the fact that the induced EM fields cause secondary effects due to their interaction with the charged particle. This leads to the generation of secondary EM fields. A mathematical description of these phenomena is provided in the field of magnetohydrodynamics which studies the interaction of electrodynamic and hydrodynamic effects in electrically conducting fluids such as plasma, liquid metals or salt solutions. In principle, magnetohydrodynamics are also relevant in the formation of ocean-dynamo fields. However, in contrast to the internal processes of stars or the Earth's core, in case of the ocean-dynamo the Lorentz force is much smaller than the flow forces. Consequently, its influence can be neglected in the macroscopic view of the ocean. However, without modelling the interaction of the induced EM fields with the electrical conducting environment like the sediments in Earth's surface layers, it is not possible to model TODS correctly. The interaction of the electrical conducting environment and the EM signals also leads to secondary induced electric currents and modulates the measured EM signals in dependence of the conductivity of the surrounding material (Kuvshinov et al., 2002). Mathematically this is described with the EM induction equation:

$$\frac{\partial \vec{B}}{\partial t} = \vec{\nabla} \times \left(\vec{v} \times \vec{B} \right) - \frac{1}{\mu_0 \sigma} \vec{\nabla} \times \left(\vec{\nabla} \times \vec{B} \right), \tag{2.3}$$

where $\vec{B}$ is the magnetic field, $\vec{v}$ the velocity of a moving conductor, μ_0 the permeability of the free space, a natural constant, and σ the electrical conductivity. The EM induction equation can be derived using a generalized form of Ohms law for moving conductors in superposed $\vec{E}$ and $\vec{B}$ fields that are hence subjected to Lorentz Force ((2.1)):

$$\vec{J} = \sigma \left(\vec{E} + \vec{v} \times \vec{B} \right) \tag{2.4}$$

($\vec{J}$ is the current density), and the Maxwell-Faraday equation:

$$\vec{\nabla} \times \vec{E} = -\frac{\partial \vec{B}}{\partial t}. \tag{2.5}$$

An in-depth derivation of equation (2.3) can be found in Irrgang (2017) or Lorrain et al. (2006). For the general 3-D case, there is no analytical solution to the induction equation. It can therefore only be solved numerically. Motivated by this necessity, different approaches have been developed (cf. section 3.1).

In a nutshell, the transport of seawater within the ambient magnetic field of Earth's core induces electric currents. These electric currents emit electromagnetic fields which, in return, interact with the electromagnetic environment. The resulting electromagnetic signals are called ocean-dynamo signals. Tidal ocean-dynamo signals possess unique characteristics which are not found in signals induced by other ocean transports. These characteristics can be attributed to their source, the ocean tides. Ocean tides are one of the best-understood phenomena to the present day. They are one of the only phenomena that can be predicted well into the future within a reasonable margin of uncertainty. One reason for this is the near perfect knowledge of the motion of the Sun and the Moon. Another is the availability of data which originates from tide gauges or altimetric satellite missions. One characteristic feature of ocean tides is the regularity in time and their well-known tidal frequencies. These frequencies are imposed by the orbits of the Moon and the Sun with respect to Earth. Since these orbits are elliptical and the axes of rotation are angled towards each other, there are periodic changes in distances of the celestial bodies relative to each other. The strength of the tidal forces changes accordingly. As a consequence, the resulting temporal behaviour of sea level or tidal current strength deviates significantly from a regular sine wave which would occur in the case of constant tidal forces acting on a rotating planet. However, the temporal behaviour can be described with a set of sine waves on differing frequencies which are known as partial tides (Doodson, 1928). Magnetic field measurements show consequently significant tidal peaks at the frequencies related to the partial tides. In addition to their regularity, ocean tides are also robust in time. The propagation of tidal waves across the Earth is impeded by the continents. This leads to the formation of standing waves in the oceans. Due to the rotation of the Earth, the standing waves are influenced by the Coriolis force which leads to the creation of a system of rotating tidal waves, the amphidromic system (Pugh et al., 2014). It has been shown that the amphidromic system and resulting non-coastal tidal amplitudes are relatively robust in time despite rising sea levels (Saynisch et al., 2016). Both characteristics, the regular periodicity of their signals on well-known tidal

frequencies and their robustness, are inherited by TODS. However, TODS amplitudes experience additional variations caused by changes in seawater temperature and salinity variations which create a unique opportunity for ocean observation purposes.

2.2 SPATIAL CHARACTERIZATION OF TIDAL OCEAN-DYNAMO SIGNAL AMPLITUDES

The former section explains the general mechanism of the emergence of TODS as a result of the interaction between the the geomagnetic field, the ocean tide induced magnetic field and the electrical conducting environment. The general mechanism alone however is insufficient to provide an understanding to TODS specific aspects that will be discussed in upcoming chapters. One example is: When reviewing the global radial TODS amplitude distribution (cf. figure 5.1), why is there no pronounced large scale minimum at the South Atlantic Anomaly (SAA) (Heirtzler, 2002; Pavón-Carrasco et al., 2016), where the total geomagnetic field strength plummets (cf. figure 5.1), but a minimum along the geomagnetic equator, where the radial geomagnetic field changes its direction? Another example: Why are the following studies solely focusing on the radial magnetic TODS amplitude component? To give answers to these questions, TODS need to be further characterized in their three-dimensional extension. This entails mainly two aspects: (1) the distinct characteristics of TODS components after they have been decomposed into poloidal and toroidal components and (2) the effect of the characteristic tidal ocean wave velocity distribution on source current density $\vec{J}$ inducing TODS and hence the resulting signal.

Many of the findings of the afore mentioned magnetic TOD field components is based on the work of Chave (1983). He extended the work of PRICE (1950) and Weaver (1971) by examining the case where the forcing source, the electrical tidal ocean-dynamo current, is formulated explicitly. Using the Helmholtz decomposition, he orthogonally divided the inducing electric current into the components that are the source of two distinct modes of the resulting magnetic field. These are called the poloidal and the toroidal mode (PM and TM). The Helmholtz decomposition uses the fact that all magnetic field lines form closed loops which makes the vector field divergence free. Magnetic fields form consequently a torus around the inducing electric current. The qualities of said torus are the namesake for the two mentioned modes. As a side note, in older literature poloidal and

toroidal modes may also be referred to as *solutions of first and second kind* (PRICE, 1950), or *E and B polarization modes* (J. Larsen, 1973; Preisendorfer et al., 1974).

Both, the TM and PM are a result of charges carrier moved by the ocean transport. But, the orientation of the ocean transport in space defines the resulting mode. Since both modes are induced by orthogonally oriented electric current components; the modes are also distributed dissimilar in space (cf. figure 2.2. Additionally, they also differ in their physical properties such as the sensitivity towards ocean flow velocities and and its gradients, or the electrical conductivity of the surrounding media. The TM on one side, which is induced by electric currents in the vertical direction, is highly sensitive to the gradient of ocean flow velocities (Chave, 1983) and the electrical conductivity distribution of the lithosphere (Dostal et al., 2012). With these properties, the TM would in principle be a suitable signal to investigate both properties, if the TM would not vanish at sea surface and could hence only be detected directly inside the ocean. In theory the TM is indirectly observable via secondary PM at the ocean continent boarder (c.f. figure 2.2). The PM, which is induced by electric currents in the horizontal plane, on the other side is more sensitive to the depth integrated electrical conductivity weighted ocean velocities than the gradient of ocean flow velocities (Sanford, 1971). This is not least a consequence of the fact that the inducing horizontal currents are less impacted by conductivity variations. The electrical conductivity is highly sensitive to the seawater temperature (cf. section 2.4) and varies thus, comparing the scales of ocean extension in depth and width, more in vertical than in horizontal direction. Furthermore, the PM is less sensitive to the radial conductivity distribution below the ocean layer. This fact justified early thin sheet approximation approaches for modelling TODS. However, these approaches underestimate the influence of the spatial conductivity distribution, especially on a global scale (Sanford, 1971). Furthermore, in an idealized medium with a uniform conductivity distribution, the toroidal and poloidal modes exist independent from each other. In spite of this, in a realistic inhomogeneous medium both modes are coupled dynamically.

The reason, why the following studies, but also a large fraction of TODS research literature, focuses on the radial magnetic field component, is the fact that the PM, in contrast to the TM, permeates into the atmosphere and beyond. The PM is thus directly measurable using spaceborne and terrestrial observation techniques, e.g. satellites and terrestrial observatories.

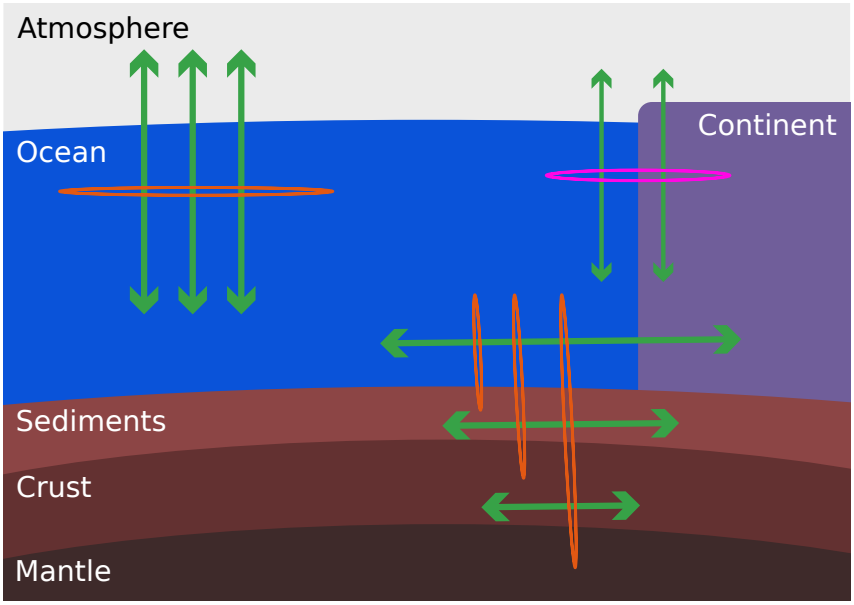

Figure 2.2: Schematic vizualisation of the toroidal and poloidal modes of ocean-induced magnetic fields. The primary poloidal magnetic fields (vertical green arrows) are induced by horizontal electric currents inside the ocean (horizontal red ellipse). The primary toroidal magnetic fields (horizontal green arrows) is induced by vertical electric currents which are not only contained in the ocean but can also reach deep down into the solid earth (vertical red ellipse). Said toroidal field also induces secondary currents in the boundary between the ocean and the continents or the ocean and the continental shelf (horizontal magenta ellipse). These induced currents are an effect of the abrupt change in conductivity between two regimes and induce secondary poloidal magnetic fields (vertical green arrows).

The second aspect, that needs to be discussed, are the consequences of the characteristics of the the spatial distribution vertical and horizontal tidal ocean velocities. Rotating tidal ocean waves cause mainly a horizontal flow and the vertical component is comparatively small. The values of the velocities in both directions express hence in general different orders of magnitudes. Equation (2.4) provides a suitable framework to investigate the consequences of this for the resulting TODS.

When taking into account the lack of an external electric field $\vec{E}$, the electric current induced by the tidal ocean-dynamo the equation can be formulated as:

$$\vec{J}_{\text{Tide}} = \sigma_{\text{Water}} \left(\vec{v}_{\text{Tide}} \times \vec{B}_{\text{Earth}} \right) . \tag{2.6}$$

The equation describes how the electrical conducting seawater σ_{Water} moved by the tides with a tidal velocity $\vec{v}_{\text{Tide}}$ within the ambient magnetic field of

Earth's core $\vec{B}_{\text{Earth}}$ creates an electric current with the current density $\vec{J}_{\text{Tide}}$. The three-dimensional velocity vector can be formulated as:

$$\vec{v}_{\text{Tide}} = \begin{pmatrix} v_{\text{Tide},\varphi} \\ v_{\text{Tide},\vartheta} \\ v_{\text{Tide},r} \end{pmatrix}, \tag{2.7}$$

with its horizontal components $v_{\text{Tide},\varphi}$ and $v_{\text{Tide},\vartheta}$, and the radial or vertical component $v_{\text{Tide},r}$. Horizontal velocities are much larger as vertical velocities, or mathematically $v_{\text{Tide},r} \ll v_{\text{Tide},\varphi}$ and $v_r \ll v_{\text{Tide},\vartheta}$. In first order, $v_{\text{Tide},r}$ can hence also be assumed as zero ($v_{\text{Tide},r} = 0$) which leads to the following simplification of equation (2.6):

$$\begin{aligned} \vec{J}_{\text{Tide}} &= \sigma_{\text{Water}} \cdot \begin{pmatrix} v_{\text{Tide},\varphi} \\ v_{\text{Tide},\vartheta} v_\theta \\ 0 \end{pmatrix} \times \begin{pmatrix} B_{\text{Earth},\varphi} \\ B_{\text{Earth},\vartheta} \\ B_{\text{Earth},r} \end{pmatrix} \\ &= \sigma_{\text{Water}} \cdot \begin{pmatrix} v_{\text{Tide},\varphi} B_{\text{Earth},r} \\ -v_{\text{Tide},\vartheta} B_{\text{Earth},r} \\ v_{\text{Tide},\vartheta} B_{\text{Earth},\varphi} - v_{\text{Tide},\varphi} B_{\text{Earth},\vartheta} \end{pmatrix}. \end{aligned} \tag{2.8}$$

Examining equation (2.8) shows that the current density $\vec{J}_{\text{Tide}}$ depends in horizontal direction only on one geomagnetic field component, the radial magnetic field component $B_{\text{Earth},r}$. Considering the fact that the PM, the only mode directly observable outside of the ocean, is induced by the horizontal $\vec{J}_{\text{tide}}$ component, it becomes clear, why the radial magnetic TODS show a minimum at the geomagnetic equator but not where the SAA is found.

2.3 PROCESSES IMPACTING TIDAL OCEAN-DYNAMO SIGNAL AMPLITUDES

Tidal ocean-dynamo signal amplitudes vary over time. To draw conclusions about the underlying causes for this temporal, two things are needed: A profound understanding of the signal formation process and the understanding of processes modulating TODS. As indicated in sections 2.1 and 2.2, amplitudes and phases of standing tidal waves in the amphidromic

system. They are thus determined by the geometry of the ocean basin. This means that the amplitudes of tidal waves depend on the bathymetry of the ocean basin and the sea level (Wright et al., 1999). Both change with time. However, in the open ocean, it has been found that changes in the bathymetry or sea level leading to significant alterations in the tidal system occur on centennial or even longer time scales. For this reason, tidal amplitudes and phases in the open ocean are assumed to be robust with regards to their naturally occurring variation. In shallow ocean regions however, amplitude variations of partial tides, e.g. the principal lunar tide M2, become significant on seasonal time scales (Müller et al., 2014). This case will be further discussed in chapter 6. Factoring out shallow ocean regions, causes for temporal TODS amplitude variations can be limited to two factors: changes in the electrical seawater conductivity σ_{Water} and the secular variation of Earth's core field $\vec{B}_{\text{Earth}}$. Both change with time but these changes usually happen on different time scales. Geomagnetic field variations are comparably slow; their impact on tidal ocean dynamo signals becomes significant on decadal time scales. Changes in the spatial distribution of σ_{Water} are typically faster and dominate therefore temporal TODS amplitude variation on short timescales.

The study of TODS and their variation will thus help to assess spatial σ_{Water}-distributions and their variations on short time scales. The standard approach to obtain this data is to take local measurements of σ and seawater temperature. This is usually done to gain knowledge of the local salinity which is determined from existing numerical approximations (Apel, 1987; IOC et al., 2010). However, the study on the electrical conductivity has gained interest over the last decade (Irrgang et al., 2016b; Trossman et al., 2019; Tyler et al., 2017). Evidence suggests that its vertical distribution is less dependent on the geographical location than the vertical salinity distribution (Zheng et al., 2018). By providing new electrical seawater conductivity data, this promotes the research on electrical seawater conductivity itself.

Moreover, since σ is defined through seawater salinity S, temperature T and pressure p (cf. figure 2.3), changes in those quantities will also impact TODS amplitudes. Especially, since σ_{Water}-variations can be primarily attributed to temperature variations (Saynisch et al., 2017). This means that the effects of climate change, such as ocean warming, the effects of changes in the ocean current system and the resulting effect on the oceanic heat distribution become observable. Likewise, there are well-known seawater

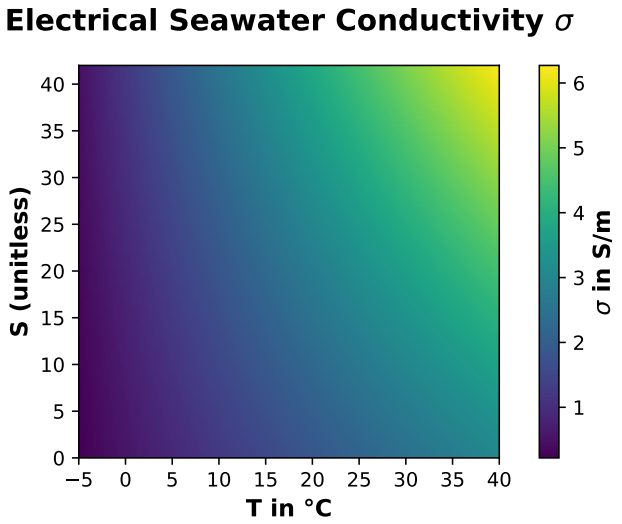

Figure 2.3: Heatmap of electrical seawater conductivity σ values at sea surface (p = 0 dbar). The parameter space reflects on the naturally occurring seawater temperature (T from -4°C to 40°C) and salinity (S from 0 to 42) values.

temperature anomalies associated with the seasonal variations, ENSO, the Atlantic Multidecadal Variability (Ba et al., 2014) or phenomena like the Pacific warm or the Atlantic cold 'blob' (Liang et al., 2017).

2.4 COMPOSITION OF NATURAL MAGNETIC FIELD SIGNALS AND THE DETECTION OF TIDAL OCEAN DYNAMO SIGNALS

Despite the good understanding of the processes leading to the formation of TODS and the modulation of their amplitudes, the extraction of TODS from magnetometer observations is challenging. That is because magnetic field measurements integrate, by their nature, many magnetic field signals simultaneously. Consequently, signals of naturally occurring magnetic field sources like the magnetic field of Earth's core, the static magnetic fields of the lithosphere, induction processes occurring in the ionosphere, the ocean, and the magnetosphere, are combined into one integrated signal. Separating these signals, whose strengths cover multiple orders of magnitude (geomagnetic field: $\mathcal{O}(10^5$ nT); TODS: $\mathcal{O}(10^0$ nT)), is possible when factoring in their individual temporal behaviour.

A valuable advantage for TODS signal detection is the possibility to filter magnetic field observations for the well-known tidal frequencies. This is one of the reasons why TODS have been successfully observed in the past

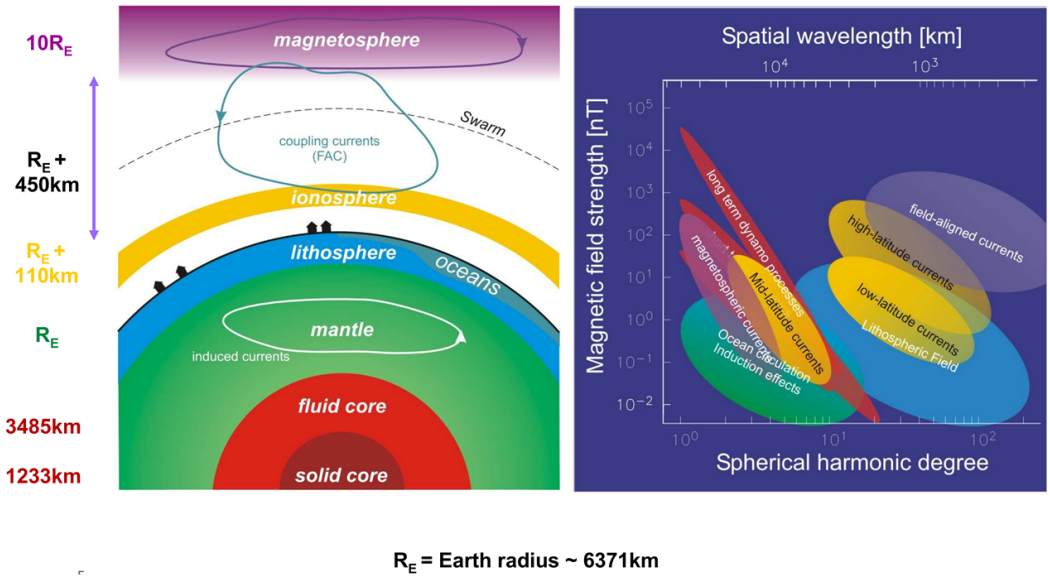

Figure 2.4: Overview of sources of magnetic field contributions (left) and characterization of the individual magnetic fields regarding field strength and spatial wavelength (right). The image is adapted from Haagmans et al., 2012, ESA

and the irregular signals of the general ocean circulation have not. They cannot be filtered for fixed frequencies (Irrgang, 2017). However, this approach has its limitations because TODS and signals of ionospheric induction processes share mutual frequency ranges (cf. figure 2.4), a challenge that needs to be addressed when extracting TODS from magnetic field observations. These ionospheric signals originate, for example, from electric currents induced by rising tidal waves in the ionosphere or the daily non-sinusoidal signal of the Equatorial Electrojet (EEJ) or the Solar-Quiet (Sq) variation. The strengths of the tidal ionospheric dynamo signals reach values of 10-30% of the oceanic counterpart (Malin, 1970; Schnepf et al., 2014). By contrast, the signals of the EEJ and Sq are in the order of several tens of nano teslas (nT) and consequently one order of magnitude larger than TODS. A source for additional variability is the sun spot-cycle which impacts ionospheric signals unlike oceanic signals (Sabine, 1857). These signals and their variations cannot be separated unambiguously by frequency filtering alone.

One approach to address this challenge is to separate magnetic field data into daytime and nighttime data upon analysis. During the night, the conductivity of the relevant part of the ionosphere decreases to 1/30th of the day side value, so that there is a distinguishable difference between day and night side measurements of the magnetic field. This difference was

historically exploited by the so-called Chapman-Miller extraction method (Chapman et al., 1940) which is based on an assumed ionospheric conductivity minimum at midnight (Malin, 1970). Today, the separation of night and day side data is achieved by means of local time or solar elevation angle (Kelley, 2009). However, depending on the geographical location, there are still residual signals of ionospheric processes, such as the Electrojets, which also contaminate the night data (Maus et al., 2004).

Another aspect that must be taken into account when analysing TODS is that data processing approaches and expected signal strengths depend significantly on the measuring site. One reason for this is the dependency of disturbing signals on the geographic location. The shielding effect of Earth's core field weakens external signals. However, this shielding effect is weakened at the geomagnetic equator were the vertical component of the core field reaches its minimum. There, the influence of disturbing signals becomes larger. Additionally, signals of local phenomena like the equatorial or polar electrojets need to be considered only in certain regions of the Earth. Those effects increase the complexity of the necessary data processing. Another aspect is a significant difference in TODS strength when measured inside or outside of the ocean. All magnetic field lines are self-contained. Magnetic fields are thus divergence free. Based on this property, it is possible to decompose magnetic ocean-dynamo signals into poloidal and toroidal field components using the Helmholtz decomposition (Chave, 1983; Chave et al., 1990; Jin, 2015) (cf. section 2.2). Unlike toroidal fields, poloidal fields are measurable outside of the ocean in the downward facing z-component of the magnetic field. However, poloidal fields have been shown, when induced by ocean circulations such as the Antarctic Circumpolar Current, to be affected by ocean-contained toroidal fields in terms of amplitude and seasonal variation (Velímský et al., 2019).

3

KNOWLEDGE GAP

Chapter Summary

This chapter is divided into two complementing sections. The first section reviews the existing body of literature to demonstrate the relevance of the subsequent studies in chapters 4 to 6 by placing them in context with the existing body of knowledge. Based on this review, the second section defines the investigated knowledge gap and states the specific aims of the present thesis in conjunction with the structured approach on how these aims are tried to be achieved.

3.1 PRESENT STATE OF RESEARCH

The field of electromagnetic field signals generated through motional induction processes in the ocean started with the a theoretical treatise by Michael Faraday in 1832 (Faraday, 1832). The attempted experimental validation of his own hypothesis however failed; he was unable to measure signals exceeding the noise level. The first experimental validation of tide induced electromagnetic field signals was achieved in 1851 by Wollaston (1881) and the first scientific report of a successful measurement was authored by Adams (1881). Both authors analyzed the signals of telegraph cables grounded in the ocean or coastal proximity.

Since the first experimental proof, the field of ocean-dynamo induced EM signals has been ever-growing and split into three main branches. These branches focus on the type of seawater flow generating motional induced electric currents in the ocean. These are EM fields induced through (1) Tsunamis, (2) general ocean circulation and (3) tides. There are also publications deviating from the mainstream which investigate signals from a passing Eddy (Lilley et al., 1993), swells (Lilley et al., 2004) or the effect of Hurricane Francis on the upper ocean (Sanford et al., 2011, 2007).

The research field of Tsunami generated EM signals has emerged after said signals have been successfully modelled (Kuvshinov, 2008) and measured (Toh et al., 2011). The analysis of the temporal development of the

EM signal revealed that part of its signature has the potential to be used for an early warning system of Tsunamis (Minami et al., 2015; Schnepf et al., 2016). This is due to the fact that Tsunami induced EM signals, like the signal of seismic waves, can be divided into fast and slowly moving signal parts (Minami et al., 2021). However, a major drawback in the field is the fact that the observation of Tsunami induced EM signals will probably be limited to terrestrial observations (Kuvshinov, 2008). Despite the fact that even relatively small Tsunamis can create an observable magnetic signature (Torres et al., 2019) locally, the signal magnitude is inversely proportional to the square of the distance. Given the small spatial scale, the signal will be below a measurable threshold when reaching satellite altitude.

Developments in the field of Tsunami induced EM signals are quite young in comparison to the more mature field of EM signals induced through general ocean circulation and ocean currents. Here the signals have not only been successfully observed but also used to observe volume transports. This was done for example for the Florida current (J. C. Larsen et al., 1985, 1992) or the Kuroshio (Andres et al., 2015; Segawa et al., 1992). The respective signals have been observed using seafloor voltage cables or so called EM-APEX profilers (Sanford et al., 2005). Considering that EM signals induced by the general ocean circulation, especially the signals induced through the Antarctic Circumpolar Current (ACC), are in principle strong enough to be measurable from space, one of the remaining challenges in the field is the extraction of ocean circulation induced electromagnetic signals from satellite observations. This is also one of the declared objectives of the Swarm Mission launched in 2013 (Friis-Christensen et al., 2006; Olsen et al., 2013). A detection of these signals would significantly advance the fields of ocean remote sensing (Irrgang et al., 2017) and the fields of mapping and modelling magnetic field sources for an improved noise reduction in magnetotelluric studies (Maus et al., 2006). Consequently, studies were conducted to characterize the estimated magnetic field signal in terms of signal strength (Glazman et al., 2005; Vivier et al., 2004), variability or uncertainty (Irrgang et al., 2016a,b; Manoj et al., 2006) and depth of origin (Irrgang et al., 2018). A promising estimation of the EM ocean circulation signals based on altimetry data using the geostrophic approximation has been proposed by Saynisch et al. (2018).

The third and most advanced subtopic and, also, a focal point of the thesis at hand is the research on tidal ocean-dynamo signals (TODS). These signals have been observed for more than a century using different measur-

ing techniques like telegraph cables (Adams, 1881; Wollaston, 1881), towed electrodes (Young et al., 1920), seafloor voltage cables (Duffus et al., 1974; Fujii et al., 2000; Kuvshinov et al., 2006), terrestrial magnetometer measurements (Bindoff et al., 1988; Cueto et al., 2003; Hewson-Browne, 1973; Love et al., 2014; Malin, 1970; Maus et al., 2004; McKnight, 1995; Schnepf et al., 2018; Winch, 1970; Winch et al., 1981), ocean bottom magnetometers (Schnepf et al., 2014) or satellite magnetometers (Grayver et al., 2019; Sabaka et al., 2018, 2016, 2015; Tyler et al., 2003).

TODS observed from space are in good agreement with model predictions which can be attributed to the achievements in the field of TODS modelling. Four onsets for modelling motionally induced EM signals have developed: a thin sheet approximation (Stephenson et al., 1992; Tyler et al., 1995, 1997; Vivier et al., 2004), a contracting integral equation approach that operates in the frequency domain (Kuvshinov, 2008; Kuvshinov et al., 2002, 2005; Pankratov et al., 1997), a finite element approach (Velímský et al., 2005) and a finite difference approach (Flosadóttir et al., 1997). The thin-sheet models were sufficiently accurate to support the validity of the first satellite detection, but its computation relies on the insubstantial assumption of an insulating mantle conductivity. The integral equation approach does not. The integral equation approach has been adopted in many studies (Manoj et al., 2006; Smith, 1996a,b), produces more accurate results than most approaches (Kelbert et al., 2014; Sachl et al., 2019) and allows for efficient computation. Additionally, the operation in the frequency domain is natural when studying periodic phenomena such as ocean tides. This is why the presented studies (cf. chapters 4 and 5) rely also on the integral equation approach by using the x3dg-model of Kuvshinov et al. (2002).

The achievement of being able to reliably model and extract TODS also has applications in further research fields. On the basic level, the TODS have been identified as a source of noise. In magnetotelluric studies, TODS have hence been removed since the 1960's (Constable, 2013; Cox, 1980; Junge, 1988). Also, Guzavina et al. (2018) have demonstrated the impact on the recovery of ionospheric signals and have developed a novel data correction scheme. Additionally, also in the field of magnetotellurics, there is the remaining challenge of determining the 3D conductivity distribution beneath the ocean and continents. This problem is linked to ocean tide induced magnetic field signals due to the sensitivity of these signals to subseafloor conductivity distributions (Chave, 1983; Dostal et al., 2012; Schnepf et al., 2015). Reducing the uncertainty about the conductivity distribution

is also one of the key objectives of the Swarm Mission (Olsen et al., 2013). The ever-growing amount of available satellite data and the increasing quality thereof has led to a growing number of publications providing insights into Earth's conductivity distribution (Civet et al., 2013, 2015; Kuvshinov et al., 2006; Püthe et al., 2013, 2014, 2015; Velímský, 2010, 2013). A noteworthy milestone in this field was the inversion of global 1-D conductivity distributions from satellite observations of M2 tide induced magnetic field signals by Grayver et al. (2016).

Two recent developments, i.e., the continuous improvements in TODS modelling and the advances in the field of spaceborne TODS observations, motivated research on the link between physical oceanography and TODS. On the one hand, new TODS modelling approaches led to more reliable conductivity distributions, especially when combined with physical oceanography. On the other hand, satellite measurements obtained from the CHAMP (CHAllenging Minisatellite Payload) mission were used to extract the signal of the principal lunar tide M2 (Tyler et al., 2003) and include these signals into the magnetic field model of Sabaka et al. (2015) CM5. However, 12 years of CHAMP data were used for this analysis. With the increased precision (0.1 nT) and the improved experiment design (along-track and cross-track measurements) of the Swarm mission, Sabaka et al. (2016) were able to extract not only the signals of the M2 but also the smaller N2 using only the first 20,5 months of data. The extracted N2 signals, however, were unreliable - a problem solved by Grayver et al. (2019) who did not only improve the results but also extracted the additional O1 signal by combining CHAMP and Swarm data. Thus, the prospect of ocean remote sensing using TODS in the near future was a catalyst for studies investigating TODS amplitude uncertainties (Saynisch et al., 2018) and the impact of climate variations on TODS amplitudes. Saynisch et al. (2017) for example investigated how tidal ocean-dynamo signal amplitudes change in oceanic warming scenarios derived from climate model predictions of CMIP5. Motivated by the ongoing increase in ocean heat content and the lack of seawater temperature observations below 2000 m depth, Irrgang et al. (2019) used machine learning techniques to infer global ocean heat content from global ocean tide induced magnetic field amplitudes. Furthermore, the effect of a breakdown in the Atlantic Meridional Overturning Circulation (AMOC), a possible tipping point in the climate system, and the impact on tidal ocean dynamo signals due to redistribution of cold and warm ocean waters was investigated by Saynisch et al. (2016).

While reviewing the recent developments on the link between ocean phenomena and temporal TODS variations, it becomes apparent that existing studies focused on temporal TODS variations on decadal time scales and demonstrated the sensitivity of these signals towards seawater temperature and salinity changes. The increased measurement precision of the Swarm Mission and the decrease in observation period lengths raise the expectation of a near future TODS based ocean remote sensing on sub-decadal and possibly even annual or sub-annual time scales. Likewise, the mentioned studies focus mainly on signal amplitude variation. So far, only one study on phase variations in TODS attributed to changes in seawater conductivity and the geomagnetic field was conducted by Saynisch-Wagner et al. (2020). The present thesis contributes to the outlined field of research by addressing the need for studies on the impact of seawater temperature and salinity variations on sub-decadal of even seasonal time scales on both TODS amplitudes and phases. [1]

1 The literature review in the present thesis provides only a narrow overview of the relevant literature. A comprehensive overview of the better part of relevant literature in the field of EM fields of oceanic origin can be achieved through the study of the following review papers:
The review of Longuet-Higgins et al. (1949) covers the developments ranging from the first mention in Faraday's treatise to the 1940s. The review also includes the experiment of Young et al. (1920) who measured TODS using towed electrodes. They realised that the measured EM signals were not in phase with the local tidal motion but with a stronger remote tidal stream, a first proof of the remote sensing capabilities of TODS. Then, there are the reviews of Palshin (1996) and Kuvshinov (2008) who cover motional induced EM fields together with magnetically induced EM fields in the ocean. Similarly, in "Instrumentation and experimental methods for oceanic studies" (Filloux, 1987), the topic of motionally induced electric fields is treated as one of several aspects. The review of Szuts (2012) focuses on the possibility of indirectly measuring ocean velocities from motionally induced electric field signals and covers the technical and the theoretical side. The most recent review from Minami, 2017 focuses primarily on Tsunami and Tide induced electromagnetic fields.

3.2 AIMS AND STRUCTURE

This cumulative thesis was compiled to close existing knowledge gaps about TODS variations on sub-decadal time scales using three manuscripts that have either been already published or are currently under review. The studies give answers about: (1) ENSO related signal variations, (2) global spatio-temporal variation patterns and (3) observations of signal variations. The first study (chapter 4) is a model study investigating the sensitivity of TODS towards ENSO, a well known quasi-periodic climate phenomenon. Building upon the findings of the first study, the second study (chapter 5) uses 25 years of in-situ observations for identifying ocean regions with large TODS variations together with their temporal dynamics. The third study (chapter 6) investigates whether the variations identified in the second study can be reliably extracted from observatory data. Chapter 7 summarizes the results, provides additional context and perspective for future studies.

ENSO Related Signal Variations

How big are ENSO related TODS amplitude variations?

How are these amplitude variations distributed in space and time?

What underlying oceanic causes relate to temporal amplitude variations?

The El Niño/Southern Oscillation causes large scale seawater temperature and salinity anomalies in the central Pacific. Because of these anomalies and their quasi-periodic occurrence with a period of three to seven years, ENSO is a likely candidate for sub-decadal TODS variations. Using a coupled ocean-atmosphere general circulation model and a global induction model, the study design allows for a comprehensive analysis of the link between ocean dynamics and tidal ocean dynamo signals. As ENSO dynamics include not only sea surface but subsurface processes like thermocline depth variations, the obtained comprehensive understanding allows for an estimation of the electromagnetic signature of other oceanic processes, an important step towards observing and interpreting temporal TODS variations.

Global Spatio-Temporal Variation Patterns

What is the expected magnitude and spatio-temporal distribution of recent TODS amplitude variations?

In which ocean regions can we expect the largest changes in TODS?

Which oceanic processes can be attributed to the identified signal variations?

The second study extends the regional analysis made in the Central Pacific to a global scale. Using a time series of global tidal ocean dynamo signals, the study identifies signal variations and analyses their temporal development. In contrast to the first study, the oceanographic data is not modeled. Instead, it is obtained from data products based on a statistical analysis of in-situ observations. In addition to the comprehensive view on the cause and effect relation between the ocean and induced electromagnetic signals, this allows to link observed anomalies to the research of recent ocean dynamics. Apart from the deepened understanding of the signals, the study provides an observation based climatology of TODS variations and identifies ocean regions where the electromagnetic signals are most susceptible to seawater temperature and salinity changes. Both the climatology and the location of the identified highly sensitive ocean regions are testable assets in the pursuit of advancing the accuracy of existing TODS extraction methods.

Observations of Signal Variations

Can we identify seasonal variations and trends in magnetometer observatory data?

What temporal resolution can be achieved for reliable tidal signals extraction?

Are amplitudes and phases equally robust in the extraction process?

Using the findings of the previous study, the third study attempts to identify seasonal variation and trends in magnetometer observations. This step is much needed to test existing assumptions and assess the obtained understanding of the link between ocean dynamics and TODS variations. The increased understanding of the complexity of the temporal TODS devel-

opment is especially valuable when trying to resolve the existing offset between observed and modeled TODS in coastal proximity. The much needed advances in the field of TODS modelling are thus provided by robust observation techniques and reliable statements about local TODS amplitudes and phases.

Part II

Advancement

4

ELECTROMAGNETIC CHARACTERISTICS OF ENSO

by Johannes Petereit[1,2], Jan Saynisch[1], Christopher Irrgang[1], Tobias Weber[1], Maik Thomas[1,2]

[1] GFZ German Research Center for Geosciences, Potsdam, Germany
[2] Freie Universität Berlin, Institute of Meteorology, Berlin, Germany

This paper is published in Ocean Science.

Abstract

Electrically conducting sea water flows through Earth's magnetic field and induces secondary electric and magnetic fields. The tidal ocean flow induces periodic magnetic fields which are easily detectable in magnetic field measurements. Additionally, they have been found to be sensitive to changes in oceanic temperature and salinity distributions. The tidal magnetic fields could be used to monitor phenomena that are redistributing oceanic heat and salinity. Such a phenomenon is the El Niño/Southern Oscillation (ENSO). We simulated 50 years of ENSO with a coupled ocean-atmosphere climate model to investigate the impacts of ENSO on the tidal magnetic field. For this purpose, we calculated a Magnetic Niño Index (MaNI). This index was then compared to the Oceanic Niño Index (ONI) derived from sea surface temperatures and we put MaNI in relation to oceanic subsurface processes. We show how oceanic subsurface processes leading over sea surface processes result in Magnetic Niño Index that is leading by 5 month over the Oceanic Niño Index.

4.1 INTRODUCTION

The El Niño/Southern Oscillation (ENSO) is well known for its warm and cold temperature anomalies caused by changes in the ocean-atmosphere system in the equatorial Pacific Ocean. These anomalous events, known as El Niño and La Niña, can cause extreme weather conditions throughout the

globe, e.g. tropical cyclones (Vincent et al., 2011), droughts, bush fires and floods (Philander, 1983). This extreme weather affects whole ecosystems (Glynn et al., 1991), causes damages to infrastructure and agricultural production (Wilhite et al., 1987), increases health risks and causes deaths (Vos et al., 1999). The frequency of extreme El Niño events is assumed to double in response to greenhouse warming (Cai et al., 2014). Further increase in the already substantial socio-economic costs would be the consequence. Reliable forecasts of El Niño events give the opportunity to mitigate these negative impacts.

Changes of upper ocean heat content are known to be a major source of ENSO predictability (Meinen et al., 2000). Monitoring of seawater temperature and salinity anomalies are consequently beneficial for an improved ENSO forecast. Especially since changes in thermocline depth, caused by equatorial Kelvin waves, have been known to precede sea surface temperature anomalies (Harrison et al., 1984).

Altimetry measurements are well known to measure these displacements and have been subject of extensive research (Ji et al., 2000; Picaut et al., 2002, 1996). A lesser known method to detect changes in the oceanic heat content are the motion-induced electromagnetic fields of the ocean (Irrgang et al., 2016b; Minami, 2017). The flow of electrically conducting seawater generates an electric current due to the interaction of moving salt ions with Earth's geomagnetic field. The magnetic field induced by these electric currents can locally reach several nano Tesla (nT) (Kuvshinov, 2008).

The oceanic magnetic field strength depends on the strength of ocean flow and its electric conductivity. The ocean flow is usually divided into two types, flow caused by wind driven and thermohaline circulation and flow due to oceanic tides.

The circulatory flow is irregular in time and consequently difficult to separate from magnetic field measurements. However, the circulatory magnetic field's non-trivial contributions to the geomagnetic field have been subject of many studies (Irrgang et al., 2016a,b, 2017; Manoj et al., 2006; Tyler et al., 1995) Manoj et al. (2006) analysed the influence of changes in equatorial currents caused by ENSO on the circulatory magnetic field. They found that the ENSO generated magnetic field anomalies were too small to be distinguishable from the magnetic field anomalies produced by the Antarctic circumpolar current with a magnitude of ± 0.2 nT.

The tidal flow on the other hand is periodic, which allows an easy separation of its magnetic field from other constituents in geomagnetic field

measurements. Accordingly, these signals have been extracted successfully for the semidiurnal M2 and N2 tides from measurements of the magnetic satellite missions CHAMP and Swarm (Sabaka et al., 2016; Tyler et al., 2003). Amplitude variations of these periodic magnetic signals are mostly caused by variations in seawater conductivity distribution. Seawater conductivity is sensitive to seawater temperature and salinity and these quantities exhibit high variability in comparison to the amphidromic system of the tides. Consequently, all information gained about variations of the oceanic tidally induced magnetic signals are directly linked to changes in the oceanic temperature and salinity distributions. Modelled and measured tidally induced magnetic fields are in good agreement (Kuvshinov, 2008; Sabaka et al., 2016; Tyler et al., 2003) offering the possibility for in silico sensitivity studies.

The influences of climate variations with a global impact such as Greenland glacial melting (Saynisch et al., 2016) and global warming (Saynisch et al., 2017) on the electromagnetic oceanic tidally induced signals have already been investigated. For these cases, the tidally induced radial magnetic field was found to be an appropriate measure to monitor climate variations of the global oceanic conductivity on decadal time scales.

ENSO alters not only the ocean circulation in the equatorial pacific. It also alters the conductivity of the equatorial upper Pacific Ocean ($\approx$ 300m) on a regional scale within months.

In our study, we follow the approach of Saynisch et al. (2017) and investigate whether the electromagnetic oceanic tidally induced signals could be used as an appropriate measure to monitor these changes in seawater conductivity and, consequently, the dynamic of the El Niño/Southern Oscillation.

4.2 MODELS AND DATA

Ocean and tidal induced current

We simulated ENSO with a global coupled atmosphere-ocean model, the ECHAM6/MPIOM.

The Max-Plank-Institute Ocean Model (MPIOM, (Marsland et al., 2003)) is a general ocean circulation model. The model solves the primitive equations for a hydrostatic Boussinesq fluid on a curvilinear Arakawa-C-grid with poles shifted to Antarctica and Greenland. The ocean is discretised on

a grid with a horizontal resolution of $\sim 3.0^\circ \times 1.8^\circ$ (GR30) and an irregular vertical distribution over 40 horizontal levels.

The atmosphere general circulation model ECHAM6 (Roeckner et al., 1996) is applied with the horizontal resolution of $\sim 3.75^\circ \times 3.75^\circ$ (T31) and 31 vertical hybrid sigma/pressure levels.

The simulated ocean data covers 50 years of monthly mean seawater temperature T, seawater salinity S and seawater pressure P. Using the Gibbs seawater equation (TEOS-10 (IOC et al., 2010)), the seawater conductivity σ can be calculated from, T, S and P. The modelled time span represents a climate similar to present day conditions, but represents reality only in a statistical sense.

The tidally induced electric current, the source for the electromagnetic oceanic tidal signals (EMOTS), is derived for each month with the following two step algorithm.

First, the product of seawater conductivity σ and tidal velocities $\vec{v}_{M2}$ is integrated from ocean bottom (-H) to surface (SSH)

$$\vec{V}_{M2}(\varphi, \vartheta, t) = \int_{-H}^{SSH} \sigma(\varphi, \vartheta, z, t) \cdot \vec{v}_{M2}(\varphi, \vartheta, z, t)\, dz, \tag{4.1}$$

where φ, ϑ and z are longitude, latitude and depth. The tidally induced electric current $\vec{j}_{M2}$ is then calculated as the cross-product of the depth-integrated and conductivity-weighted transports $\vec{V}_{M2}$ and the ambient geomagnetic field $\vec{B}_{\text{Earth}}$ as,

$$\vec{j}_{M2}(\varphi, \vartheta) = \vec{V}_{M2}(\varphi, \vartheta) \times \vec{B}_{\text{Earth}}(\varphi, \vartheta). \tag{4.2}$$

Variations in the amphidromic system are negligible even on decadal time scales (Saynisch et al., 2016). Consequently, we followed the approach of Saynisch et al. (2017) and assumed the tidal system to be invariable in time. The tidal amplitudes and phases of the oceanic M2 tide were taken from the TPXO8-atlas (Egbert et al., 1994, 2002).

For this study, Earth's magnetic field $\vec{B}_{\text{Earth}}$ was estimated with the International Geomagnetic Reference Field edition IGRF-12 (Thébault et al., 2015). The naturally occurring secular variations in $\vec{B}_{\text{Earth}}$ will linearly vary $\vec{j}_{M2}$ (equ. (4.2)). The geomagnetic field is well known for real observation times (Gillet et al., 2010) and its secular variations should be taken into account before analysing real observations of EMOTS for the influence of

ENSO. However, our study focuses on the effects of oceanic conductivity variations. We consequently assume $\vec{B}_{\text{Earth}}$ to be constant in time.

EMOTS

The electromagnetic oceanic tidal signals are the electromagnetic response of interactions between the tidal electric current $\vec{j}_{M2}$ and its electrically conducting environment. The EMOTS in our study are modelled with the induction model x3dg of Kuvshinov (2008). The model's solutions are based on a volume integral approach combining the modified iterative dissipative method of Singer et al. (1995) with a conjugate gradients iteration. For realistically modelled interactions, Earth's mantle conductivity and the oceanic conductivity need to be included in the model-setup (Grayver et al., 2016). The mantle conductivity is represented by a time constant 1-D spherical symmetric conductivity distribution following Püthe et al. (2015). The time variant ocean conductivity and the constant sediment conductance are represented by an inhomogeneous spherical conductance layer situated on top of the mantle conductivity. This conductance layer combines sediment conductance and modelled ocean conductance, derived from modelled T, S and P. The sediment conductance is a combined result of the method of Everett et al. (2003) with the global sediment thickness of Laske et al. (1997).

Indices and statistical analysis

Different indices have been used to identify anomalous ENSO events (Hanley et al., 2003). A current state-of-the-art indicator is the Oceanic Niño Index (ONI) (NOAA, 2017) from the climate prediction center (CPC) of the National Oceanic and Atmospheric Administration (NOAA). The ONI is used to monitor the oceanic part of the ocean-atmosphere phenomenon. It is defined as a 3 months running mean of sea surface temperature anomalies in the Nino 3.4 region (i.e., 5° N - 5° S, 120° W - 170° W) relative to the mean annual signal of regularly updated 30-year base periods. Warm and cold events are identified as periods exceeding a threshold of ± 0.5° C longer than 4 months. The sea surface temperatures of the Nino 3.4 region have been known to correlate well with ENSO (Bamston et al., 1997).

In our study, the ONI is calculated from the ECHAM6/MPIOM model experiment. We used all 50 years as base period, since no significant trends are present in our data.

We also calculate a comparable index based on the radial tidally induced magnetic field B_r (see section 4.2), the Magnetic Niño Index (MaNI). The same algorithm as in the ONI calculation is used with the difference that the sea surface temperature anomalies are substituted with B_r anomalies in the Nino 3.4 region.

The relation of the indices is analysed by calculating their correlation. Additionally, a time delay analysis is carried out by calculating and analysing the cross-correlation. For two time series, the cross-correlation is the evolution of correlation between those two when they are shifted against each other in time. It can be used to identify temporally lagging or leading signals.

4.3 RESULTS AND DISCUSSION

Comparison of indices

The time series of ONI and MaNI are shown in figure 4.1. In agreement with the NOAA classification (NOAA, 2017), we find that the climate model data contain 7 El Niños and 10 La Niñas. Following Null (2017), we find that 1 out of the 7 El Niños is classified as very strong ($\geq 2.0^\circ$ C), 3 are found to be moderate (1.0 to 1.4 $^\circ$ C) and 3 are classified as weak (0.5 to 0.9° C). The set of simulated La Niña events consists of 6 moderate (-1.0 to -1.4° C) and 4 weak events (-0.5 to -0.9° C).

The very strong warm event is found at the most prominent peak of the time series and starts at month 133 of the modelled time with a time span of 16 month and a maximum value of 2.3° C (figure 4.1). These values are comparable to that of observed El Niño events (warm events) taken place in winter 1997/8 or 2015/6, with anomalies of 2.3° C and durations of 13 and 19 month, respectively (NOAA, 2017).

The mean spatially averaged B_r signal in the Nino 3.4 region was found to be 0.546 nT with a mean seasonal variation of ± 0.29 pT (pikoTesla). The MaNI-range of -0.84 pT to 0.82 pT is comparable to the seasonal variation. High performance magnetic field sensors have reduced the noise levels down to 0.3 fT $\mathrm{Hz}^{-1/2}$ (Schmelz et al., 2011) and current field magnetometer reach precisions of 50 fT $\mathrm{Hz}^{-1/2}$. Considering this in combination

with the easy detectability of the periodic tidal part in magnetic field measurements, it is reasonable to assume that a ENSO induced B_r anomalies become detectable within years.

While the ONI covers the development of sea surface processes, the MaNI also includes subsurface processes. B_r is an integral measure incorporating the seawater conductivity integrated from ocean bottom to sea surface (see equ. (4.1) and equ. (4.2)). Despite their differing perspective on oceanic processes, both indices show a correlation of 0.63. The SST based index ONI is used to quantify the duration and strength of anomalous ENSO events. The high correlation of both indices indicates that ENSO is not only dominating sea surface processes (ONI) but has also considerable impact on subsurface processes integrated in the tidal magnetic field.

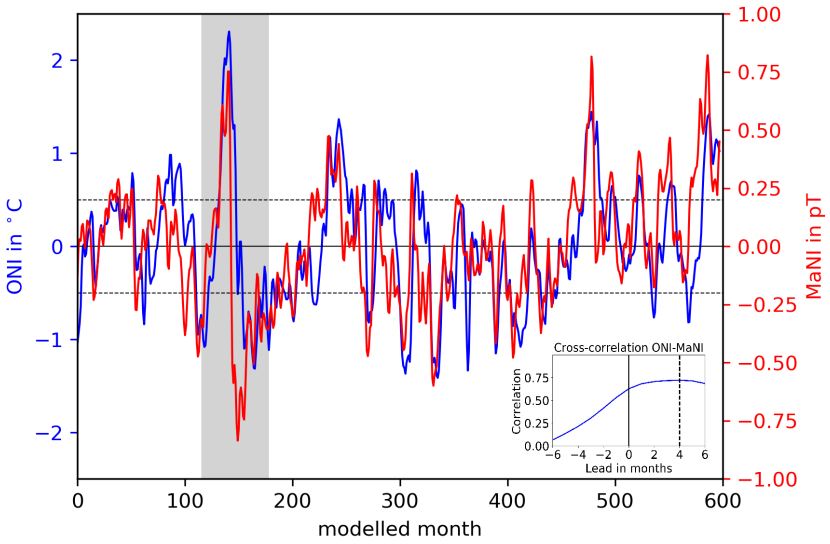

Figure 4.1: ENSO indices. ONI derived from sea surface temperatures (blue curve) and MaNI derived from the radial tidal induced magnetic field B_r (red curve). The solid horizontal line marks the zero value for both time series. The dashed lines mark the threshold of ± 0.5 °C, the threshold for El Niño and La Niña events. The grey shaded area marks the strongest cycle of ENSO events (used for further analysis). The embedded plot shows the cross-correlation between ONI and MaNI. For positive leads, MaNI leads ONI.

The analysis of the cross-correlation of the two indices (embedded plot in figure 4.1) shows a MaNI-lead of 4 months over the ONI. Accounting for this lead, the correlation of both time series is increased to 0.72.

Since in our setup the only time-variable contribution to B_r is the seawater conductivity σ, we conclude that in the Nino 3.4 region subsurface anomalies of σ, caused by anomalies in S and T, are leading SST anomalies.

Spatial and temporal anomaly development

A different perspective on the underlying processes is shown in figure 4.2. The temporal and spatial development of SST and B_r anomalies are shown as Hovmoeller plots. Shown is the development of the strongest ENSO cycle of the time series (indicated by the grey shaded interval in figure 4.1). The findings for the other regular ENSO cycles are comparable (not shown).

The amplitude of B_r in the ENSO region is decreased by the presence of the geomagnetic equator. Additionally, B_r is varied by the distribution of the tidal flow. Consequently, SST and B_r anomalies have been averaged from 5° S to 5° N to diminish the disturbing influences. Remaining influences are visible as vertical lines in figure 4.2.

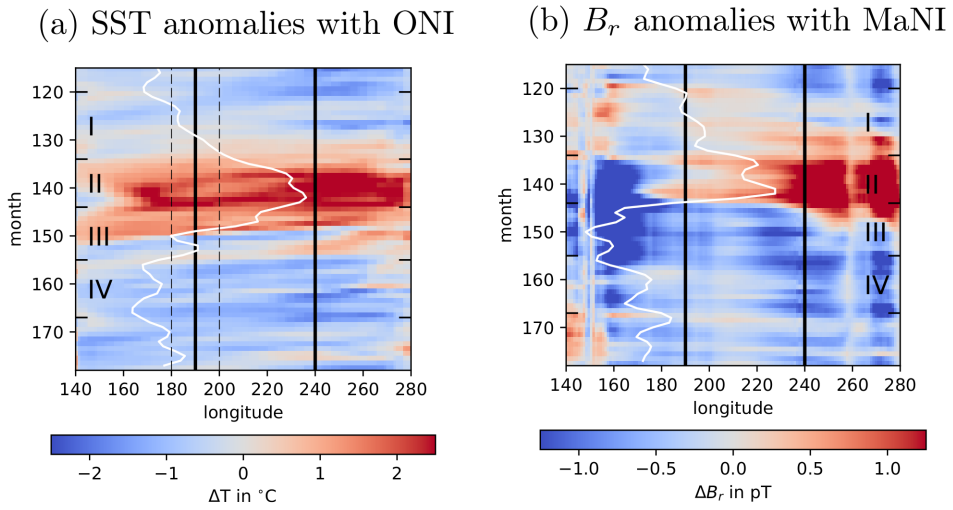

Figure 4.2: Hovmoeller plots of sea surface temperature anomalies (left image) and B_r anomalies (right image) averaged from 5° S to 5° N. The chosen time interval contains the strongest ENSO cycle and is identical to the grey shaded time interval of figure 4.1. Vertical black lines enclose the Nino 3.4 region used to calculated ONI and MaNI. The solid white lines represent the indices derived from the individual anomalies centred on 170° E (20° of longitude correspond to 1° C (left) and 0.4 pT (right)). The dashed lines in the left image represent the thresholds of ±5 °C by which El Niño and La Niña events are identified in the ONI. Roman numerals identify different phases of the presented dynamics.

In the following we present differences and agreements in the dynamics of anomalies presented in figure 4.2. For this purpose, different phases in the dynamic of the ENSO cycle have been identified.

The comparison of figure 4.2a and figure 4.2b shows the development of B_r anomalies before SST anomalies. Positive B_r anomalies emerge almost

a year before they form in SST (phase I in figure 4.2). The same is found for negative B_r anomalies. They also emerge months before positive SST anomalies receded, which marks the end of El Niño (phase III).

At the beginning of the first phase (I) we find the following conditions. A positive B_r anomaly is found west of the Nino 3.4 region, while at sea surface cold or neutral conditions are found. Then positive B_r anomalies travel through the Nino 3.4 region eastwards. They are caused by equatorial Kelvin waves known to precede the onset of El Niño (Harrison et al., 1984). The Kelvin waves deepen the thermocline and increase the conductance in the upper ocean. SST anomalies have not formed during this phase. An intensification of positive B_r anomalies on the South American west coast is observed with the arrival of the Kelvin waves several months before the start of El Niño as defined by NOAA. This is explained by the anomalous increase of warm water in the upper ocean caused by the deepening of the thermocline (Wang et al., 2013).

During the second phase (II), El Niño's effects become apparent at sea surface. Changes of wind patterns in the Walker Circulation cause changes in the equatorial current system (McPhaden, 1999). Consequently, the warm water of the Western Warm Pool flows eastward and leads to an increase and westward expansion of SST anomalies at the Peruvian coast. The eastward migrating warm water also causes a thermocline shallowing in the Western Warm Pool and a simultaneous deepening of the thermocline at the Peruvian coast are the consequence. This leads to negative (positive) B_r anomalies west (east) of the Nino 3.4 region reaching local amplitudes of -6 pT (3 pT) when El Niño has fully developed. During this phase, ONI and MaNI are in good agreement indicating that sea surface and subsurface processes are sharing the same dynamic. The maxima of both indices are found at comparable points in time.

The beginning of the third phase (III) is marked by an eastward expansion of the western negative B_r anomaly that has formed during phase II. The effects of El Niño in form of warm SST anomalies are still present for several months. Subsurface processes, however, cause an early decrease in B_r anomalies and consequently in MaNI. The eastern positive B_r anomaly recedes and a negative anomaly forms months before the onset of La Niña becomes apparent in ONI.

The fourth phase (IV) marks the beginning of La Niña at sea surface. During this phase, ONI and MaNI are in good agreement because sea surface and subsurface are following the same dynamics. The Walker Circulation

returns to normal conditions and the westward direction of the equatorial ocean current is re-established. Hence, the eastern thermocline shallows due to upwelling of cold water and warm surface water is transported to the western warm pool. Westward travelling SST and B_r anomalies are the consequence.

With the end of phase IV a new cycle starts from the beginning. The build-up of positive B_r anomalies can be observed towards the end of the plotted time interval.

The analysis shows that the identified lead in the MaNI is not just a mere forward shift of the signals. The lead is a result of different effects. It is caused by early signs of the onset of the El Niño caused by eastward travelling Kelvin waves in combination with a decrease in the magnetic signal months before the actual end of El Niño due to a shallowing of the thermocline. Consequently, B_r anomalies seem to fulfil their ENSO induced cycle before SST anomalies do.

Cross-correlation ONI and conductance

These results are backed up by the findings we get from calculating the cross-correlation between the oceanic conductance and the ONI at each grid point (figure 4.3).

In figure 4.3a the maximum conductance anomaly at each grid point is shown. The magnitude of conductance anomalies is linked to the magnitude of relative EMOTS-changes. The largest signals are therefore evident in the Western Warm Pool and at the west coast of South America. In these regions, the thermocline undergoes the largest relative changes as a result of ENSO. We also find that the conductance anomalies are elevated in a small band throughout the whole equatorial region. This region is the passage way of the equatorial Kelvin waves and therefore the region with high variability in thermocline depth.

In figure 4.3b, the maximum absolute correlation is plotted. Its largest values are found east of the Nino 3.4 region. The values decrease westwards in a tongue shaped pattern, like the typical SST anomalies of El Niño and La Niña.

Figure 4.3c shows the lag between the ONI and the conductance at each grid point. The lead in conductance increases in a tongue shaped pattern originating from the South American west coast. Since the Kelvin waves

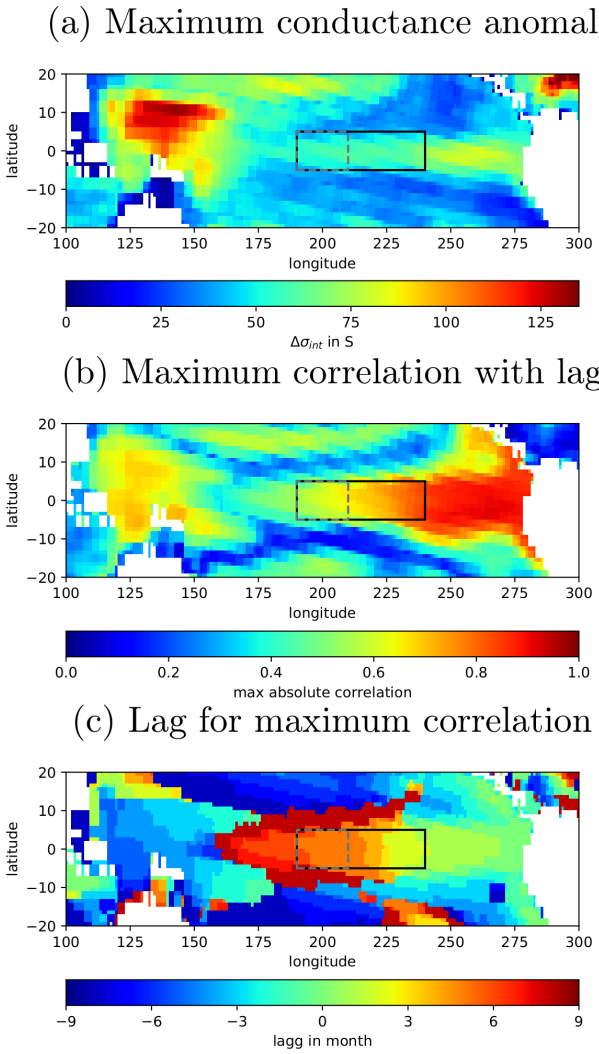

Figure 4.3: Summary of cross-correlation analysis between the ONI and the conductance (σ_{int}) at each grid point. The top image shows the maximum absolute conductance anomaly. The middle image shows the absolute maximum correlation, the peak value of the cross-correlation. The bottom image shows the corresponding lead/lag to the absolute maximum correlation. The solid rectangle shows the location of the Nino 3.4 region, the dashed rectangle shows the location of an improved MaNI (5° N - 5° S, 150° W - 170° W).

travel eastwards an increase in the lead towards their origin is a logic consequence.

For the Nino 3.4 region (solid rectangles in figure 4.3) in figure 4.3, we find the same characteristics as for the analysis in section 4.3. The maximum absolute correlation of the whole region ranges from ≈ 0.7 to ≈ 0.8 (fig. 4.3b). The lead distribution in the area is not uniform. A large part of the western half is leading by 5 months and decreases eastward to 2 months. The area-averaged B_r anomalies of the MaNI therefore produce a

signal that is leading in averaged by 4 month with a correlation between 0.7 and 0.8.

Test of results

In order to put the interpretation of our results to a test, we did a reanalysis of the results from section 4.3 with an updated region for the MaNI. The new region is located at 5° N - 5° S, 150° W - 170° W. It keeps the poleward extend of ±5° to account for an adequate averaging in account of the presence of the geomagnetic equator. The eastern boundary is shifted westwards to increase the lead in magnetic field anomalies over SST anomalies (see figure 4.3c). The westward shift is constrained by the maximum correlation found in figure 4.3b. A recalculation of the MaNI within the updated region is shown in figure 4.4.

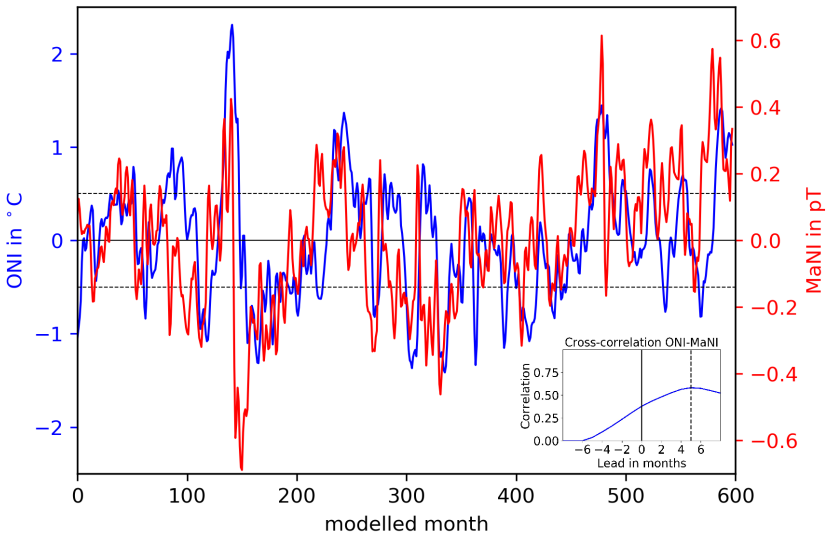

Figure 4.4: Comparison of time series of ONI (blue) and updated MaNI (red). Anomaly strength and correlation are reduced, while the lead is increased.

A repetition of the initial analysis from section 4.3 shows a decreased correlation of both time series, 0.38 for a lag of 0. The maximum correlation has also decreased to 0.58, while the lead has increased to 5 month. The range of the updated MaNI has reduced to −0.69 pT - 0.61 pT.

These findings are in agreement with the previous findings of section 4.3. Consequently, we conclude that the lead in MaNI found in section 4.3 and 4.3 is caused by the lead in conductance anomalies found in section 4.3.

The correlation and cross-correlation are a linear measure for the relation between two variables. ENSO is the major influence on the course of ONI and MaNI. However, we found that the different processes contributing to ENSO cause different developments in sea surface and subsurface dynamics. Consequently, the decrease in correlation should be viewed as an increase in information gained from the perspectives of SST and B_r anomalies onto the same phenomenon.

4.4 SUMMARY AND CONCLUSION

In this study, we investigated whether the electromagnetic oceanic tidal signals, integrating oceanic processes from bottom to surface, could be used as an appropriate measure to monitor the El Niño/Southern Oscillation.

We used a coupled ocean-atmosphere general circulation model to model 50 years of monthly mean seawater temperature, salinity and pressure. The properties are used to calculate the electromagnetic tidal signals for each.

We analysed the relation of electromagnetic signals and ENSO by comparing two ENSO related indices. These indices, calculated in the Nino 3.4 region, are the Oceanic Niño Index (ONI), based on SST anomalies, and the Magnetic Niño Index (MaNI), based on anomalies in the tidal magnetic field. A high correlation between both indices was found. Additionally, we found MaNI leading ONI by 4 months.

The spatial and temporal evolution of B_r anomalies was analysed and compared to the evolution of SST anomalies in order to explain the found lead. We found the lead to be caused by eastward travelling equatorial Kelvin waves. They are known to precede the development of ENSO typical SST anomalies. They are also increasing the thermocline depth in the eastern Pacific ocean. An increase of electric conductivity in the upper ocean and therefore and increase in the tidal magnetic field is the consequence.

Based on these findings, we analysed the relation of equatorial Pacific conductance anomalies and the ONI. The found spatial distributions in correlation, lead and signal strength were used to explain the found MaNI characteristics. We found an eastward increase in correlation of conductance anomalies and the ONI, while the lead is increased westward.

These findings were tested by a recalculation of the MaNI in a modified region. We could confirm our interpretation and increase the lead in MaNI to 5 month. In the same time, signal strength and correlation was reduced. Sea surface and subsurface dynamics are driven by different aspects of the

same phenomenon, the El Niño/Southern Oscillation. The decrease in correlation is interpreted as a gain in information about subsurface dynamics.

In summary, our study shows that the dynamic of tidally induced radial magnetic field anomalies contains appropriate information for an early awareness of developing anomalous warm and cold ENSO conditions. This in return may be used to improve the current warning system. Consequently, social-economic effects brought into different regions of the Earth due to ENSO's teleconnections could be diminished with early pro-active counter measurements.

The first study demonstrated that, at the moment, ENSO related changes in TODS amplitudes in the Central Pacific are too small to be measured, despite large scale temperature and salinity changes. One reason for this is the location of the geomagnetic equator. The geomagnetic equator is located in the region where temperature and salinity anomalies are largest, but the reduced vertical geomagnetic field contributions at the geomagnetic equator result in only small TODS amplitudes in the first place. An additional reason for small signals is found in the fact that the TODS inducing tidal waves are shallow-water waves. The oscillation of shallow-water waves reaches from sea surface to ocean bottom and affects, therefore, the entire water column. TODS are consequently an integral measure of the conditions found in the whole water column. In relation to a water column of several kilometers depth, surface dynamics, like the investigated ENSO related seawater temperature and salinity changes, play only a minor role.

Although the study demonstrated a significant lead of TODS over the onset of cold and warm phases of ENSO, it is unlikely that TODS can be used as a main predictor for El Niño events. This is not only due to the small signal strength of anomalies caused by ENSO but also because of the fact that the found correlation and lead time with respect to the onset of El Niño events are insignificant in comparison to achievements made in the field of computational ENSO forecasting. A standing problem in the field of ENSO forecasting is to overcome the spring barrier to achieve long lead time forecasts of more than 6 months. However, state of the art approaches in the field of ENSO prediction (Ludescher et al., 2019; Meng et al., 2020) are not only able to forecast the occurrence of an El Niño event about one year in advance with high accuracy but also its magnitude.

The demonstrated influence of subsurface dynamics like equatorial Kelvin waves on TODS strengths can, in theory, also be transferred to other subsurface processes such as internal tides. Based on the presented results, it can be deduced that a good first estimate of TODS variations related to ocean processes impacting seawater temperature and salinity is obtained by assessing the variation of the depth-averaged conductivity ($\Delta\sigma_{mean}$) they cause. In view of existing studies that have investigated TODS variations

on long time scales (Saynisch et al., 2016, 2017), it is known that electrical seawater conductivity changes are mainly attributed to temperature variations. Consequently, ocean phenomena causing substantial changes in the seawater temperature distribution in the water column are the most likely candidates for significant TODS variations.

Identifying the conditions under which measurable TODS variations occur is an important step towards the goal of closing the ocean observation gap using TODS. The upcoming study maps and analyses the variation of modeled TODS that are based on time series of global in-situ seawater temperature and salinity observations. This way, ocean regions are identified where, unlike in the equatorial Pacific, σ_{mean} variations and TODS strengths combine in a way that leads to observable electromagnetic signal variations. Additionally, the study identifies conditions under which σ_{mean} changes are maximised and provides a first assessment of the time scales on which the rising ocean heat content or other processes lead to significant changes in the vertical distribution of seawater temperature and salinity. Lastly, the study provides an identification of ocean regions where seawater conductivity changes, e.g. seasonal variations, have the largest impact on TODS amplitudes.

5

ANALYSIS OF OCEAN TIDE INDUCED MAGNETIC FIELDS DERIVED FROM OCEANIC IN-SITU OBSERVATIONS — CLIMATE TRENDS AND THE REMARKABLE SENSITIVITY OF SHELF REGIONS

by Johannes Petereit[1, 2], Jan Saynisch[1], Christopher Irrgang[1], Maik Thomas[1, 2]

[1] GFZ German Research Center for Geosciences, Potsdam, Germany
[2] Freie Universität Berlin, Institute of Meteorology, Berlin, Germany

This paper has been published in JGR Oceans .

Abstract

Tidal motion of oceanic salt water through the ambient geomagnetic field induces periodic electromagnetic field signals. Amplitudes of the induced signals are sensitive to variations in electrical seawater conductivity and, consequently, to changes in oceanic temperature and salinity. In this paper, we computed and analyzed time series of global ocean tide induced magnetic field amplitudes. For this purpose, we combined data of global in-situ observations of oceanic temperature and salinity fields from 1990-2016 with data of oceanic tidal flow, the geomagnetic field, mantle conductivity, and sediment conductance to derive ocean tide induced magnetic field amplitudes. The results were used to compare present day developments in the oceanic climate with two existing climate model scenarios, namely global oceanic warming and Greenland glacial melting. Model fits of linear and quadratic long term trends of the derived magnetic field amplitudes show indications for both scenarios. Also, we find that magnetic field amplitude anomalies caused by oceanic seasonal variability and oceanic climate variations are ten times larger in shallow ocean regions than in the open ocean. Consequently, changes in the oceanic and therefore the Earth's climate system will be observed first in shelf regions. In other words, climate variations of ocean tide induced magnetic field amplitudes are best observed in shallow ocean regions using targeted monitoring techniques.

5.1 INTRODUCTION

Throughout Earth's history, the global climate changed drastically from extreme cold to extreme warm phases. Since ocean currents distribute heat from solar radiation throughout the globe, the ocean plays a central role in climate formation. The release of oceanic heat and humidity into the atmosphere is one of the driving forces for atmospheric circulation. Atmosphere and ocean dynamics impact each other mutually and form a complex dynamical system, which determines the global climate.

Global mean surface temperature (GMT) and ocean heat content (OHC) have risen over the last 50 years (Hansen et al., 2010; Levitus et al., 2012). Changes in ocean circulation, and therefore global heat transport, are the consequence. In order to monitor global climate variations, it is essential to observe oceanic processes continuously (Meyssignac et al., 2019).

In prinicple, global monitoring of climate variations can be achieved with observations of ocean tide induced magnetid field signals (Irrgang et al., 2019; Saynisch et al., 2016, 2017). Electric currents are induced by the motion of electrically conducting seawater through the ambient geomagnetic field (Irrgang et al., 2016b; Manoj et al., 2006; Minami, 2017). The strength of the induced electric currents and the corresponding magnetic fields is, among other influences, sensitive to changes in the electrical seawater conductivity (σ) distribution which is determined by oceanic temperature and salinity. That the oceanic σ distribution can be used to anticipate OHC with great precision and accuracy has recently been demonstrated by Trossman et al. (2019).

Tidal current induced magnetic field signals reach values of several nanotesla (nT) at sea level and satellite altitude (Kuvshinov, 2008; Minami, 2017). Due to the periodicity of the induced magnetic field signals, it has been possible to extract global distributions of radial semidiurnal principal lunar tide (M2) induced magnetic field ($B_{M2,r}$) amplitudes from satellite observations of the magnetic field missions CHAMP (Sabaka et al., 2015; Tyler et al., 2003) and Swarm (Sabaka et al., 2018, 2016). Additionally, Grayver et al. (2019) have successfully extracted the magnetic field signals of the tidal constituents N2 and O1 from combined data of both satellite missions. By means of an artificial neural network, it is possible to infer global ocean heat content values from these global ocean tide induced magnetic field amplitudes (Irrgang et al., 2019).

Ocean tide induced electric currents are sensitive to electrical seawater conductivity, tidal ocean flow, and the geomagnetic field. Out of these three, conductivity exhibits the highest temporal variability. In fact, variations of oceanic temperature and salinity occur on shorter time scales than changes in the tidal ocean flow or the geomagnetic field. This fact was used in recent studies that investigated $B_{M2,r}$ amplitude variations due to climate variations. On one hand, Saynisch et al. (2017) modelled the impact of the oceanic warming, caused by increased greenhouse gas content in the atmosphere, on the ocean tide induced magnetic fields. It has been found that, in general, $B_{M2,r}$ amplitudes increase with oceanic warming. On the other hand, motivated by Greenland glacial melting, Saynisch et al. (2016) have simulated a continuous freshwater influx in the arctic region which has lead to a breakdown of the Atlantic meridional overturning circulation (AMOC) in the model simulation. In contrast to the first study, altered heat transport and an increase in cold freshwater caused a decrease in $B_{M2,r}$ amplitudes.

Since, in both simulations the individual processes were investigated separately, it is currently unknown, whether one process will dominate or whether the two processes will annihilate each other in time. Moreover, it is unknown how the actual ocean climate influences $B_{M2,r}$ amplitudes and how variations in the amplitudes compare to modelled climate scenarios. Currently, there are no global magnetic field observations with the necessary precision and temporal resolution to answer that question by extracting $B_{M2,r}$ amplitude variations. But, the necessary global $B_{M2,r}$ amplitudes can be modelled, based on recent ocean state observations. In this study, we computed and analyzed a time series of monthly mean global $B_{M2,r}$ amplitudes for the years 1990 to 2016 based on global oceanic temperature and salinity observations. Dynamical changes in the resulting time series were then linked to recent ocean dynamics and compared to the findings of the preceding studies.

In section 5.2 we present the data and the methods used to compute the $B_{M2,r}$ amplitudes. The results of the subsequent analysis are presented in section 5.3 and discussed in section 5.4. We conclude and summarize this study in section 5.

5.2 DATA AND METHODS

Oceanographic in-situ observations

The oceanographic data needed to calculate recent changes in the ocean tide induced magnetic fields is provided by the Copernicus Marine Environment Monitoring Service (CMEMS). The Coriolis data set for Re-Analysis (CORA5.0, Cabanes et al. (2013)), with global monthly mean seawater temperature and salinity fields, is used to compute ocean tide induced electric currents and monthly mean oceanic conductance models.

In the CORA5.0 data set, in-situ measurements of observation techniques such as moored buoys (e.g. TAO/TRITON network (Hayes et al., 1991)), Argo floats (Roemmich et al., 2009), or gliders are used to estimate monthly mean temperature and salinity fields through a statistical analysis method, the In Situ Analysis System (ISAS) (Bretherton et al., 1976; Gaillard et al., 2016). The first guess for their estimation method was derived from the monthly climatologies of temperature and salinity distribution of the World Ocean Atlas (WOA) (Locarnini et al., 2013; Zweng et al., 2013). The WOA climatologies for periods between 1985-1994,1995-2004, and 2005-2012 are interpolated to provide monthly temperature and salinity fields centered at the 15th of each month. After applying an objective analysis, the resulting fields contain dynamical changes on inter-annual, inter-seasonal and monthly time scales from 1990 to 2016 on a $0.5^\circ \times 0.5^\circ$ grid. The data is distributed on 152 vertical levels between the sea-surface and a depth of 2000 m.

The in-situ observation coverage is low in the first 10 years of the considered period, but increases with the progressive deployment of Argo-floats. Almost no data is available in the polar regions, which have been shown to be highly susceptible to climate variations (Saynisch et al., 2016, 2017). In the highly dynamic, and for this study crucial, region of the northern Atlantic, by contrast, data coverage is particularly high. In case of unavailable profile data, the provided values are equal to the first guess, which is equal to the temperature and salinity fields of the World Ocean Atlas.

Conductivity model

The conductivity model is composed of a time-constant spherically symmetric 1-D mantle conductivity (Grayver et al., 2017) placed below a thin spherical electrical conductance layer. The spherical layer combines the time-constant sediment conductance with the time-variable ocean conductance. The sediment conductance is calculated with the method of Everett et al. (2003) using sediment thicknesses from Laske et al. (1997).

This study uses monthly mean ocean conductance fields that contain monthly, inter-seasonal and inter-annual variability. There are pre-computed global σ distributions available (Tyler et al., 2017). These data sets have been compiled with the highest possible consistency in ocean data in mind assuring that only temperature and salinity were used that were measured at the same place and time. However, these distributions present average climatologies and lack the necessary inter-annual variability and long-term trends needed to analyze the relation between the underlying changes in ocean dynamics and the ocean tide induced magnetic field signals. Hence, we computed the monthly mean ocean conductance from the oceanic seawater temperature and salinity distribution of the CORA5.0 data set with the following three-step algorithm:

First, we derived the 3D oceanic conductivity distribution down to a depth of 2000 m from the CORA temperature and salinity fields (cf. section 5.2). The conductivity was computed with the Gibbs-Seawater equation, specifically, the conductivity function of the TEOS-10 toolbox (IOC et al., 2010). The ocean pressure p needed for this calculation was approximated as $p \approx h$ in dbar. Here, h is the depth of the individual data point given in m. Subsequently, the monthly conductivity was depth-integrated down to 2000 m depth to obtain oceanic conductance fields of the upper ocean.

Second, the global ocean conductance from sea-surface to ocean bottom was computed by adding the deep ocean conductance for depths below 2000 m to the upper ocean conductance (cf. step one). The deep ocean conductance was obtained by integrating the global conductivity distribution of the World Ocean Atlas for the years 1981 to 2010, from 2000 m to ocean bottom (Tyler et al., 2017).

Third, the obtained monthly ocean conductance fields were depth-averaged (σ_{mean}) first and then multiplied with the bathymetry of the TPXO8-atlas (Egbert et al., 2002). This way, we removed the influence of the coarse bathymetry resolution of the WOA in the global ocean conductance fields.

Furthermore, this step assures consistency between the conductance and the ocean tide induced electric currents. The latter rely on the tidal flow of the semidiurnal ocean tide M2, which was also taken from the TPXO8-atlas (cf. section 5.2).

The final monthly mean ocean conductance fields have a regular grid with a resolution of $0.5° \times 0.5°$. All necessary input fields have been interpolated bi-linearly to fit this regular grid before applying the algorithm.

Electric current

The Lorentz force acts on seawater that flows through the ambient geomagnetic field. As a consequence, an electric current is induced. We compute the electric current sheet density $\vec{j}_{M2}$ induced by the tidal ocean currents of the semidiurnal principal lunar tide M2 with Ohm's Law:

$$\vec{j}_{M2}(\varphi, \vartheta) = \sigma_{mean}(\varphi, \vartheta) \left(\vec{V}_{M2}(\varphi, \vartheta) \times \vec{B}_{Earth}(\varphi, \vartheta) \right). \tag{5.1}$$

Here, φ and ϑ are longitude and co-latitude. σ_{mean}, $\vec{V}_{M2}$ and $\vec{B}_{Earth}$ are the depth-averaged conductivity (cf. section 5.2), the tidal ocean transport of the M2 tide, and the geomagnetic field, respectively.

For the tidal flow of the M2 tide $\vec{V}_{M2}$, we use the barotropic flow provided by the TPXO8-atlas (Egbert et al., 2002). The geomagnetic field $\vec{B}_{Earth}$ is based on the international geomagnetic reference field IGRF-12 (Thébault et al., 2015). We follow the approach of the Greenland glacial melting study (Saynisch et al., 2016) and the oceanic warming study (Saynisch et al., 2017) and assume a time-constant $\vec{B}_{Earth}$. This assures better comparability between the findings of all three studies and puts the focus on the oceanic causes of $B_{M2,r}$ variability. However, the influence of the secular variation on $\vec{j}_{M2}$ should be considered when the data set of this study is compared to actual $B_{M2,r}$ observations. Since the variations in the geomagnetic field are well known (Gillet et al., 2010), their effects can be removed.

Induction solver x3dg

The time-varying electric currents induced by the oceanic tidal motion produce time-varying magnetic fields. These magnetic fields in return interact with their electrical conducting environment and induce secondary electric currents, which produce further magnetic fields and so forth. This mech-

anism and additional electromagnetic phenomena such as galvanic effects and currents induced parallel to conductivity boundaries are described by Maxwell's equations.

Maxwell's equations have no analytical solution in a general three dimensional environment. With the numerical 3-D induction solver x3dg of Kuvshinov (2008), we compute the electromagnetic response to interactions of ocean tide induced currents and the heterogeneous electrical conducting environment. x3dg solves Maxwell's equations in the frequency domain using an iterative contracting volume integral equation approach (Pankratov et al., 1995; Singer et al., 1995). The solver has been shown to simulate electromagnetic fields of models with sharp contrasts and complicated geometries in an efficient and accurate manner (Kelbert et al., 2014; Sachl et al., 2019). The solver is forced with the computed monthly ocean tide induced electric currents and conductance distributions (Velímský et al., 2018).

The resulting ocean tide induced electromagnetic fields (B_{M2}) are computed at sea level and satellite altitude with a spatial resolution of 0.5°. The B_{M2} fields can be expanded into poloidal and toroidal magnetic modes with the Helmholtz decomposition (Chave et al., 1990). While toroidal magnetic fields are confined inside the ocean and the sediments, poloidal magnetic fields are measurable outside of the ocean as the radial magnetic field amplitudes $B_{M2,r}$ (Dostal et al., 2012). Recent studies have shown that lateral conductivity variations allow an exchange of energy between the magnetic modes (Velímský et al., 2019). In this study however, we focus solely on $B_{M2,r}$ and do not show the remaining electromagnetic field components.

5.3 RESULTS

Mean seasonal variations of averaged radial ocean tide induced magnetic field amplitudes

Amplitudes of the radial ocean tide induced magnetic field components $B_{M2,r}$ were averaged over the entire time span covered by the CORA data set. The resulting global distribution of averaged M2 induced magnetic field amplitudes is shown in figure 5.1. The distributions at sea level and satellite altitude are consistent with the findings of previous studies (Grayver et al., 2016; Kuvshinov, 2008; Sabaka et al., 2016; Saynisch et al., 2016, 2017; Tyler et al., 2003).

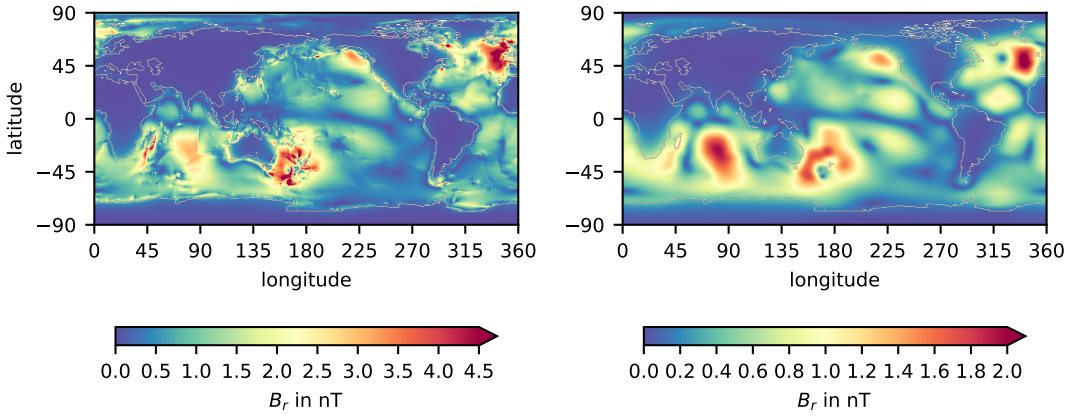

Figure 5.1: Amplitudes of the radial magnetic field component induced by the oceanic M2 tide. Temporal average over the whole time span from 1990 to 2016. The amplitudes at sea level (left) reach higher magnitudes and are more detailed in their lateral structure. At satellite altitude (right), the amplitudes have decreased in magnitude. Also, the influence of small-scale structures with high amplitudes at sea level vanishes due to the upward continuation of the signals.

There are 4 large areas with amplitudes greater than 3.0 nT at sea level and 1.4 nT at satellite altitude. The strongest maximum is located around New Zealand with values of up to 6.9 nT (1.7 nT at satellite altitude). In the northern Atlantic $B_{M2,r}$ amplitudes reach values of 5.7 nT (2.1 nT), while in the Indian Ocean and the northern Pacific values of 3.0 nT (1.9 nT) and 3.3 nT (1.4 nT) are reached.

Additionally, there are multiple small scale regions with high amplitudes at sea level but moderate amplitudes at satellite altitude. Around Madagascar, for example, $B_{M2,r}$ amplitudes reach values of 4.1 nT and in the Bering Sea, close to the Aleutian Islands, they reach values of 5.7 nT. Furthermore, $B_{M2,r}$ amplitudes close to the Hudson Straight estuary in the Labrador Sea reach maximum values of 4.2 nT. These values are comparable to those occurring off the coast of Nova Scotia with maximum values of 3.7 nT. With increasing altitude, the magnitude of $B_{M2,r}$ amplitudes decreases and the lateral fine-scale structures fade until the large scale patterns dominate and overshadow small scale patterns. The small scale patterns are therefore better detectable at sea level (cf. figure 5.1).

In the next step, we calculated a climatological mean annual cycle from the $B_{M2,r}$ time series. The local peak-to-peak difference of the cycle represents the statistical annual modulation of $B_{M2,r}$ amplitudes and is shown in figure 5.2. Areas with large peak-to-peak difference are most affected by the seasonal cycle. The computed spatial distribution of seasonal am-

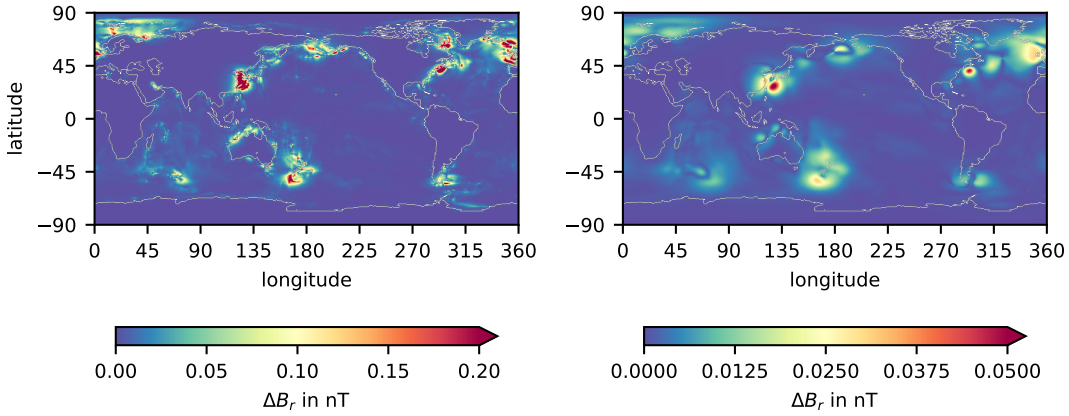

Figure 5.2: Seasonal peak-to-peak difference of radial ocean tide induced magnetic fields based on climatology derived from CORA5.0 at sea level (left) and satellite altitude (right).

plitude variations at satellite altitude is consistent with the one of Grayver et al. (2016).

At sea level, the largest seasonal peak-to-peak differences are found in the Yellow Sea ($\Delta B_{r,mean} \leq 0.54$ nT) and Gulf of Maine ($\Delta B_{r,mean} \leq 0.68$ nT). Since the mean signal in these regions is in the order of 1.0 nT, the seasonal variation represents relative changes of $\propto 10\%$. Off the coast of New Zealand, the Labrador Sea and off the European Atlantic coast, we also find high seasonal $B_{M2,r}$ variations with values of more than 0.3 nT.

The range at satellite altitude is about ten times lower and reaches $\approx$ 0.05 nT in the Yellow Sea and the Gulf of Maine. Around New Zealand and the northern Atlantic the seasonal variations reach up to $\approx$ 0.03 nT. There are several reasons against the extraction of seasonal $B_{M2,r}$ amplitude variations at satellite altitude. The absolute magnetometers of the Swarm mission have a nominal accuracy of $<$ 0.045 nT (Jager et al., 2010). Furthermore, lunar tidal forces induce additional electromagnetic signals in the ionosphere (Matsushita, 1967) in the same frequency range which have to be separated correctly. And last but not least, recent studies relied on more than 18 month of satellite data to extract global $B_{M2,r}$ amplitude fields (Grayver et al., 2019; Sabaka et al., 2018, 2016, 2015; Tyler et al., 2003). Consequently, the accuracy and precision of the available data as well as the temporal sampling are momentarily too low for the task at hand.

Indications for Climate Variation

The oceanic temperature T and salinity S fields of the CORA5.0 data set are the only time-varying input in our experimental setup. The changes of S and T cause variations of the depth-averaged seawater conductivity σ_{mean} which leads consequently to variations in the current-sheet density of the ocean-tide induced electric current $\vec{j}_{M2}$ (cf. equation (5.1)) and the global conductance model (cf. section 5.2).

We have computed the correlation (r) between the time series of σ_{mean} and the principal lunar tide induced radial magnetic field component $B_{M2,r}$ at sea level and satellite altitude for each grid point (cf. figure 5.3). This way we are able to assess the linearity of the relation of the input and output variables. We find that r is generally close to 1 in most ocean regions. In some small regions, however, the correlation coefficient is either negative or close to 0. These exceptions are mostly found in regions with low $B_{M2,r}$. With the continuation of $B_{M2,r}$ in radial direction up to satellite altitude, the correlation decreases slightly but retains a high level.

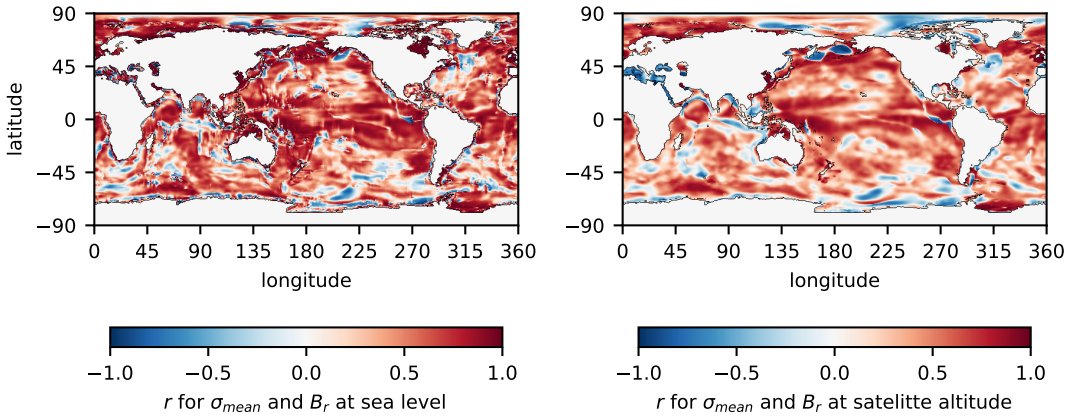

Figure 5.3: Pearson correlation coefficient r of σ_{mean} and B_r at sea level (left) and at satellite altitude (right).

Changes in oceanic conductivity can be attributed, in large part, to changing seawater temperature distributions (Saynisch et al., 2016; Tyler et al., 2017). The seawater temperature distribution is closely related to the ocean heat content, a well-known indicator for the global climate state (Meyssignac et al., 2019) which has been subject of many studies (Hansen et al., 2010; Levitus et al., 2012, 2001; Loeb et al., 2012). It is in first order proportional to the depth integrated seawater temperature of the upper 2000 m (Levitus et al., 2012) of the ocean; the depth for which observations are available from the Argo program (Roemmich et al., 2009). We calculated the corre-

lation between the time series of σ_{mean} and T_{int}, the seawater temperature integrated from a depth of 2000 m to sea surface, at each grid point (cf. figure 5.4) and found that T_{int} and σ_{mean} are virtually proportional in the majority of ocean regions. The correlation of both quantities is practically 1 throughout the world ocean except for regions at the immediate coast and the arctic ocean. In some parts of the cold Arctic ocean we find, that the changes in σ_{mean} correspond better to the depth-integrated seawater salinity S_{int} (cf. right side of figure 5.4). This is explained with the fact that temperatures in that region are quite constant while the salinity exhibits much higher variability than most ocean regions. This is due to effects caused by ice formation and melting processes as well as the supply of freshwater due to glacial melting. This is in agreement with the findings of Trossman et al. (2019) who previously have investigated the high correlation between OHC and σ_{mean}.

Following the presented evidence, we conclude that our findings for OHC or the comparable T_{int} are also true for σ_{mean}. Additionally, we conclude that the relation of OHC and $B_{M2,r}$ is also in first order linear in most ocean regions. This makes not only the OHC and σ_{mean} but also $B_{M2,r}$ a good indicator for the oceanic climate state.

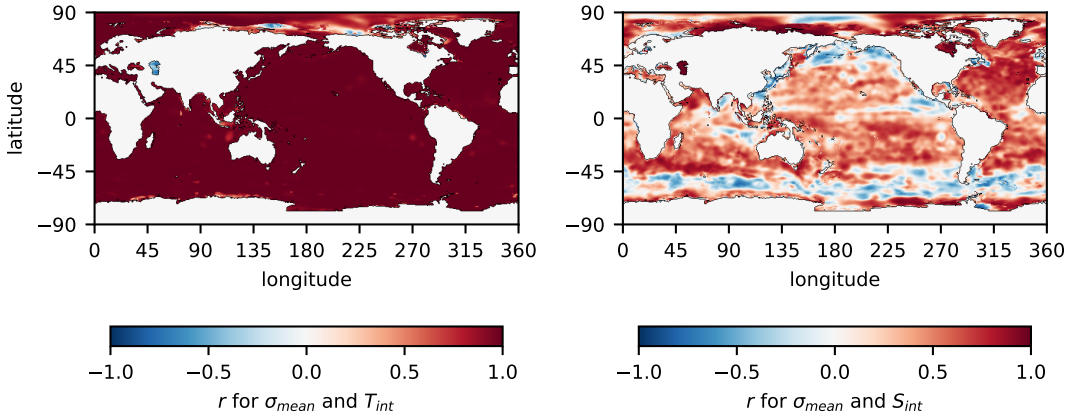

Figure 5.4: Pearson correlation coefficient r of σ_{mean} and T_{int} (left) and S_{int} (right).

In order to assess developments in the ocean climate and compare these to the presented Greenland glacial melting (Saynisch et al., 2016) and oceanic warming (Saynisch et al., 2017) scenarios, we computed long term trends of the depth integrated temperature T_{int}, σ_{mean} and $B_{M2,r}$. In detail, we have carried out a linear regression to fit the linear model

$$f_i = a_1 \cdot t_i + a_0. \tag{5.2}$$

Here, f_i is the modelled value at time t_i. This way, we have obtained the linear trend a_1 for the entire time series (cf. figure 5.5).

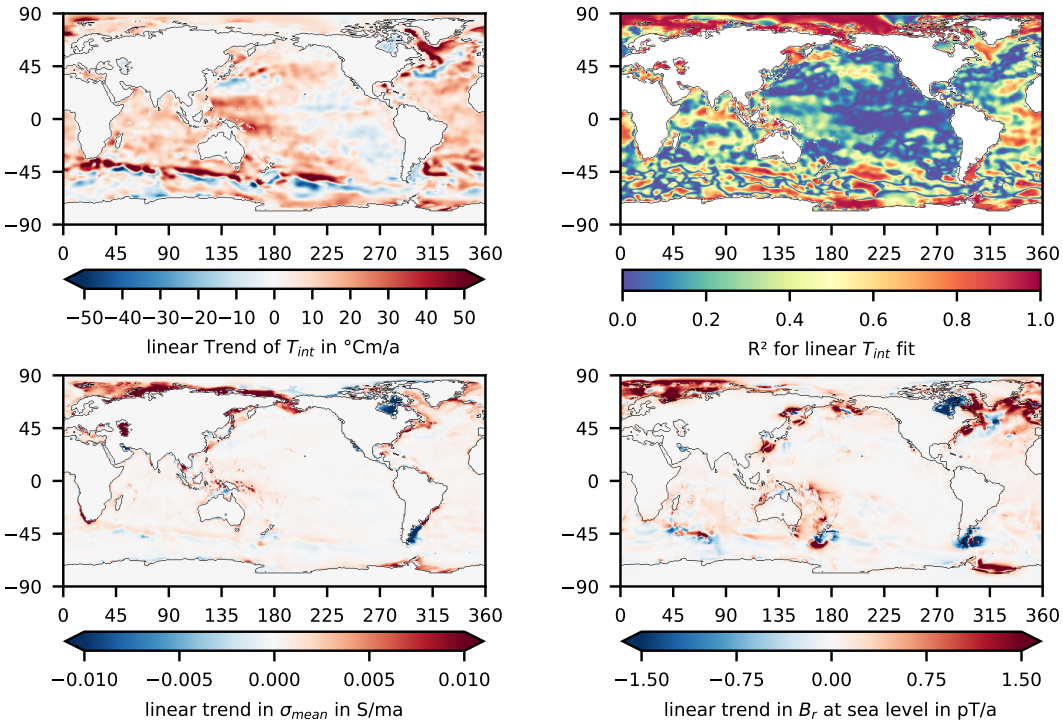

Figure 5.5: Linear trend in T_{int} (top left) and the corresponding coefficient of determination R^2 (top right). The linear trends in σ_{mean} (bottom left) and $B_{M2,r}$ at sea level (bottom right) follow the trend in the depth integrated temperature T_{int} but express larger differences in their magnitude between coastal regions and the open ocean.

We have also carried out a polynomial regression of second order to fit a quadratic model

$$f_i = b_2 \cdot t_i^2 + b_1 \cdot t_i + b_0 \tag{5.3}$$

and obtain the quadratic trend b_2 of the time series (cf. figure 5.6). a_1 and b_2 are the coefficients of the terms that will dominate the dynamic of their model in time, due to the leading exponent. In our study, b_2 is about ten times smaller than a_1. Consequently, if the quadratic trends persist, they will dominate ocean dynamics on decadal time scales.

The coefficient of determination R^2 provides a measure of how well the observed values are explained by a model and is defined as:

$$R^2 := 1 - \frac{\sum_i (y_i - f_i)}{\sum_i (y_i - \bar{y})}. \tag{5.4}$$

Here, $\bar{y}$ is the mean of the observed values y_i and f_i is the value modelled with the respective regression fit. In order to increase the significance

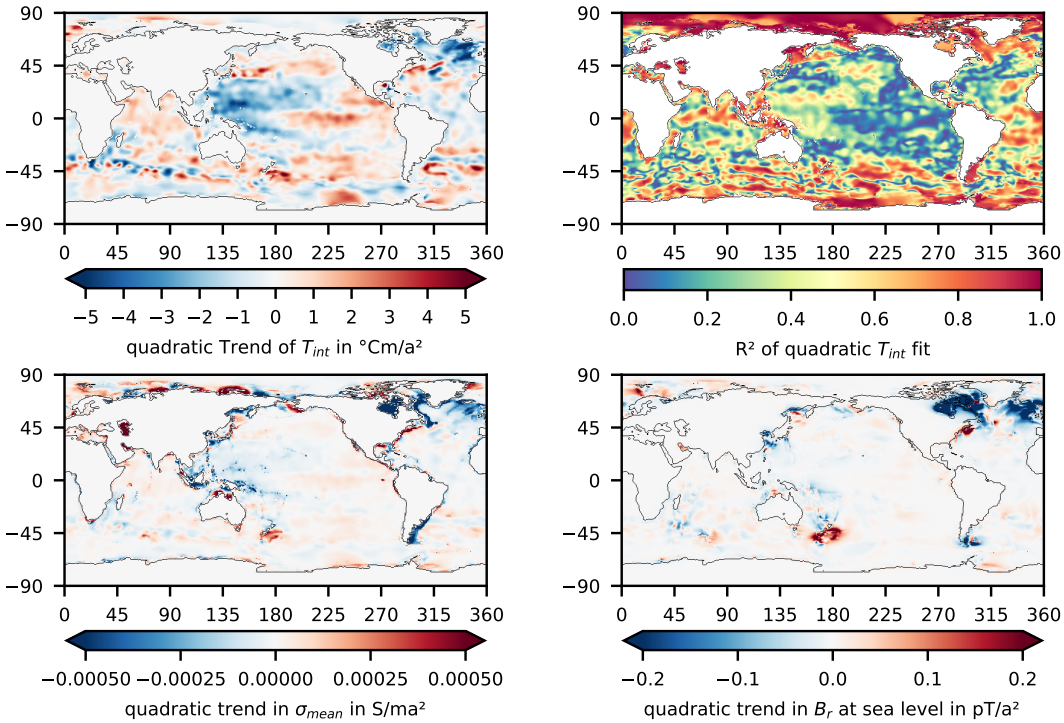

Figure 5.6: Quadratic trend in T_{int} (top left) and the corresponding coefficient of determination R^2 (top right) along with the quadratic trends in σ_{mean} (bottom left) and $B_{M2,r}$ at sea level (bottom right).

of R^2, we removed seasonal and high-frequency variations by applying a 12-month running mean. As a consequence, the magnitude of R^2 is increased and the decision of whether the linear or the quadratic model fits the long-term ocean dynamics better is facilitated. Due to the high correlation of $B_{M2,r}$, σ_{mean} and T_{int}, this report only illustrates the R^2 coefficient for the T_{int} model (cf. figure 5.5 and figure 5.6). The R^2 coefficients of the models for $B_{M2,r}$ amplitude and σ_{mean} dynamics exhibit a very similar global distribution (not shown).

The distribution of signs in T_{int}, σ_{mean} and $B_{M2,r}$ trends are in good agreement. This is in accordance to the high correlation of these quantities in most ocean regions (cf. figure 5.3 and figure 5.4). Despite this high correlation, there is a significant difference in the magnitude distribution in the respective trends. The magnitude of T_{int} trends is almost uniformly distributed across the global ocean. By contrast, σ_{mean} and $B_{M2,r}$ trends are about ten times larger in the shallow shelf regions than the open ocean. This is also found for the magnitude distributions of seasonal variations in $B_{M2,r}$ (cf. figure 5.2).

The complex dynamical system of the global ocean circulation, and thus of the ocean heat distribution, exhibits high variability. The dynamics are

too complex to be modelled with simple linear or quadratic dynamical models on longer time scales. The dynamics of the equatorial Pacific Ocean, for example, is largely dominated by the influence of the El Niño/Southern Oscillation. In this region, R^2 values of both trend models are especially low. Neither the linear model nor the quadratic model can adequately represent the dynamic in this region. However, there are ocean regions, where ocean heat dynamics are well explained with one of these simple models.

The Arctic ocean, the Sea of Okhotsk, the area around the Aleutian Islands, the western coast of South America, and the Weddell Sea are examples for regions for which the linear model is a good fit. That is why we find large R^2 coefficients for this model in these regions (cf. figure 5.5. Additionally, the linear $B_{M2,r}$ trends in these ocean regions are relatively large, surpassing 2 pT/a at sea level (0.5 pT/a at satellite altitude). The trends in these regions are all positive, except for trends off the western coast of South America. Here, the OHC increases gradually in time. This agrees well with known OHC trends (Cheng et al., 2016; Levitus et al., 2012). However, the large part of ocean dynamics is poorly explained with a linear model.

The signs of b_2 and a_1, the leading exponents in the individual models, are opposed in most ocean regions. This indicates trend reversals, an acceleration or deceleration of the observed trend, or a saturation effect. In most regions, we also find a substantial increase of the R^2 coefficients for the quadratic model (cf. figure 5.6). This increase indicates that the dynamics in these regions regions are better fitted with the quadratic model. But only in regions where R^2 is close to 1 for the quadratic model, we can assume that T_{int}, σ_{mean} and $B_{M2,r}$ dynamics are well explained by the model.

In the northern Atlantic, south of Greenland, we find an initial increase in T_{int}, σ_{mean} and $B_{M2,r}$ over the first 15-20 years of the investigated period. However, after the tipping point between 2005 and 2010 we find a rapid decrease in both quantities. This is well represented in the fitted models. For the linear models, we find large positive trends in T_{int}, σ_{mean} and $B_{M2,r}$, which account for the long period of increase. However, due to a reversal of the trend we find low R^2 coefficients for the linear fit. The trend reversal and the subsequent rapid decrease explain the large negative values for the quadratic T_{int}, σ_{mean} and $B_{M2,r}$ trends and the increase in R^2 coefficients. This is also in agreement with the positive linear trends b_1 (not shown). Consequently, the linear trend of the quadratic fit dominates on shorter time scales while on longer time scales the negative quadratic trend

prevails. A similar dynamic, with reversed signs, can be on the continental shelf of New Zealand.

5.4 DISCUSSION

In the following we discuss effects that were neglected in our analysis but have to be taken into account when investigating actual magnetometer observations.

OHC changes in an ocean depth below 2000 m were not taken into account in this study. However, the majority of the total OHC is stored above 700 m and the small fraction of OHC originating from depths below 2000 m increases comparatively slow (Cheng et al., 2016). In addition, the variability of oceanic temperatures and salinity is higher in the upper ocean than in the deep ocean. Consequently, no significant changes are expected when including deep ocean salinity and temperature variations of the considered time period.

The large scale temporal variability of the geomagnetic field and the tidal ocean flow have also been neglected. It is known that the amphidromic system is robust with regards to changes in sea level and oceanic temperatures (Saynisch et al., 2016) in the majority of ocean regions. Consequently, in those regions long-term changes in tidal amplitudes can be neglected. However in coastal regions, oceanic warming and sea level rise has a considerable impact on M2 tidal amplitudes. Seasonal warming, for example, increases coastal M2 tidal amplitudes up to 5 % (Müller et al., 2014). The subsequent increase in the tidal flow, determined by the tidal amplitude and ocean depth, should in principle cause even larger seasonal $B_{M2,r}$ variations than those found in section 5.3.

Comparison to climate projections

There are two studies investigating the relation between oceanic climate variations and $B_{M2,r}$ anomalies. In the first study, Saynisch et al. (2017) analysed the effects of oceanic warming, due to increased greenhouse gas content in the atmosphere, on $B_{M2,r}$ amplitudes. An initial mean annual ocean state was modelled and compared to terminal mean annual ocean states that were projected 96 years into the future. The terminal mean annual ocean states were modelled with an ocean general circulation model.

The ocean model was forced with atmospheric data of a selection of atmospheric warming scenarios from CMIP5 (Taylor et al., 2012). The resulting oceanic warming caused $B_{M2,r}$ anomalies of up to 0.3 nT at sea level. The areas with largest $B_{M2,r}$ amplitude increase were the northern Atlantic, the Arctic Ocean, the Pacific region surrounding New Zealand, the Labrador Sea, the Gulf of Maine, and the northwestern Pacific. In the Hudson Bay, by contrast, $B_{M2,r}$ amplitudes decreased by a comparable magnitude.

In Saynisch et al. (2016), the second study, the authors investigated the effect of Greenland glacial melting on the ocean tide induced magnetic field. Ongoing Greenland glacial melting was modelled with an increased freshwater influx in the northern Atlantic. The fresh water hosing experiment resulted in a breakdown of AMOC and large scale changes in the oceanic temperature and salinity distribution. The AMOC breakdown occurred within a time period of 50-100 years. Again, the final and terminal mean annual ocean climate state were compared and revealed mostly negative $B_{M2,r}$ anomalies. At sea level, the fresh water hosing caused a decrease in $B_{M2,r}$ amplitudes in large areas around New Zealand and in the northern Atlantic. In those regions anomalies were in the order of 0.1 nT with a maximum value of 0.7 nT.

The distribution of positive and negative linear $B_{M2,r}$ matches the expectations of the oceanic warming induced $B_{M2,r}$ anomalies modelled by Saynisch et al. (2017). The linear trends (cf. section 5.3) reach amplitudes of more than 2 pT/a in the regions where the largest $B_{M2,r}$ anomalies are expected, according to the oceanic warming scenario. Consequently, extrapolating the linear trends 100 years into the future results in $B_{M2,r}$ anomalies of more than 0.2 nT. Therefore, the changes of OHC are within the expected range. Despite the high correspondence of the linear trends and the modelled $B_{M2,r}$ anomalies of the oceanic warming study, the dynamics in the region of the northern Atlantic are better explained with a linear model.

In this study, the observed dynamics of $B_{M2,r}$ amplitudes in the northern Atlantic are well explained with the quadratic model (cf. section 5.3). The long-term trends indicated by the negative b_2 match the findings of the Greenland glacial melting study. The b_2 coefficients for the quadratic $B_{M2,r}$ model at sea level reach values of more than 0.2 pT/a^2. For the quadratic model, with b_2 coefficients about ten times smaller than b_1 coefficients, the leading exponent will dominate the dynamic on decadal time scales. Assuming that the prospective course of the dynamics in the Northern Atlantic follows the fitted dynamic, it would take about 28 years to cause

anomalies of 0.1 nT and about 55 years to cause anomalies of 0.5 nT. Neglecting the ten times larger positive b_1 trends, this time would be reduced to about 22.5 years and 50 years, respectively. Consequently, the quadratic trends of the quadratic model also match the expected changes in OHC.

In the northern Atlantic ocean region, ocean dynamics are highly variable and cause high variability in oceanic temperature and salinity (McCarthy et al., 2015). It is also a crucial region for the global climate, because of the poleward heat transport in the Atlantic, which is unique among global oceans (Bryden et al., 2001). In the northern hemisphere, up to one quarter of global poleward atmosphere-ocean heat transport is carried by the Atlantic Meridional Overturning Circulation (AMOC). On one hand, the better fitting negative quadratic model and the decrease of AMOC during 2009-2010 for a time period of 14 months (Bryden et al., 2014) are arguments for the Greenland glacial melting scenario. On the other hand, the consistent increase in global OHC and global mean surface temperatures are in favor of the oceanic warming scenario.

The trends of both fitted models indicate developments in the ocean climate state which could lead to anomalies similar to the two presented climate scenarios. However, in the preceding studies only anomalies of the initial and the final ocean climate states have been investigated. The ocean dynamics leading to these anomalies have been neglected. By contrast, the present study investigates the dynamical changes of present day OHC and $B_{M2,r}$ amplitude variations. In consideration of the high variability of the complex ocean dynamics, especially in the North Atlantic, the investigated time period is too short to make reliable predictions for prospective ocean dynamics. The $B_{M2,r}$ amplitude changes observed in the northern Atlantic could be caused by an impending break down of AMOC but also by a temporary weakening. Additionally, the combined effects of oceanic warming and Greenland glacial melting on $B_{M2,r}$ amplitudes is currently unknown. Consequently, a longer time series of data is necessary to decide which one of the possible scenarios will prevail.

Climate sensitive shelf regions

The extraction of $B_{M2,r}$ amplitudes from magnetometer observations is a challenging task. The ocean tide induced magnetic signals are minute compared to other magnetic signals. Additionally, seasonal variations and trends in $B_{M2,r}$ amplitudes are even smaller and their detection can not be

assured for the immediate future. However, if $B_{M2,r}$ amplitude variations caused by ocean heat variations are detected, they are most likely detected in shallow ocean regions. $B_{M2,r}$ amplitudes show higher sensitivity to ocean climate variations in the shelf seas compared to the rest of the ocean. The highest seasonal variability of the $B_{M2,r}$ amplitudes (cf. figure 5.2) and the largest magnitude of long term $B_{M2,r}$ trends are found in coastal regions (cf. figures 5.5 and 5.6). This is consistent with $B_{M2,r}$ anomalies modelled in the oceanic warming and the Greenland glacial melting study (Saynisch et al., 2016, 2017).

Despite the fact that ocean depth in shelf regions is one order of magnitude lower than in the open ocean, there is no significant difference in the magnitudes of $B_{M2,r}$ amplitudes and the tidal ocean transports between those two regions. For the tidal transports in shelf regions, the shallow ocean depth is compensated by high tidal current velocities. As a shallow water wave, the phase velocity of the tidal wave is proportional to the square root of the ocean depth $\sqrt{h}$. However, the tidal current velocity is proportional to the product of $\sqrt{g/h}$ and the tidal elevation amplitude A (Stride, 1983). A itself is proportional to $\sqrt[-4]{h}$. Consequently, as the tidal wave approaches the shelf, tidal wave speed decreases but amplitude and current velocity increase, due to energy conservation. This explains why ocean depth has only little influence on $B_{M2,r}$ and V amplitudes, but does not explain the differences in $B_{M2,r}$ sensitivity of the two ocean regimes.

The only time-variable input in our experiment design are the oceanic temperature and salinity fields. They are the only possible cause for trends and anomalies in $B_{M2,r}$ (cf. equation (5.1)). The tidal transports V_{M2} show only small dependence on variations of ocean depth, salinity, and temperature. The geomagnetic field B_{Earth} is independent of those quantities. This means that the increased $B_{M2,r}$ variability in shelf regions must be caused by σ_{mean} variations due to changes in the oceanic temperature and salinity distribution.

σ_{mean} values are more extreme in shelf regions compared to the open ocean. For shelves in the mid-latitude, σ_{mean} is much higher than in the deep ocean. This relation reverses in high latitudes (cf. Saynisch et al. (2016), Trossman et al. (2019), and Tyler et al. (2017)). However, the extreme values do not explain the increased sensitivity of σ_{mean} and $B_{M2,r}$ towards changes in T_{int}. Neither large temperature nor salinity changes are limited to shelf regions. In the equatorial Pacific, for example, the El Niño/Southern Oscil-

lation causes large temperature and salinity anomalies which again cause only minor σ_{mean} and $B_{M2,r}$ anomalies (Petereit et al., 2018).

Temporal trends of T_{int} and therefore OHC are in the same order of magnitude throughout the world ocean. By contrast, the temporal trends of the highly correlated σ_{mean} are ten times larger in shallow ocean regions (cf. figures 5.5 and 5.6). This is explained with the fact, that the amount of heat, necessary to increase the average conductivity in the water column in shelf region, is about ten times smaller than the amount of heat needed to cause a similar change in the open ocean. Consequently, the depth averaged seawater conductivity σ_{mean} is more sensitive to temperature and salinity changes in shallow ocean regions than in the open ocean. That is why, the impact of oceanic temperature related phenomena like seasonal thermocline depth variations or oceanic warming on σ_{mean} and consequently $B_{M2,r}$ is ten times larger in shelf regions than in the open ocean.

5.5 SUMMARY AND CONCLUSIONS

In previous ocean tide induced magnetic field signal studies, it was investigated how the processes of Greenland glacial melting (Saynisch et al., 2016) and oceanic warming (Saynisch et al., 2017) affect climate sensitive ocean tide induced magnetic field ($B_{M2,r}$) amplitudes in time. The findings of these studies showed opposing effects on $B_{M2,r}$ amplitudes. Therefore, in this paper we investigated how present day developments in ocean climate influence $B_{M2,r}$ amplitudes and how the present day $B_{M2,r}$ amplitude developments compare to the modelled climate scenarios. From global monthly mean seawater temperature and salinity fields, we derived a time series of global monthly mean $B_{M2,r}$ amplitudes for the years of 1990 to 2016. From the obtained $B_{M2,r}$ time series, we inferred the seasonal variability and fitted linear and quadratic trend models. This way, we assessed long-term trends in $B_{M2,r}$ amplitudes.

The linear $B_{M2,r}$ trends correspond well with the $B_{M2,r}$ anomalies caused by oceanic warming. However, these trends are in conflict with the in-situ observations in the North Atlantic ocean region. Here, $B_{M2,r}$ signals increase until a tipping point is reached towards the end of the first decade of the new millennium. Afterwards, $B_{M2,r}$ amplitudes decrease continuously. This temporal development fits better to the dynamic of a quadratic model. The quadratic fit supports the findings of the Greenland glacial melting study.

Additionally, we show that ocean heat content (OHC) and $B_{M2,r}$ are highly correlated. Consequently, the found long-term $B_{M2,r}$ trends show that recent developments in OHC are within the expected range set by the two climate scenarios. In order to come to a final decision in this matter, a continuous monitoring of either OHC or ocean conductance variations is necessary. Due to the high correlation, the radial ocean tide induced magnetic field amplitudes are a suitable observation technique for this task.

The presented variations in $B_{M2,r}$ amplitudes caused by changes in OHC are very small. It is already challenging to extract $B_{M2,r}$ amplitudes from magnetic field observations. There are further electromagnetic phenomena such as solar quiet variation or lunar tides in the ionosphere in the same frequency range. Additionally, the magnitude of the presented variations is, in most ocean regions, below the current accuracy of most magnetometer measurements. We show that their detection will most likely be realized in shallow ocean regions. Changes in electrical seawater conductivity caused by variations in oceanic temperature and salinity distribution lead to ten times larger $B_{M2,r}$ amplitude variations in shelf regions than in the deep ocean. In the shelf regions, depth-averaged electrical seawater conductivity σ_{mean} and $B_{M2,r}$ amplitudes show high sensitivity to seasonal variations and long-term climate trends. This is explained by the fact that ocean heat variations leading to σ_{mean} changes scale with the depth of the water column. Thus, the effect of seasonal thermocline depth variations on σ_{mean}, for example, is ten times larger in shelf seas than in the ten times deeper open ocean. The corresponding $B_{M2,r}$ amplitude anomalies in the shelf regions are also approximately one order of magnitude higher than in the deep ocean.

The seasonal $B_{M2,r}$ variability has to be taken into account when $B_{M2,r}$ amplitudes are to be extracted from magnetometer observations. A temporal averaging over a time span other than a multiple of the seasonal cycle would impose a bias. However, the current satellite magnetometer precision is too low and extracted $B_{M2,r}$ amplitudes might be unaffected by the mentioned bias.

However, there are several additional observation techniques which allow a monitoring of ocean tide induced electromagnetic field components, like terrestrial magnetometer stations. Coastal sea-floor voltage cables (Baringer et al., 2010; Kuvshinov et al., 2006; D. J. Thomson et al., 1986) or ocean-bottom magnetometer (Guzavina et al., 2018; Schnepf et al., 2015,

2014; Shimizu et al., 2011) even allow detection of components other than $B_{M2,r}$.

We conclude, that oceanic shelves are not only the regions where $B_{M2,r}$ amplitudes are most affected by oceanic climate variations, but also the regions where these climate variations will become observable as $B_{M2,r}$ variations first. Consequently, a targeted monitoring of ocean tide induced magnetic fields in shelf regions is beneficial for the monitoring of changes in oceanic and therefore Earth's climate. As a next step, it is planned to extract seasonal and long-term $B_{M2,r}$ amplitude variations from coastal magnetometer observations to test the presented results.

The second study attempts to reconcile conflicting TODS forecasts by modelling, analyzing and extrapolating contemporary TODS developments. In doing so, the study contributes insights to physical TODS characterization and provides a deepened understanding of the link between ocean dynamics and TODS amplitude variations. In the following, two main findings of the study will be highlighted and put into a broader context.

First, the study demonstrates, in the first order, a linear relation between depth-averaged seawater conductivity variations ($\Delta\sigma_{mean}$) and TODS amplitude variations in most ocean regions. Also, $\Delta\sigma_{mean}$ variations are mainly attributed to changes in the depth-integrated seawater temperature and therefore heat content. This supports the found relation of seawater temperature and conductivity variations of Saynisch et al. (2016) and stresses the role of temporal changes in the oceanic heat distribution for TODS based ocean observations. This is further supported by the study of Irrgang et al. (2019) which infers global ocean heat content from global TODS amplitude observations. However, the contribution of their study to the field of ocean observations is limited since there is a significant difference between changes in the integrated global ocean heat content and the dynamics of oceanic heat distribution. While global ocean heat content changes reflect on the energy balance within the greenhouse effect leading to global warming, the spatial heat distribution, redistribution and subsequent changes in the local water column reflect on ocean dynamics on a smaller scale.

Second, the study also demonstrated that in shelf regions TODS amplitude variations are expected to reach values of more than 10% on annual time scales. Existing studies investigating the impact of changes in global seawater temperature and salinity distributions on TODS consistently confirm this increased sensitivity of shelf regions (Saynisch et al., 2016, 2017). On the other side, Irrgang et al. (2016b) concluded that seasonal seawater and temperature variations only have a minor impact on the electrical seawater conductivity. However, their comparison of local conductivity values does not account for the accumulation of changes in the depth-averaged conductivity σ_{mean}.

In consideration of these findings and the fact that the link between ocean dynamics and TODS variations has mainly been investigated with model studies on global scales, empirical evidence is needed to validate the findings of the previous study. Even more so, since findings in coastal regions through global ocean modelling are possibly affected by approach-dependent artifacts. Furthermore, there is a standing problem of a measurable offset between modeled and observed TODS amplitudes in coastal proximity (Maus et al., 2004; Schnepf et al., 2016). Whether this offset can be resolved with advances in TODS modelling or signal processing in order to extract and observed TODS is to this date undecided. For these reasons, the third study investigates which conditions must be fulfilled to measure temporal TODS variations on short time scales and provides the first steps towards a solution to these standing challenges.

6

ON TEMPORAL VARIATIONS OF COASTAL TIDAL OCEAN-DYNAMO SIGNALS

by Johannes Petereit[1,2], Jan Saynisch-Wagner[1],
Achim Morschhauser[1], Leonie Pick[1], Maik Thomas[1,2]

[1] GFZ German Research Center for Geosciences, Potsdam, Germany
[2] Freie Universität Berlin, Institute of Meteorology, Berlin, Germany

This version of the article has been accepted for publication, after peer review but is not the Version of Record and does not reflect post-acceptance improvements, or any corrections.

The Version of Record is available online at:
https://doi.org/10.1186/s40623-022-01610-9.

Abstract

The movement of seawater in the ambient geomagnetic field meets all requirements for motional induction processes, the working principle of a dynamo. Periodic tidal ocean currents induce electric currents and, therefore, magnetic field signals that are not only observable using spaceborne and terrestrial observation techniques, but can, in theory, also be used to monitor oceanic temperature and salinity variations. Tidal magnetic field amplitudes and phases have been extracted from magnetometer measurements, but their temporal variations have not yet been identified and analyzed. In this study, we characterize seasonal variations and long-term trends in the 10 year magnetometer time series of three coastal island observatories. We demonstrate that existing approaches, i.e., subtraction of core field models or first order differencing, are unable to reliably remove low-frequency contributions. We hence propose a novel approach and demonstrate its advantages over existing approaches. By spectral analysis of the processed

data, we determine signal and side peak magnitudes of the M2 tide induced magnetic field signal and find evidence for seasonal magnetic field signal variations of roughly 10% to 25% from the annual mean. Additionally, we apply various signal extraction techniques to identify tidal ocean-dynamo signal amplitudes and phases in sub-series of the 10 year time series with incrementally increasing lengths. The analyses support three main findings: (1) trends cause signal amplitude changes of up to $\approx$ 1 nT and phase changes are in the order of $\mathcal{O}(10^{\circ})$ within the observation period; (2) at least 4 years of data are needed to obtain reliable amplitude and phase values with the extraction methods used and (3) signal phases are a more robust measurand than signal amplitudes.

6.1 INTRODUCTION

There are two fundamental electromagnetic induction principles: motional and magnetic induction. While magnetic induction describes the generation of electric currents through temporal changes in the magnetic flux of an ambient magnetic field, motional induction describes the generation of electric currents through the movement of charge carriers within an ambient magnetic field. The latter is not only the working principle of a dynamo or generator, but generates also electric currents in the ocean. There, electrically charged particles (salt ions) move relative to an ambient magnetic field (the geomagnetic field). The Lorentz Force, acting on the charge carriers, deflects positive and negative salt ions in opposing directions and generates thus electric currents. The electromagnetic (EM) field signals emitted by these currents have been studied in the context of different ocean phenomena such as: mass transport (J. C. Larsen et al., 1985; Sanford, 1971) and heat flux estimations (J. C. Larsen et al., 1992) of ocean currents, the identification and analysis of EM signals generated by Eddies (Lilley et al., 1993) or passing Hurricanes (Sanford et al., 2007). Naturally, studies of ocean-dynamo signals are not limited to ocean currents and the general ocean circulation (Glazman et al., 2005; Irrgang et al., 2016a,b; Manoj et al., 2006; Vivier et al., 2004), but include also studies of Tsunamis (Minami et al., 2021, 2015; Schnepf et al., 2016; Toh et al., 2011) and ocean tides (Malin, 1970; Maus et al., 2004; Petereit et al., 2018; Tyler et al., 2003). A comprehensive overview of the recent research in this field was given by Minami (2017).

Despite the general interest of ocean-dynamo signals, tidal ocean-dynamo signals (TODS) are the only ones that have been observed from space. Since the first successful magnetic signal extraction of the semidiurnal principal lunar tide (M2) from CHAMP data by Tyler et al. (2003), additional partial tides (N2, O1) have also been successfully extracted (Grayver et al., 2019; Sabaka et al., 2016). Simultaneously, the time series length for a successful signal extraction could be reduced from initially 12 years (Sabaka et al., 2015) to tens of months (Sabaka et al., 2016). This is attributed to an increased measurement accuracy and improved measurement setup of the Swarm mission allowing for a higher spatial-temporal coverage. This reduction in required measurement time allows for a global observation of temporal changes of these signals.

The signal strength of TODS is determined by three factors: the electrical seawater conductivity σ, the tidal current velocities v, and the Earth's magnetic field strength B_{Earth}. In the open ocean, changes in the amphidromic system and magnetic field are slow compared to changes in the conductivity distribution which is determined by seawater salinity and temperature. As a result, TODS inferred from satellite data can be used to observe large-scale changes in the oceanic conductivity distribution. These prospects, and the fact that state of the art model predictions of M2 TODS (Velímský et al., 2018) agree well with satellite observations (Grayver et al., 2019; Sabaka et al., 2015), inspired model-based investigations of the effect of conductivity changes on TODS. Such studies consider conductivity changes caused by, e.g., (a) global warming scenarios (Saynisch et al., 2017), (b) a possible collapse of the Atlantic Meridional Overturning Circulation (AMOC) and a subsequent redistribution of cold and warm water masses (Saynisch et al., 2016) or (c) cold and warm surface water anomalies caused by the El Nino Southern Oscillation (ENSO) (Petereit et al., 2018).

Far off the coast (Schnepf et al., 2018) and at the ocean bottom (Schnepf et al., 2014), M2 TODS identified in magnetometer observations are also in good agreement with model predictions. In coastal regions, this is different. Maus et al. (2004) and Schnepf et al. (2018) have extracted TODS from coastal island magnetometer data and found significant differences when compared to model data. At the moment, there are only speculations about causes for this discrepancy like insufficient model resolutions, unmodelled coastal phenomena or long range effects. It is well-known that the variability in the conductance, i.e. the depth-integrated conductivity, is larger in shallow shelf regions than in the open ocean. This can be explained with

the difference in the ratio of thermocline depth to total water column depth (Petereit et al., 2019). As a consequence, coastal TODS amplitudes vary significantly on seasonal to decadal time scales. This is caused by mainly two effects. On the one hand, seasonal thermocline depth variations (Petereit et al., 2019) cause conductance deviations of $\approx 10\%$ from the annual mean. On the other hand, thermosteric variations lead to tidal velocity amplitude changes in the order of 10% (Müller et al., 2014). In theory, both effects accumulate and cause even larger seasonal TODS variations. Furthermore, in coastal regions, nonlinear effects are known to alter the sinusoidal shape of shallow tidal waves. The impact on coastal TODS is currently unknown.

To take a first step towards the goal to unify observations with model predictions, we build on the work of Maus et al. (2004) and Schnepf et al. (2018) and attempt to identify temporal TODS variations. The above mentioned high TODS variability of coastal TODS on seasonal time scales is momentarily not observable with spaceborne techniques. This is due to the necessary observation period length of more than a year. Besides, small scale features of TODS are not captured at satellite altitude. The EM signal decay with distance ($\propto 1/r^2$) implies that large scale features dominate at satellite altitude (Grayver et al., 2016).

Hence, in this study we analyse time series data of 10 years length from three island magnetometer observatories, namely Ascension Island (ASC), the Crozet Archipelago (CZT) and San Juan on Puerto Rico (SJG). This paper is divided into four parts. In the first part, we present the selection criteria together with a novel data processing method to filter low-frequency signals of electromagnetic phenomena in the data (section 2). In the second part, we conduct a spectral analysis on the unevenly sampled residual data to validate the advantages of our data processing method in comparison to existing processing methods (section 3). Also, we attempt to identify seasonal M2 TODS variations in the hyperfine structure of the obtained spectra. In the third part, we apply three existing approaches used to identify M2 TODS in magnetometer observatory data. The results are subsequently compared to asses the robustness of our results and estimate uncertainties (section 4). In the final part of the presented study, we put our findings into context of other studies and discuss opportunities for future studies (section 5).

6.2 DATA SELECTION & PROCESSING

6.2.1 *Data Selection & Filtering*

For this study, we analysed time series of magnetic field observations from island coastal magnetometer stations found in the INTERMAGNET catalogue (Love et al., 2013). The time series cover the 10-year period 2005 - 2015. The sampling rate for all analyzed time series is one observation per minute. The chosen stations are situated on Ascension Island (ASC), the Crozet Archipelago (CZT) and San Juan on Puerto Rico (SJG) and were selected through the following criteria. First, the islands lie in ocean regions with high M2 TODS amplitudes (Kuvshinov, 2008) so that the challenge of identifying these signals and their variations becomes less demanding. Second, the coastal proximity of the stations assures a good signal to noise ratio which is a precondition for reliable signal extraction. It also increases the chance of detecting seasonal TODS variations anticipated by Petereit et al. (2018). Third, the stations deliver the magnetic field component pointing vertically down (Z, in local Cartesian or cylindrical frames). This direction is the only magnetic field direction carrying the ocean-dynamo signal outside of the ocean (Dostal et al., 2012). Due to the computational costs of the following analysis, we limited our choice to three stations.

Signals of various magnetic field sources, such as signals of Earth's lithosphere and core, or of currents in the ocean, ionosphere and magnetosphere, are integrated in magnetic field measurements. However, signal strengths and typical time scales of natural electromagnetic phenomena cover multiple orders of magnitude. While amplitudes of tidal ocean-dynamo signals reach values below 10 nanotesla (nT), Earth's geomagnetic core signals reaches magnitudes of more then 60000 nT. The current standard approach for the extraction and subsequent analysis of ocean-dynamo signals is to preprocess the data by removing modelled signals (Maus et al., 2004; Schnepf et al., 2018; Tyler et al., 2003).

The strength and variability of the coupled magnetosphere-ionosphere current systems are relatively small during so-called quiet conditions, i.e., the absence of geomagnetic (sub-)storm activity. Much work has been invested into the development of geomagnetic activity indices on the basis of which global/local quiet conditions may be identified (Kp, Dst or Rc index) (Kauristie et al., 2017). We follow the lead of Grayver et al. (2019) and

Schnepf et al. (2018) and identify these quiet conditions with the criteria that Kp$<$ 2 and $\|$dDst/dt$\|$ $<$ 2nT/h.

Remaining ionospheric signals like the solar quiet (Sq) current system or ionospheric tides are largest on Earth's dayside. During the night, the conductivity of the ionosphere plummets to $\approx 1/30$th of its dayside value (Malin, 1970). We consequently limit our work to the analysis of nightside data. Following the approach of Maus et al. (2004), we identify night-side data by identifying time windows in which the average magnetic signal strength is lowest (ASC (6 hour window) : 9 pm - 3 am; CZT (7 hour window): 5 pm - 12 pm; SJG (6 hour 141 window) 0 am - 6 am (in universal time UTC)). There is also the possibility to identify nightside data as observations when the solar elevation angle (Woolf, 1968) is several degrees (usually 10) below the horizon (Grayver et al., 2019). We applied both approaches and found that the first worked better for us due to the existence of ionospheric activity close to the equator shortly before sunrise.

6.2.2 *Removal of low-frequency variations*

After the data processing, the largest contributor to the remaining signal is the core magnetic field and its temporal variation (secular variation). Removing these signals is necessary to isolate the high-frequency TODS and leverage the full advantage of their periodicity for the subsequent analysis. In long time series, periodic signals are easily identified and separated with high accuracy when long term variations are absent. The reliability of the separation, however, depends on the number of cycles included in the time series. Since we are searching for variations of amplitudes and phases in time, we have to assure that these variations cannot be attributed to other sources.

The influence of slow variations in the observed magnetic field has been dealt with in different ways, in the past. For short time series, i.e., in the range of months, it has been assumed that these influences are negligible and have therefore been approximated as constant in time (Schnepf et al., 2018). For time series in the range of a few years, slow variations have been accounted for by including long frequencies in the harmonic analysis (Schnepf et al., 2014). This however does not account for non-periodic slow variations such as the secular variation and is thus not suitable for the case at hand.

In the following, we will apply three different approaches.

Removal by magnetic field model subtraction

The removal of magnetic field components of Earth's core can be achieved either with the subtraction of model predictions for all components. Some examples for available magnetic field models are the CHAOS (Finlay et al., 2020, n.d.), GRIMM (Lesur et al., 2010, 2008) and Kalmag (Baerenzung et al., 2020) models but also the International Geomagnetic Reference Field (IGRF) (Alken et al., 2021; Thébault et al., 2015), a composite of such individually developed models. Please note, some of this models include the time constant contribution of Earth lithosphere while others do not, e.g. the IGRF. Consequently, the elimination of the magnetic field contribution has to be handled differently depending on the chosen model. Like Grayver et al. (2019), we also subtracted the CHAOS model predictions (Version 7.6) from the filtered data. Other models deliver comparable results for island observatory data.

Subtracting a geomagnetic field model is a reasonable and reliable approach for global magnetometer observations obtained from satellite missions such as Swarm or CHAMP. At satellite altitude a lot of the spatial TODS variability has vanished due to the invert-square law of EM field propagation.

Removal by first order differencing

Another approach to the problem is using time series analysis (TSA) methods. Typically, TSA methods analyse the statistical properties of stationary time series, i.e., time series with time constant statistical properties such as the average or variance. One method to transform non-stationary time series, like the time series at hand, into a stationary time series is called differencing (Blackman et al., 1958a,b; R. E. Thomson et al., 2014).

By subtracting successive magnetic field observations $y(t_i)$:

$$\Delta y(t_i) = y(t_{i+1}) - y(t_i)$$

we obtain a time series of differences $\Delta y(t_i)$ that is "pre-whitened", i.e., the power was shifted from lower to higher frequencies and the trend thus removed. This way we not only remove the trends but also highlight the tidal frequencies, the focus of our study. Depending on the characteristics of the trend, differences of higher orders need to be applied. In our case, first or-

der differencing, i.e., differencing once, sufficed to remove low-frequency components.

Differencing can also be applied to remove seasonality, i.e., periodic signals, in time series data. Instead of subtracting neighboring data points, data points are subtracted that are separated by the period in question. For our purposes only the slowly varying trend was removed and the periodic signals remained. In the context of magnetic field data analysis, the same technique was applied by Love et al. (2014) in their analysis of the *magnetic tides* of Honolulu. In their study, *magnetic tides* are the diurnal variation of geomagnetic field observations during solar quiet times, a signal combining oceanic and ionospheric signals. For consistency reasons, we only included differences on neighboring data points, if the time passed between both observations was 1 minute. Differences at data gaps created by the previously described selection procedure were omitted.

Removal by smoothing spline subtraction

A third option for removing slow variations in time series is filtering the data with smoothing splines (Craven et al., 1978). Splines, especially cubic splines, are rigid, smooth and easy to compute. Also, they are uniquely identified by the number and position of their knots. It is consequently easy to identify two extreme cases for splines fitted to data. The first is the interpolation spline. It passes through every given data point and is therefore overfitting the data. The other extreme is the linear spline which is equivalent to a linear regression curve and therefore only capable of removing linear trends. Linear trends however do not account for the complex temporal development of the secular variation. It is possible to balance between both extremes and identify a cubic spline function with an equidistant knot distribution which fits well to the data but is, due to the rigid characteristics of the splines, not overfitting the data. The smoothing condition is defined as

$$\sum_i \left(y(t_i) - spl(t_i)\right)^2 \leq s \cdot N, \tag{6.1}$$

where $y(t_i)$ is the magnetic field observation and $spl(t_i)$ the value of the smoothing spline at a given time t_i and N the total number of observations and s the smoothing parameter.

The smoothing parameter s, however, should depend on the noise level of a given time series. Consequently, the identification of a suitable s to filter time series with differing noise levels to a chosen cut-off frequency is not

automated easily and has to be calibrated by hand. To assure consistency in the smoothing, for the analysis in section 6.4, we filtered each 10-year time series in total instead of filtering individual sub-series separately. For the chosen station data, we chose s to filter out signals with periods longer than 10 days which resulted in s values of 2.3 (ASC), 16.5 (CZT) and 45.5 (SJG). To our knowledge, this method was not yet applied in the context of M2 TODS identification.

6.3 SPECTRAL ANALYSIS

A standard method to asses the periodic variation of time series is to interpret the power spectrum or periodogram. In evenly spaced time series, a power spectrum can be computed with the efficient Fast Fourier Transformation (FFT). The applied data processing (cf. section 6.2) removes the disturbing signals but leaves an unevenly spaced time series. The analysis of such time series is common practice in the field of astrophysics where observations depend on external factors like cloud coverage. A standard method to compute a periodogram was developed by Lomb (1976) and later refined by Scargle (1982), the Lomb-Scargle Periodogram (Press et al., 2007; VanderPlas, 2018). The Lomb-Scargle method is more demanding on computational resources and time than the FFT method but the efficiency of the available implementation has dramatically improved since the algorithm was first developed (Harris et al., 2020; Virtanen et al., 2020).

The Lomb-Scargle Periodogram helps to estimate the spectral power of a harmonic signal of a given frequency. For the data processing it was used to identify suitable values for the smoothing parameter s by visualizing its impact on the periodogram. However, since it relies essentially on a least squares algorithm it inherits also its weaknesses. Also, the obtained values in the periodogram do not represent the power but a detection probability normalized with the variance of the input data. Despite the fact that the detection probability is closely related to the signal power and signal to noise ratio, the obtained values can consequently not be directly translated into physically meaningful values. However, they are still helpful to identify periodic signals (peaks) and their temporal variation (side bands).

6.3.1 *Comparison of Data Processing Procedures*

The above mentioned spectral analysis allows us to compare the periodograms of the residual data after applying the three detrending methods (cf. Fig. 6.1). Judging from the signal peaks found in all images, the dominating signal found in the residual data is the daily variation. This can be inferred from the existence of prominent peaks at periods of an integer fraction of one solar day, in Fig. 6.1 marked with S_n. The combination of the S_n signals signify the daily variation which can be attributed to solar causes.

There are two kind of tides: gravitational and radiatonal or thermal tides. For gravitational tides, the largest signal is usually the semidiurnal principal lunar tide M2. This is because the gravitational pull of the moon makes up, depending on the relative position of the sun and the moon on their individual orbits, 2/3 to 3/4 of the total tidal force. Thermal tides originate from the differential heating of the sun during night and day. Peaks labeled with S_n are probably of the latter type (see Fig. 6.1). Because of the dissimilar distribution of solar radiation during night and day, the daily variation is usually non-sinusoidal. It can however be deconstructed into a Fourier series with peaks at higher orders, i.e., multiple frequencies of S_1, like these found in our residual data. That these signal peaks can be found in the nightside data provokes different theories about their origin. One explanation is that filtering the data with a fixed local time is not sufficient given that sun rise and sun set vary seasonally. Another explanation is that there are still slowly decaying ionospheric signals present during night time. The persistent nature of these signals in all analysed time series indicates that the taken measures are insufficient for a clean separation of radiational and gravitational tidal EM signals.

Comparing the spectra by trend removal method applied, i.e., comparison by column in figure 6.1, we can assess the suitability of the detrending methods. We find that subtracting the geomagnetic field model reduced the slow variations but failed to remove them completely. Residual low-frequency signals in the same order of magnitude as the tidal signal peaks remain. While the approach has been proven to be successful for the extraction of TODS from satellite data, it appears to be unsuitable for regional applications. Comparing the spectra at each station after subtracting CHAOS, we find large S_n signal peaks only in ASC. For the other two stations, S_n signals are much smaller. A possible reason are remaining ionospheric signals in the ASC time series.

For the first order differencing, we can clearly observe the successful removal of slow variations in at least two of the three stations (CZT and SJG). We can also confirm the pre-whitening effect as the signal power in higher frequencies has increased in comparison to the previous method. In the data from Ascencion Island however, we find signs of an annual (Sa), semi-annual (Ssa) and a monthly synodic fortnightly (MSf) variation as well as a residual low frequency variation. These peaks substantiated the suspicion that the residual daily variation of the magnetic field has not been sufficiently removed from the data. The daily magnetic field variation caused by the ionosphere is not only stronger than the oceanic signal but it is also known to be sensitive to seasonal variations, Earth's orbit around the sun (Canton, 1759), the sun magnetic activity cycle (Sabine, 1857) and the lunar cycle (Broun, 1874; Kreil, 1852). All these influences could in principle contribute to the identified signals. An additional argument for the origin of residual signal of the ionosphere is that the MSf signal which typically corresponds to the spring-neap-tide frequency is usually quite small in comparison to other gravitational tidal constituents (Cartwright et al., 1971). Then again, on shallow coastal regions, there are nonlinear tidal effects which could cause the MSf tide to be a prominent tidal constituent (Pugh, 1987). However, given the absence, at least relative to the signal strength of the MSf tide, of the MSm and the Mf tide, it is unlikely that the MSf signals are induced by oceanic processes. Ionospheric processes are the most likely candidate, especially when Love et al. (2014) have found comparable signals in their analysis of the daily geomagnetic variation.

The third detrending method, the subtraction of a smoothing spline has successfully removed low frequencies, while leaving high frequencies practically uninfluenced. The proposed data processing reliably removed periods below the threshold of $f = 0.1\ \mathrm{d}^{-1}$ or above $T = 10\mathrm{d}$ respectively. This allows the separation of all periodic signals in the subsequent signal extraction (c.f. section 6.4) in a time series of the given length.

Additionally, we want to emphasize the dependence of the detected signal peaks in the frequency range above $1\ \mathrm{d}^{-1}$ on the detrending method. This becomes particularly clear when comparing the sidebands of the signal peaks of the solar tides, or the peaks of higher orders. When substracting CHAOS, the peak distribution exhibits a significantly different characteristic than found in the spectra obtained with the other two detrending methods. Since the foundation of the Lomb-Scargle method is the least squares fitting of sinusoidal functions of different frequencies to a given

time series (VanderPlas, 2018), we conclude that the chosen data processing also has an impact on the basic detectability of periodic signals. By removing virtually all slow variations, we can detect the periodic signal peaks and characterize the individual distribution of each island magnetometer observation easier. In consequence, the attained data quality of the residual time series data fulfills the necessary precondition for the subsequent analysis of signal extraction methods.

Comparing the spectra by station, i.e., comparison by row in figure 6.1, we find that noise levels and spectral peak distribution are unique for every observatory. This is reasonable since the oceanic and ionospheric tidal causes depend on geographic position.

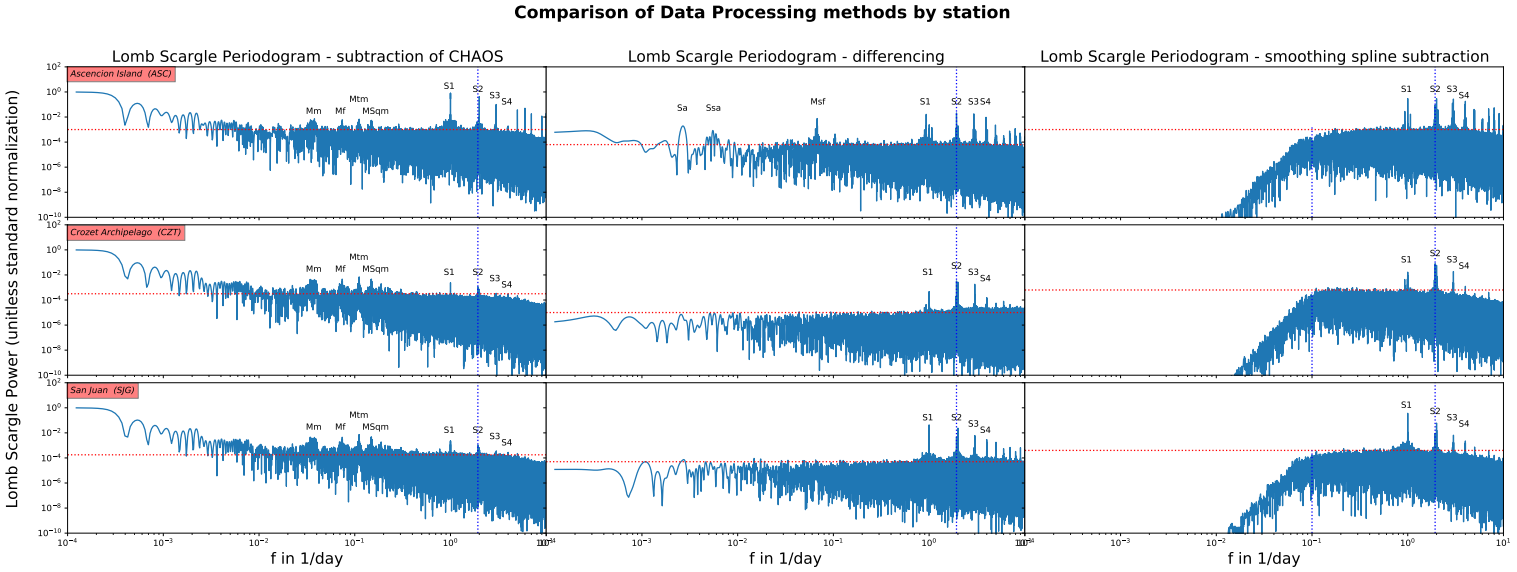

Figure 6.1: Lomb-Scargle Periodograms of the residual time series data at all three analyzed Intermagnet stations ASC (top row), CZT (middle row) and SJG (bottom row)). In each column a different removal technique was applied: the subtraction of the model prediction of the CHAOS model (left), differencing of subsequent data points (middle) and the substraction of a smoothing spline (right). Dotted red lines indicate an estimation of the noise level. The dotted blue lines visualize the frequency of the prinicipal lunare tide M2. Other prominent frequency peaks or well-known tidal frequencies are marked with their tidal code, e.g. Sa, Ssa or Mf. The halved dotted blue lines in the right column indicate the targeted cut-off frequency for the smoothing spline (10^{-1} d^{-1}). The amplitudes, noise level and distribution of significant peaks vary as expected with the location due to differing coastal, oceanic and geographical conditions. However, the distribution of detected periodic signals and their signal strength varies with the chosen processing method.

6.3.2 *Indications for periodic M2 Signal Modulation*

From the results obtained in the previous section, we conclude that non-oceanic causes for the signal peaks can not be completely excluded, especially for solar tides. Therefore, we refrain from an in depth analysis of the fine spectral structure. Instead, we analyse the hyperfine structure around the signal peak of the semidiurnal principal lunar tide M2 to identify signs for its seasonal amplitude variation (c.f. figure 6.2). To assure robustness in our findings, we compare the residual spectra produced by differencing and smoothing spline subtraction respectively. Unlike the subtraction of CHAOS, both methods successfully removed slow variations so that their spectra seem more conclusive.

From the fields of signal processing and spectral analysis we know that amplitude and phase variations of a periodic signal can cause side bands (Blackman et al., 1958a,b). A prominent application for this is the analysis of tide gauge data where oceanic tides are decomposed into various tidal species. Oceanic tides are mainly gravitational tides which are caused by the interaction of the Earth with the Moon and the Sun. There are various components that are caused by the periodic variations in the interacting forces due to elliptical and mutually tilted orbits, and rotational axis of the celestial bodies (Doodson, 1928; Hendershott et al., 1970). Additional examples are beat interference and amplitude modulation. The beat interference is created by two signals with a frequency difference much smaller than the average frequency of both. The frequency of the enveloping signal is similar to the frequency difference of the original signals. The simplest form of the amplitude modulation is described as the periodic modulation of a periodic carrier signal which creates symmetric side peaks left and right to the carrier peak frequency. It is a phenomenon well known in the field of signal processing and led to the development of AM (amplitude modulation) radios.

In addition to amplitude and phase variations, there exist other effects impacting the analysed spectra like the sampling rate or the time series length. Please be aware, that for the Lomb-Scargle method the Nyquist theorem does not apply (VanderPlas, 2018) so that in theory resolutions below the Nyquist frequency can be achieved. For our analysis, we aimed for a high resolution which was achieved by sampling each spectra signal peak with 25 frequencies. A higher sampling did not have any effect on the spectra. In the obtained spectra, the M2-signal peaks and the side

peaks associated with annual variations, i.e., at the $f_{M2} \pm f_{Sa}$ frequencies, appear rather broad and show signs of additional variations. The amount of available data, however, is insufficient for a clean separation of these signal peaks. It is reasonable to assume that the natural occurring global interannual variability in the weather is also reflected in TODS. Anyhow, it remains to be determined whether these indications for additional variability are artefacts or actual signals originating from periodic variation, trends or a statistical variability.

When comparing the spectra, both detrending methods used provide highly similar results. The detection probability level of the peaks is higher for the smoothing spline subtraction method, but apart from that the distribution and proportion of signal peaks are comparable. In all spectra we find an asymmetric side peak distribution around the frequencies corresponding to an annual variation ($f = f_{M2} \pm f_{Sa}$) indicating a modulation of both, amplitude and phase. There are weak signs for side peaks corresponding to a semiannual modulation ($f = f_{M2} \pm f_{Ssa}$). Since, f_{Ssa} is a higher harmonic of f_{Sa}, this is a possible sign for an asymmetric annual modulation. The signal strengths of the possible Ssa signal side peaks, however, is more than one order of magnitude smaller than the M2-signal peak. It is therefore unlikely that there is a noticeable semi-annual variation in the M2 TODS. On the other hand, the ratio of the M2 signal peak and the side peak found at $f = f_{M2} + f_{Sa}$ are $\approx$ 3% (ASC), $\approx$ 25% (CZT) and $\approx$ 10% (SJG) respectively. The combined signal of M2 signal peak and the side peaks should in principle add up to a comparable annual variation of the M2 TODS amplitude. Causes for M2 TODS amplitudes variations on annual time scales are variations in ocean tidal velocity amplitudes, and in the seawater temperature and salinity distribution. For a possible validation of these findings both effects need to be taken into account.

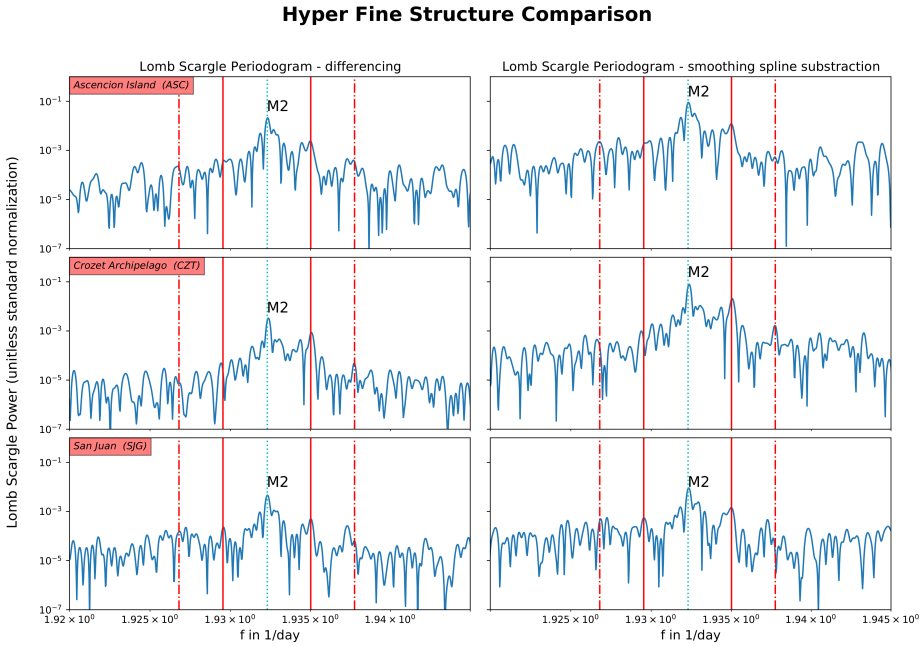

Figure 6.2: Comparison of highly resolved periodograms of the M2 TODS peaks at all three analyzed Intermagnet stations ASC (top row), CZT (middle row) and SJG (bottom row). While the left column shows the spectra obtained after first order differencing, the right column shows the results after smoothing spline subtraction. The dotted blue lines mark the frequency of the semidiurnal principal lunar tide M2. Solid red lines mark side band frequencies associated with an annual variation (Sa) and red dot-dash lines mark side band frequencies associated with a semiannual variation (Ssa). When comparing the left and the right column, we find the hpyerfine structure around the M2 TODS peaks to be independent of the method used for trend removal.

6.4 TRENDS IN M2 TIDAL SIGNALS

In addition to seasonal M2 TODS amplitude variations, we are also interested in long-term trends like the ones investigated by Petereit et al. (2019). With the achieved level of signal peak separation, a definite identification of increasing or decreasing signal amplitudes with time is not possible. In addition to a higher resolution, it would also require the analysis of the distributions of real and imaginary components around the M2 TODS peak which is not provided with by the Lomb-Scargle Periodogram. The analysis of the power spectra alone is thus insufficient to determine long-term trends.

To analyse trends in the M2 generated signal amplitudes, we divide the preprocessed 10 year time series into sub-series of increasing lengths

and applied three different methods to analyse signal amplitudes. This approach yields insights about the dependence of extracted signal amplitudes on the quantity of available data, but also indications for the temporal variation of M2 TODS. Considering the challenge of separating the M2 TODS from the residual data, it also allows to assess the overall robustness of the resulting amplitudes and phases.

For our analysis, we rely on the precondition that low-frequency signals were removed from the data. If not, the signals may not be separable from the data. The detrending methods of subtracting the geomagnetic field model and first-order differencing have not produced the desired results, especially for the data obtained at Ascension (ASC) (c.f. figure 6.1). For this part of the study, we rely thus on the residual data obtained after the subtraction of the smoothing spline.

In the following, we present the three methods used to extract TODS amplitudes from the residual data together with the obtained results.

6.4.1 *Data Phasing*

The first method we applied to identify M2 TODS amplitudes is called phasing. In this method, each data point is transformed to a new time coordinate related to the phase of the M2 oscillation. The continuous time axis is thereby transformed into a periodic time axis of M2 period length (12h and 25 min). The now overlapping data points are averaged for each minute on the axis. We computed the averages using the arithmetic mean and the median.

The unique period lengths of the different tidal components create an ever-growing phase shift between the M2 and other tides with each completed oscillation. Assuming that TODS are symmetrical oscillations around the zero value, the signals of tidal constituents other than multiples of the M2 tide are canceled out in the averaging process in long time series. If we further assume that the noise is normally distributed with zero mean, only the mean signal of the M2 tide will remain in the averaging process. From the obtained sinusoidal curve, we estimate the amplitude as the halved peak-to-peak difference .

Although the method is easily implemented and delivers fast results, there are several drawbacks. Due to the assumptions, it is only applicable with an appropriate preprocessing of the observational data. Also, the smoothness of the obtained sine shaped average signal depends on the

length of the considered time series, the signal to noise ratio and the presence and strength of residual signals. Consequently, when analysing long time series signal separation becomes more accurate and the influence of seasonal and inter annual variation decreases, the sinus shaped average signals thus get smoother with time. Furthermore, the method does only provide a rough estimate of the average amplitude but does not account for a possible phase shift of the M2 TODS. This means that in long time series, an increase in the amplitude may be masked by a phase shift.

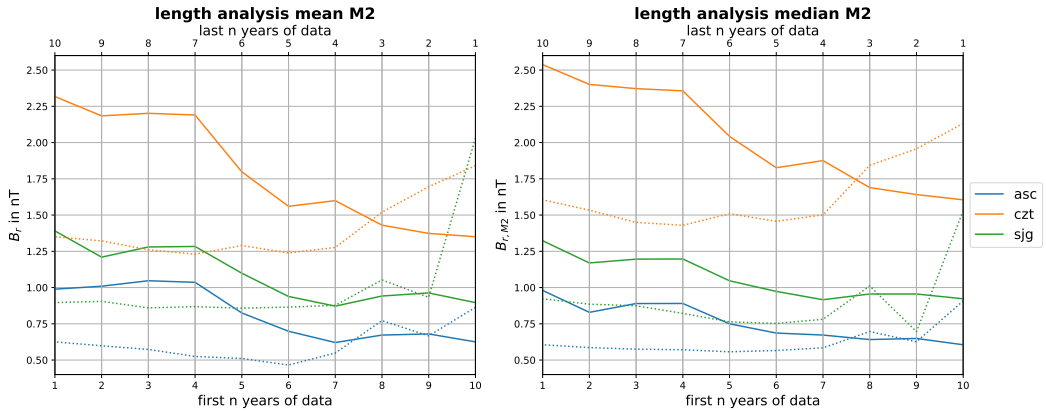

Figure 6.3: Oceanic M2 tide induced magnetic field amplitudes in dependence of analyzed time series length at all three analysed coastal magnetometer stations. The amplitudes were obtained after phasing and averaging the data with the mean (left) and the median (right). Solid lines show the results for the analysis conducted on the first n years of the 10 year time series (corresponding to lower x-axis) while the dotted lines show the analysis results for the last n years of data (corresponding to upper x-axis).

For the analysis of the 10 year time series, we started with time series of 1 year length and increased the length incrementally by 1 year. This was done forward, starting with the first year, and backward, starting with the last. The results of this analysis are shown in figure 6.3. When comparing the results obtained with the mean and median, we find consistent amplitude decrease in both methods for all three observatories. But for the difference in the magnitude of obtained M2 TODS amplitudes, we find a dependency on the selected station. While the difference between mean and meadian derived amplitudes is consistently large at CZT throughout the entire time series($\approx$ 0.25 nT for all time series length), the difference at ASC and SJG decreases with time (from $\approx$ 0.1 nT for time series of up to 5 years to almost 0 for longer time series). When looking into the time series data (not shown), we find an asymmetry in the sinusoidal signal obtained after

averaging with the mean which is not present in the median. Since an offset between median and mean usually indicates a skewed distribution of the given data, we assume that there are either systematic signals in the data which have not been accounted for in the data processing or coastal effects causing a distortion or shift of the sinusoidal signal form. One example for such an effect is the presence of ocean currents causing tidal velocities to shift away from the zero baseline, a phenomenon often found in estuaries.

Focusing on the results of the forward analysis, we find larger amplitudes for short periods and smaller amplitudes for long periods of time thus suggesting a temporal decrease. The results are supported by those obtained from the backward analysis. When comparing the average amplitudes in the first 5-year period (forward analysis) to those of the last one (backward analysis), we find that average amplitudes in the first are indeed larger than those of the last 5-year period. All in all, this validates that there is indeed a perceivable decrease in the amplitudes at the chosen station. However, the large jumps between consecutive years in the first 4 years of the analysis (forward and backward) demonstrate the large uncertainty of the method for short time series. Additionally, please note that phase shifts were not analysed with this method. In principle this is possible by fitting a sinusoidal model to the obtained averaged sinusoidal curves but it would, as we will see, add only little value when evaluating the other methods. The phase is nevertheless important as it is a possible source for the observed amplitude decrease.

6.4.2 *Least Squares*

The second extraction method is fitting a function $F(t)$ to the residual time series data by means of the least squares method. The fit functions $F(t)$ are sums of harmonic functions related to varying tidal constituents. They have the form:

$$F(t) = \sum_n A_n \sin(\omega_n \cdot t) + B_n \cos(\omega_n \cdot t). \tag{6.2}$$

$F(t)$ models the ocean tide induced magnetic field strength at a given time t. The index n indicates the tidal constituent such as S_1, S_2 or M_2. The free parameters A_n and B_n are determined by the least squares fit. From these

coefficients, we compute the TODS amplitude $B_{r,n}$ and also the phase ϕ_n of each tidal mode as:

$$B_{r,n} = \sqrt{A_n^2 + B_n^2} \tag{6.3}$$

$$\phi_n = \arctan 2 \left(\frac{B_n}{A_n} \right) \tag{6.4}$$

.

We fitted eight functions, or *models*, to the time series. The functions can be divided into two groups and details about the exact tidal frequencies in the fitting functions can be found in the supplementary material. The first group focuses on fitting the M2 tide. There, functions include only M2 tides, M2 overtides and their cyclical amplitude variations. The simplest example models the sinusoidal signal of the M2 tide using two parameters; it is similar to the M2 amplitude determination method for coastal island magnetometer obervations of Maus et al. (2004). The most complex model in this group, called "M2_overtides_modulation", includes overtides and their seasonal variation using 240 parameters. Cyclical amplitude modulations are modelled by including side bands of long periodic modulation frequencies f_{mod} corresponding to annual and monthly variations. Mathematically, the side bands can be formulated as:

$$f_{side} = f_{M2} \pm f_{mod}$$

The second group of fitting functions are based on the models used by Schnepf et al. (2014) or by the National Oceanic and Atmospheric Association (NOAA). While the "Schnepf_2014" model includes 15 tidal components, the "NOAA" model includes the 37 constituents which have usually the largest effect on oceanic tides (Parker, 2007; Schureman, 1958). Both models include low frequency tides which should not be present after the data processing. Hence, the second group of models additionally compares the influence of excluding low frequency tides on the amplitude of the M2 tide with models containing the suffix "_short".

The results of the analysis with the simple least squares method are summarized in the figure 6.4. To ease the comparison between the phasing and the least squares method, we included the results of the phasing as black lines.

To investigate the robustness of this method, we first focus on the convergence behaviour of the presented curves with time series length. One finding is that the curves of all measured variables, amplitudes and phases

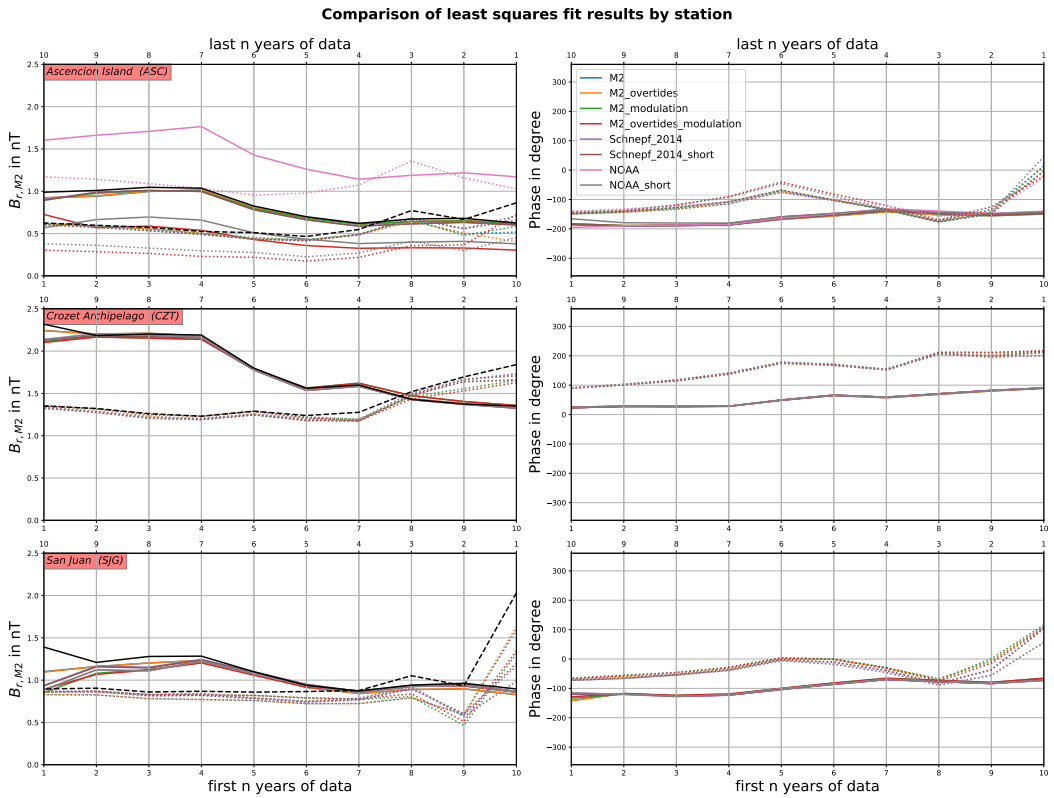

Figure 6.4: Comparison of oceanic M2 tide induced magnetic field signal parameters extracted from the residual data with *least squares fitting* of different harmonic sums. The left column shows the extracted amplitudes and the right column the extracted phases in dependence of analysed time series length. While solid lines show the results for the analysis conducted on the first n years of the 10 year time series (corresponding to lower x-axis), dotted lines show the analysis results for the last n years of data (corresponding to upper x-axis). Black lines in the left column show the results obtained by phasing and averaging the residual data and allows for a comparison of both methods.

alike, converge. Except for the amplitudes identified in the ASC data. The phases are in general very robust and all fit functions seem to converge quite well after 3 years. For the amplitude curves in CZT and SJG, the fit functions seem to converge after 2 and 4 years respectively. 4 years appears to be also the time span after which the difference between the phasing and the least squares method becomes negligible. The dependency of shorter time series on the fitting function is a sign that signals have not been separated sufficiently.

When focusing on the temporal progression of the curves over time, we see that both, amplitudes and phases, demonstrate a clear temporal variability. A finding that is, similar to the analysis in section 6.4.1, supported by the comparison of forward and backward analysis. While changes of the

average amplitudes are in the order of $\mathcal{O}(0.1\ \mathrm{nT})$, changes of the phase are in the order of $\mathcal{O}(10^\circ)$ and reach values of more than 100° in all three observatory time series for the backward analysis. The temporal variation of the M2 phases is not unexpected as its theoretical causes have extensively been studied in Saynisch-Wagner et al. (2020). In all time series, the temporal progression of the amplitudes is very similar to the one found with the first method.

Judging from the spectra after the data processing in section 6.3.1 and the comparison of values obtained after using the mean and the median in section 6.4.1, there is no obvious difference in the quality of the three data series. All the more surprising is that the amplitude curves obtained from the ASC data do not converge. Especially since the phases converge quite fast. We find a cluster of curves delivering values similar to those obtained from method one, but there are also curves that show a consistently large offset in the forward and the backward analysis. These corresponding functions are both "NOAA" functions and the "M2_overtides_modulation" curves. These functions are members of both function categories identified above. Additionally, they deliver reliable results for the observations at CZT and SJG. Furthermore, they are in agreement with the general temporal progression of all curves. Therefore, we can only speculate about residual signals in the data interfering with our analysis. A likely origin for these signals is the ionosphere as we identified signs of ionospheric signals after the detrending methods of first order differencing and magnetic field model subtraction in ASC.

A major shortcoming of the least squares method is its sensitivity to the existence of outliers. The implied assumption of the least squares method is that errors are normally distributed. Thus extreme outliers can occur but are highly unlikely. In time series with few outliers and fully explained signals, the lease squares approach is very efficient. Considering the dissimilarities among the three residual time series fig. 6.1) and the challenge of separating signals using short time series, it is unlikely that a pre-defined fitting function includes the correct frequency characteristic for an arbitrarily chosen magnetometer station. Especially, when taking into account that temporal varying amplitudes and nonlinear effects cause further signal peaks. Pre-defining a fitting function fully explaining the oceanic signal contribution for a single time series is hence a challenging task in itself. If the fit function does not fully explain the signal, it is highly unlikely that unfitted signals in the data can be considered as normally distributed. The

assumptions of the least squares method are consequently violated causing possibly misleading results.

6.4.3 *Robust Least Squares*

On account of the least squares method being overly affected by outliers, its general concept was advanced into an iteratively reweighted least squares (IRLS) (Holland et al., 1977; Huber, 2004). The IRLS is an iterative optimization approach that punishes outliers to reduce their impact on the overall fit. For details on the setup of the algorithm we refer to Schnepf et al. (2014, 2018) as we followed their lead for the implementation of the third extraction method used in this study.

We used the same eight fitting functions as in the ordinary least squares approach. The approach is computationally very expensive, especially when minimizing fit functions with up to 240 parameters with 10 years of average observations for every minute within the time series. As we find the results obtained with the forward analysis sufficiently conclusive, we omitted the backward analysis for this part of the study. The reader will find the summarized results in figure 6.5.

Comparing figure 6.5 and figure 6.4, we observe the same qualitative temporal behaviour of mean amplitudes and phases. We also find that phase values are in general more robust than amplitude values. However, apart from the similarities, we find a considerable deviation in the convergence behavior of both amplitudes and phases. While differences between phases were in the order of $\mathcal{O}(5^\circ)$ in all stations when analysing time series longer than four years with the ordinary least squares approach, there is no apparent generalized behaviour when using the IRLS for the analysis. While at CZT the phase values converge almost immediately and deviate by a few degrees, at ASC we have an almost constant spread of $\approx 20^\circ$. At SJG the individual phase curves form a group with a total spread of $\approx 30^\circ$. For the amplitudes, we also find a larger spread. While the spread at ASC stays large with a value of ≈ 1 nT, the spread at CZT converges after ≈ 4 years to a group of curves with a spread of ≈ 0.1 nT. For SJG, we find that amplitudes conserve an almost constant spread of ≈ 0.2 nT. All in all, we find it plausible that there seems to be a correlation between amplitude M2 signal strength (largest at CZT) and the observed spread in amplitude and phase as large signals are generally easier to identify. In section 6.4.1, we have seen that the difference between results obtained with the median

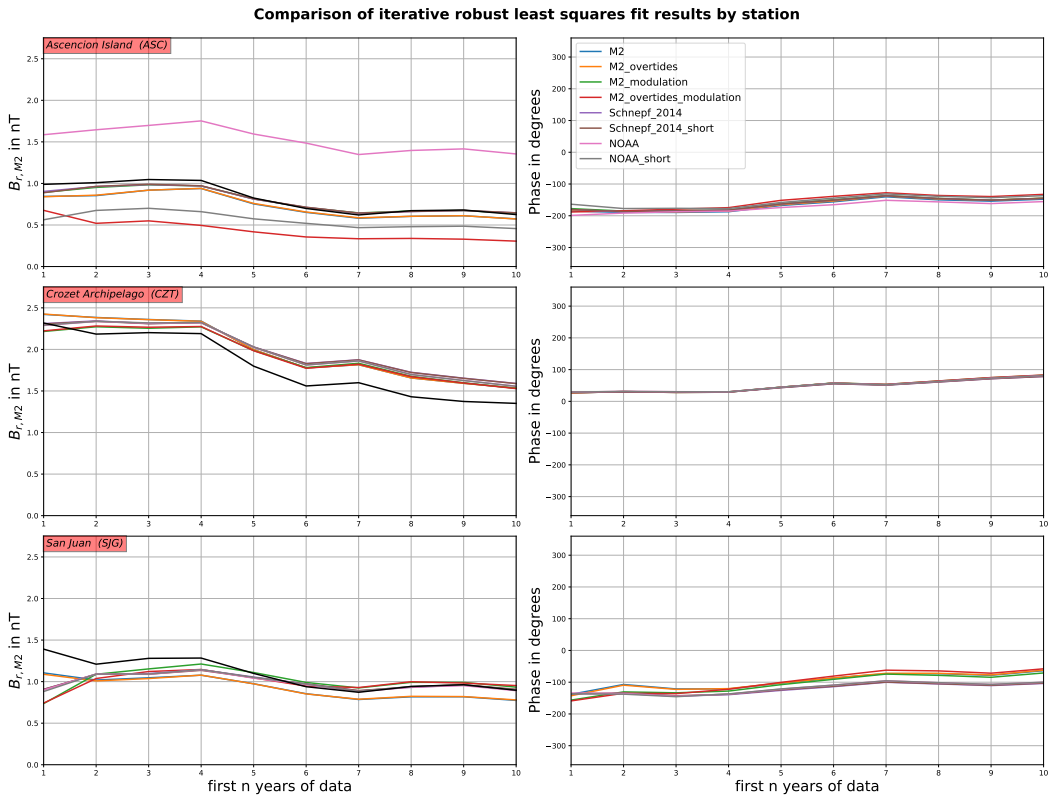

Figure 6.5: Comparison of oceanic M2 tide induced magnetic field signal parameters extracted from the residual data by fitting different harmonic sums using an *iterative robust least squares* approach. The left column shows the extracted amplitudes and the right column the extracted phases in dependence of analysed time series length. In contrast to the previous figures, only the analysis of the first n years of the 10 year time series are presented because of the computational costs of this analysis and the evident conclusions that can be drawn from these presented results. Black lines in the left column show the results obtained by phasing and averaging the residual data and allows for a comparison of both methods.

and the mean already indicated a systematic influence of non M2 tidal data. In view of these results, we also find it not surprising that the amplitude curves obtained from the CZT data converge to a curve with a substantial offset from the curve obtained by using the mean after phasing the data.

A possible reason for the noticable divergence of the results obtained from the analysis of the ASC data in comparison to the data of the other observatories is the location. In contrast to CZT and SJG, ASC is co-located with the South Atlantic Anomaly. Consequently, the influence of the secular variation is noticeable at a higher frequency together with an increased magnitude. Furthermore, the lower values of the core magnetic field lead to a reduced shielding effect causing an increase in the influence of external

sources on the overall signal. Hence, the difference in the analyses results is possibly originating from the location of the observatories with respect to the core field morphology.

We conclude that using the IRLS helps to asses the uncertainty in the amplitudes obtained with other less cost-expensive methods. Additionally, it confirmed the robustness of the obtained average phases and their temporal development. But, the interdisciplinary nature of identifying oceanic signals in magnetometer observations requires an indisputable amount of expert knowledge when choosing a fit function and parameters for the IRLS algorithm and interpreting the obtained results as well as evaluating the plausibility. The fact that the curves of SJG are seemingly separated into two groups for both, amplitudes and phases, is a good example that the optimization in the background of the algorithm may not be able to identify a global minimum on a flat curve with several local minima.

At this point, we want to draw the attention to some of the limitations of the existing study. Average amplitudes and phases obtained by the used methods differ substantially from M_2 TODS amplitudes for the following reasons. Variations and trends in the actual amplitudes are averaged in the extraction methods over the whole time span. At this point in time it is unknown whether the average amplitude changes are caused by either trends, phase changes, interannual variation in the seasonal variability or a combination of each. The extracted amplitudes are only an approximation to the actual amplitude. Furthermore, none of the presented extraction methods includes trends in phases or amplitudes explicitly as they have not been a priori known.

6.5 CONCLUSIONS

Ocean tide induced magnetic field signals are an integral measure of seawater temperature and salinity, tidal transports and the geomagnetic field strength. The signals are thus a valuable asset in the attempt of closing the observation gap in the ocean. Alas, in coastal regions, there is a noticeable offset between observed and modeled ocean tide induced magnetic field amplitudes (Maus et al., 2004; Schnepf et al., 2018). A possible explanation is that the radial magnetic field in coastal proximity is largely influenced by the surrounding 3-D conductivity structure (Dostal et al., 2012; Schnepf et al., 2015). The conductivity structure results from the bathymetry which defines the amount of conductive seawater and mire. Another explanation

for this mismatch which is further investigated in this study are temporal amplitude and phase variations in the tidal EM signals. Model studies (Petereit et al., 2019; Saynisch-Wagner et al., 2020) revealed that seasonal phenomena such as thermocline displacements cause considerable variations in both signal amplitudes and phases.

In this study, we made a first attempt to identify the temporal variations in 10 years of minute magnetometer data of three island magnetometer observatories. We first evaluated the quality of different data processing approaches with a spectral method capable of analysing the unevenly sampled data obtained after the processing. We find that existing approaches, namely subtracting geomagnetic core field models like, in our case, CHAOS or applying first order differencing, a method used in time series analysis, show deficiencies. After presenting and evaluating a suitable data processing technique, we used the data to assess seasonal variations and long-term trends using two different approaches. For the seasonal variations, we assessed the signal strength of M2 signal peak sidebands in the spectral data. We find indications for seasonal variations ranging, depending on the measuring site, from $\approx 10\%$ to $\approx 25\%$ of the M2 signal strength. For the long-term trends, we used three approaches to identify mean amplitudes and phases in time series data. The approaches were applied to time series of incrementally increasing lengths (increment = one year), starting with a time series length of one year. We find that with increasing lengths mean amplitudes change by up to ≈ 1 nT. These changes, however, cannot be attributed solely to amplitude variations of the M2 signal but also to phase changes and measuring uncertainties. Based on our results, we find that when applying the presented methods more than 4 years of observations are necessary to obtain reliable results. An identification of seasonal variations has hence not been achieved. Additionally, we find that signal phases do not only show temporal variations in the order of $\mathcal{O}(10^\circ)$ but also appear to be a more robust measurand than signal amplitudes.

Advances in this field are not only relevant for ocean observations but have also applications in magnetotelluric studies as they can be used for sounding the conductivity distribution of the mantle. Ocean tide induced magnetic field signals are sensitive to the conductivity distribution of subsurface layers (Chave, 1983; Dostal et al., 2012; Schnepf et al., 2015). This allowed for a successful global inversion to obtain an improved 1-D mantle conductivity distribution (Grayver et al., 2016). All the more important is

to realize a comprehensive understanding of the temporal development of ocean tide induced magnetic field signals, especially in coastal proximity.

One future measure is to advance the modelling capacities to small scale processes on the coastal shelves. When combining advancements in electromagnetic field modelling (Kruglyakov et al., 2020) and ocean modelling (Sulzbach et al., 2021), improved results are to be expected. Additionally, this would also help to shed light onto the role of the long-range effect of electromagnetic fields in the observed magnetic field amplitudes. Already in 1920, tidal ocean-dynamo signals were measured that did not match the tidal flow at the measurement site, but with stronger flow at a distant location generating stronger signals (Young et al., 1920). Identifying the exact location of the electric source causing the observed magnetic fields or the composition of sources adding to the signal will help to bridge the gap between EM signal observation and ocean observation. This is especially important as the remote sensing advantage does not apply to small scale EM signals. They decay faster than large scale signals with the distance so that at satellite altitude only the large scale pattern of the global tides remain. This is also one of the reasons why Tsunamis are unlikely to be detected at satellite altitude despite the fact that their signal strength is comparable with those of ocean tide induced magnetic field signals at sea level (Kuvshinov, 2008). And last but not least, the challenge of identifying seasonal M2 signal variations in coastal island magnetometer observations remains

Part III

Learning and Reasoning

7

CLOSING REMARKS

Chapter Summary

Two sections form this final chapter of the present thesis. The first summarizes the previous chapters and highlights important research findings; the second provides an outlook on future research on the road to achieving a signal-based tidal ocean-dynamo ocean observation.

7.1 THESIS SUMMARY

The achieved level of comprehension about magnetic fields induced by tidal ocean currents results in a good agreement between satellite measured and modeled global signal amplitudes distributions. To realize the vision of observing transports of oceanic heat and salinity using magnetic field signals, a broad understanding of how oceanic salt and temperature changes vary tide-induced magnetic field amplitudes is needed. The present thesis investigates this relationship on sub-decadal time scales. In particular, the magnitude and spatial distribution of expected amplitude variations are investigated which enable an assessment of the circumstances under which oceanic processes lead to measurable and detectable signal changes.

ENSO RELATED SIGNAL VARIATIONS The El Niño/Southern Oscillation (ENSO) plays a dominant role in global interannual climate variability. It causes large-scale anomalies in seawater temperature and salinity distributions so that the phenomenon is well suited for a case study to characterize the relation of temporal tidal ocean-dynamo signal variations and ocean dynamics. Fifty years of oceanic seawater temperature and salinity distributions are modeled using a coupled ocean-atmosphere model. The data is then used to calculate the electric current induced by the oceanic tides. Subsequently, electromagnetic signals induced by the electric current's interplay with the electrical conducting surrounding is computed using a numerical solver for the electromagnetic induction equation. From the analysis of the combined set of oceanic and electromagnetic signal data,

it is inferred that the changes in the electromagnetic signals are statistically preceding the well-known changes in sea surface temperatures associated with ENSO. The EM signal changes at the sea surface are above the accuracy threshold of cutting edge magnetometers but well below the threshold of magnetometers commonly used for space-borne, land-based or ocean-bottom observations. The investigation of the oceanic causes of the lead of the electromagnetic signals revealed that subsurface processes, i.e., thermocline dynamics, precede the onset of cold and warm ENSO phases. These are responsible for the found lead, a finding with direct implications for the impact of internal waves on tidal ocean dynamo signal amplitudes.

GLOBAL SPATIO-TEMPORAL VARIATION PATTERNS The first study demonstrated that in addition to the magnitude of oceanic temperature and salinity anomalies, the location of their occurrence plays a vital role in the resulting magnitude of ocean tide-induced signal variations. Therefore the second study examines the factors determining meaningful changes in the tidal ocean-dynamo signals. The second study uses the experimental setup of the first study but replaces the modeled ocean data with a time series of global seawater temperature and salinity arrays, a data product obtained through reanalysed in-situ measurements. This setup allows estimating tidal ocean-dynamo signal variations that have occurred during the period from 1990-2015 in conjunction with the driving factors and preconditions for these changes. The study showed that, in the first order, a linear relation between changes in the depth-averaged seawater conductivity and resulting tidal ocean dynamo signal variations are in the vast majority of cases caused by changes in the seawater temperature distribution. On the one hand, the analysis of the temporal TODS development provided insight into seemingly contradicting findings in the literature. On the other, it separated the effect of seasonal influences and climate trends in the found anomalies. It was demonstrated that there is a significant difference between TODS sensitivity in the open sea and the continental shelves. While seasonal variations in the more sensitive shelf regions lead locally to TODS amplitude anomalies in the order of $\mathcal{O}(10^{-1}\ \mathrm{nT})$, the effect of comparable changes in seawater temperature in the open ocean is negligible. On decadal time scales, even climate trends induced signal amplitude variations become measurable in continental shelf regions.

OBSERVATIONS OF SIGNAL VARIATIONS After having modeled and analyzed temporal TODS variations extensively, it requires experimental validation to secure the gained insights. The second study provided knowledge of the characteristics of signal variability needed for identifying these signal variations in the concoction of magnetic field signals contributing to raw magnetometer observations. It further provides the location of promising measuring sites so that the identification of temporal signal developments in magnetometer observations is rendered possible. In the third and final study presented in this thesis, existing time series of 10 years of minute observation data from three island magnetometer observatories are analyzed. After developing and validating a novel data processing procedure, the study presents evidence for seasonal variations and long-term trends in TODS amplitudes. Additionally, when comparing findings of amplitudes and phases, the study finds signs for superior robustness and confidence in the retrieved phase information than in the amplitudes. Furthermore, when comparing commonly used extraction methods, the study finds that at least four years of data are needed to obtain a reliable value for the M2 TODS amplitude.

In a nutshell, the combination of findings presented in this thesis leads to the first observation of temporal variations of TODS amplitudes and phases and unprecedented insights into the relationship between ocean dynamics and TODS variations.

7.2 STANDING CHALLENGES AND OUTLOOK

The steps made towards a mature ocean observation technology based on ocean tide-induced magnetic field signals are just a start. In order to realize this goal one day, advances in the field of *TODS Modelling*, *Signal Characterization* and *Magnetic field Data analysis* are needed to achieve the goal of fully explained ocean tide induced magnetic field signals.

TODS MODELLING At coastal regions, one finds a persistent offset between modeled and observed TODS. To resolve this offset, advances are needed in the field of ocean modelling in terms of increased resolution and modelling of non-linear phenomena, whose influence is most significant in coastal proximity, correctly (Sulzbach et al., 2021). Additionally, improved numerical induction solvers are now available (Kruglyakov et

al., 2020) which have been found not only to be more accurate but also to compute more efficiently than existing solvers. These developments will therefore allow the modeling of small-scale structures in the TODS amplitude distribution with an unprecedented resolution in the future. In the past the significant role of the resolution in modelling TODS in the open ocean has already been established by Schnepf et al. (2014) which becomes all the more important in coastal proximity.

SIGNAL CHARACTERIZATION Virtually all existing studies aimed at the observation of ocean transports of heat and salinity using TODS eliminated the influence of the secular variation of Earth's magnetic field in their studies. This simplification is commonly justified with the argument that changes in Earths magnetic field are negligible on the investigated timescales. The only exception to this is the study of Saynisch-Wagner et al. (2020). When analyzing the amplitudes of the 25-year data set used in their study (c.f. figure 7.1), we find that the influence of temporal variations of Earth's magnetic field becomes meaningful on decadal time scales. When comparing these M2 TODS amplitude anomalies combining secular variation and seawater temperature and salinity with those of the second study which eliminated the influence of the secular variation, anomalies are no longer predominantly found in shallow shelf regions but distributed throughout all ocean regions.

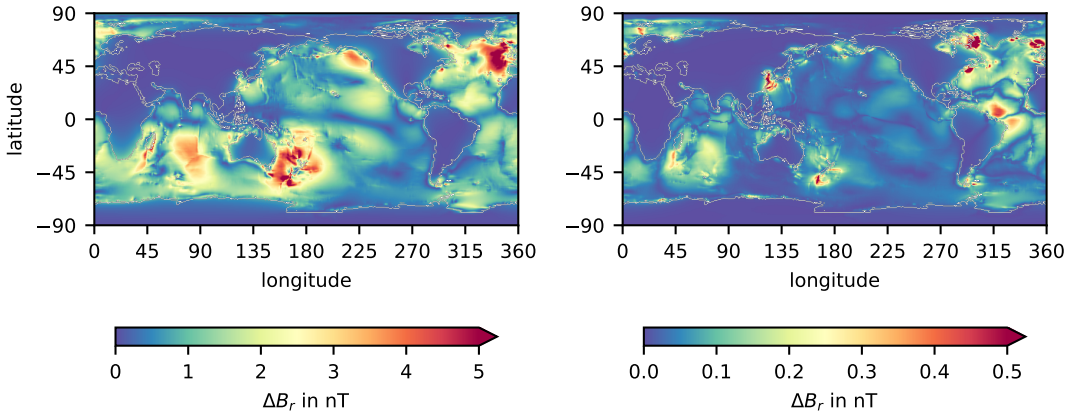

Figure 7.1: Maps of modeled principal lunar tidal (M2) ocean dynamo signals generated. The left image shows the mean amplitude at each location computed from modeled 25 years of monthly time slices. In the model oceanic seawater temperature and salinity as well as Earth's magnetic field are time variable. The right image depicts the peak-to-peak difference at each location during the analysed period.

To separate the effect of oceanic causes from those imposed by the secular variation of Earth's magnetic field, the time series has been recomputed with two different setups. While in the first setup, the time series of ocean conductivity distributions was replaced with a time-constant mean input value, the second setup did the same for Earth's magnetic field. The results of the differing impacts on M2 TODS amplitudes are shown in figure 7.2.

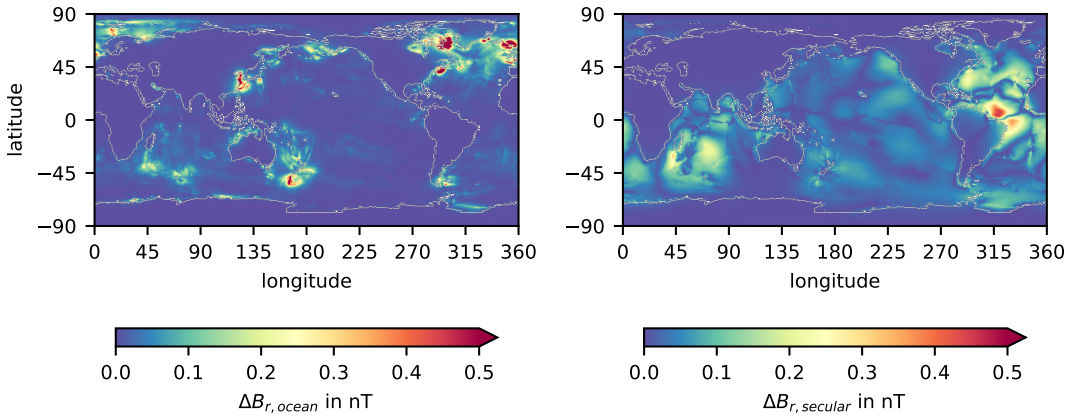

Figure 7.2: Maps of modeled M2 TODS anomalies. The left map shows the anomalies attributed to oceanic causes and the right map shows anomalies caused by temporal changes in Earth's magnetic field during the analysed 25 year period.

Following the findings of this experiment, it becomes apparent that it is not sufficient to measure M2 TODS variations to observe oceanic temperature and salinity transports. The impact of all influencing factors needs to be separated to make correct assumptions about the oceanic causes for the amplitude variation.

Another promising field for advances in the field is the research in the field of TODS phase dynamics. Investigations on TODS phase changes are an emerging field whose foundation is provided by the result of higher reliability in observed TODS phases (c.f. 6) in combination with the knowledge of the underlying mechanism (Saynisch-Wagner et al., 2020). Based on these prerequisites new studies can be designed whose insights are much needed for a comprehensive understanding of TODS leading ultimately to a fully explained tidal ocean dynamo signal.

MAGNETIC FIELD DATA ANALYSIS The third study provides evidence for M2 TODS variations on sub-annual to decadal time scales. The findings, however, represent only a next step into this area of research. Using algorithms described in this study, the approach can easily be adapted and extended to additional observatories. Using moving 4-year time slices, the

approach allows for the generation of a time series of relatively reliable M2 TODS amplitudes. The analysis of said time series in the context of existing ocean observations and model predictions can in principle advance the observational capabilities using TODS. However, the study also showed that the approach is not easily automated, demanding in computational resources and time, and is ultimately limited to a temporal resolution of approximately four years. Hence, efforts to advance existing extraction capability will pay dividends for future applications. For doing so, expertise about electromagnetic field signals in all spheres and time scales needs to be joined and combined with state of the art time series analysis methods to separate all signals from raw magnetometer observations. This includes extending the tidal analysis to all partial tides instead of focusing on the principal lunar tides. The complete set of partial tides provides additional knowledge of the temporal development of TODS amplitudes. Also, a complete description of all partial tidal components and their relative magnitude provides insights into the underlying processes as a source of the signals, i.e. ocean tides, is well understood. Likewise, investigating the impact of seawater temperature and salinity changes on TODS on multiple tidal frequencies should lead to more robust conclusions about temporal TODS variations, as the impact should be the same on all frequencies.

All in all, research on temporal TODS variations is tied to multiple fields and poses many new challenges. Its findings will also be directly applicable to research fields relying on processed magnetic field observations. A precise description of ocean tide-induced magnetic fields improves also the data cleaning process. The field of magnetotellurics, for example, will benefit as new insights into the distribution of subsurface conductivity distributions can be achieved. On top of these, however, crowns the objective of realizing a novel ocean observation technique for oceanic temperature and salinity transports. Whether this goal will be achievable depends on the fact whether the presented challenges can be solved or not. However, the present thesis and its combined research findings achieved an essential step towards this ambitious goal.

Part IV

Appendix

a

SUPPLEMENTARY MATERIAL: ON TEMPORAL VARIATIONS OF COASTAL TIDAL OCEAN-DYNAMO SIGNALS

SHORT INFO

Here we provide additional but more specifically more technical information. This includes a mathematical explanation of the amplitude modulation as well as tables that provide additional details on the used methods and figures used to support our argumentation.

Amplitude Modulation

In the following, we describe the amplitude modulation model we used. A sinusoidal signal, in our specific case the M_2 tidal constituent (or higher order of it), is identified as the carrier wave $c(t)$:

$$c(t) = A \sin(\omega_{M_2} t). \tag{a.1}$$

The carrier wave $c(t)$ is modulated by a the message signal $m(t)$ with the modulation frequency ω_m.

$$m(t) = m \cos(\omega_m t). \tag{a.2}$$

The modulated signal can thus be described as:

$$y(t) = [1 + m(t)]\, c(t) = [1 + m \cos(\omega_m t)]\, A \sin(\omega_{M_2} t), \tag{a.3}$$

where m is the modulation index which indicates the modulation of the carrier wave amplitude in percent. Using the trigonometric identities we can describe the modulated signal $y(t)$ as:

$$y(t) = A \sin(\omega_{M_2} t) + \frac{1}{2} Am \left[\sin\left(\left(\omega_{M_2} + \omega_m\right) t\right) + \sin\left(\left(\omega_{M_2} - \omega_m\right) t\right)\right]. \tag{a.4}$$

The modulated signal has consequently three components, the unchanged carrier signal $c(t)$ and two sidebands. Please note, ω_m is usually much lower than the carrier frequency. The sideband frequency are below ($f = \omega_{M_2} - \omega_m$) and above ($f = \omega_{M_2} + \omega_m$) the carrier frequency, with the frequency difference of the message signal. Since the mentioned effects acting on the M_2 signal occur seasonally, we chose the seasonal frequencies for the message signal (c.f. table A.3).

Descriptions and Details of the Presented Fit Functions

Table a.1: Names, Identifiers and short description of harmonic models with focus on amplitude modulation

Identifier	Name (hsum_)	# of Tidal Frequencies	Description
1	M_2	1	Harmonic sum comprising only the oscillation of the M_2, comparable to Maus et al., 2004
2	M_2_overtides	8	Harmonic sum comprising all tidal harmonics of the lunar tide ranging from M_1 to M_8
3	M_2_modulation	15	Harmonic sum modelling the amplitude variation of the carrier frequency of the M_2 long periodic modulation frequencies
4	M_2_overtides_modulation	120	Harmonic sum modelling the amplitude variation of the a non-sinusoidal carrier signal comprising the M_2 tide and higher harmonics (see hsum_M_2_overtides) modulated on long period

The focus of models 1-4 is to analyse the TODS of the M_2 tide, its deviation from the sinusoidal signal and its amplitude modulation.

Table a.2: Names, Identifiers and short description of harmonic models with focus on the influence of superposing oscillations

Identifier	Name (hsum_)	# of Tidal Frequencies	Description
5	Schnepf_2014	15	Harmonic sum used in the analysis of coastal TODS of Schnepf et al., 2014
6	Schnepf_2014_short	12	Harmonic sum similar to the Schnepf_2014 model except that it does not include low frequency models. It is closely related to the model of Schnepf et al., 2018 but unlike their model our model assures consistency and comparability by including the O_1 and P_1 components like in the publication of Schnepf et al., 2014
7	NOAA	37	Harmonic sum comprising the 37 tidal constituents of the NOAA model
8	NOAA_short	32	hsum_NOAA without low frequency components

For the models 5-8, the focus is analysing the influence of incorporating additional oscillations on the extracted TODS amplitude of the M_2 tide

Tidal Component used in this study

Table a.3: Long periodic tidal constituents

Species	Darwin Symbol	Period (hr)	Speed ($^\circ/hr$)	Model used
Nodal Modulation	Om_1	163161.711385	0.0022064	5
Solar annual	S_a	8766.15265	0.0410686	3*, 4*, 5, 7
Solar semiannual	S_{sa}	4383.076325	0.0821373	3*, 4*, 5, 7
Solar terannual	S_{ta}	2921.98542416	0.1232039	3*, 4*
Lunar synodic monthly	MS_m	763.486512056	0.4715211	3*, 4*
Lunar monthly	M_m	661.3111655	0.5443747	3*, 4*, 7
Lunisolar synodic fortnightly	MS_f	354.3670666	1.0158958	3*, 4*, 7
Lunisolar fortnightly	M_f	327.8599387	1.0980331	3*, 4*, 7

* in these models the frequencies are included only indirectly as sidebands to the either the M_2 tide alone (model 3) or the M_2 tide and its overtides (model 4).

Table a.4: Diurnal tidal constituents

Species	Darwin Symbol	Period (hr)	Speed ($^\circ/hr$)	Model used
Larger elliptic diurnal	$2Q_1$	28.00621204	12.854286	7, 8
Larger lunar elliptic diurnal	Q_1	26.868350	13.39866	7, 8
Larger lunar evectional diurnal	ϱ	26.72305326	13.471514	7, 8
Lunar diurnal	O_1	25.81933871	13.9430356	5, 6, 7, 8
Smaller lunar elliptic diurnal	M_1	24.84120241	14.4920521	2, 7, 8
Solar diurnal	P_1	24.06588766	14.9589314	5, 6, 7, 8
Solar diurnal	S_1	24	15	5, 6, 7, 8
Lunar diurnal	K_1	23.93447213	15.0410686	5, 6, 7, 8
Smaller lunar elliptic diurnal	J_1	23.09848146	15.58544	7, 8
Lunar diurnal	OO_1	22.30608083	16.139101	7, 8

Table a.5: Semidiurnal tidal constituents

Species	Darwin Symbol	Period (hr)	Speed ($^\circ/hr$)	Model used
Lunar elliptical semidiurnal second-order	$2''N_2$	12.90537297	27.8953548	7, 8
Variational	μ_2	12.8717576	27.968208	7, 8
Larger lunar elliptic semidiurnal	N_2	12.65834751	28.4397295	5, 6, 7, 8
Larger lunar evectional	ν_2	12.62600509	28.5125831	7, 8
Principal lunar semidiurnal	M_2	12.4206012	28.9841042	all models
Smaller lunar evectional	λ_2	12.22177348	29.4556253	7, 8
Smaller lunar elliptic semidiurnal	L_2	12.19162085	29.5284789	7, 8
Larger solar elliptic	T_2	12.01644934	29.9589333	7, 8
Principal solar semidiurnal	S_2	12	30	5, 6, 7, 8
Smaller solar elliptic	R_2	11.98359564	30.0410667	7, 8
Lunisolar semidiurnal	K_2	11.96723606	30.0821373	5, 6, 7, 8
Shallow water semidiurnal	$2SM_2$	11.60695157	31.0158958	7, 8

Table a.6: Short periodic tidal constituents

Species	Darwin Symbol	Period (*hr*)	Speed ($^\circ/hr$)	Model used
Shallow water terdiurnal	2"MK_3	8.38630265	42.927139	7, 8
Lunar terdiurnal	M_3	8.280400802	43.4761563	2, 4, 7, 8
Shallow water terdiurnal	MK_3	8.177140247	44.025172	7, 8
Shallow water overtides of principal solar	S_3	8	45	5, 6
Shallow water quarter diurnal	MN_4	6.269173724	57.423833	7, 8
Shallow water overtides of principal lunar	M_4	6.210300601	57.9682084	2, 4, 7, 8
Shallow water quarter diurnal	MS_4	6.103339275	58.984104	7, 8
Shallow water overtides of principal solar	S_4	6	60	5, 6, 7, 8
Shallow water overtides of principal lunar	M_5	4.96824048818	72.4602605	2, 4
Shallow water overtides of principal solar	S_5	4.8	75	5, 6
Shallow water overtides of principal lunar	M_6	4.140200401	86.9523127	2, 4, 7, 8
Shallow water overtides of principal solar	S_6	4	90	5, 6, 7, 8
Shallow water overtides of principal lunar	M_7	3.54874320584	101.4443647	2, 4
Shallow water eighth diurnal	M_8	3.105150301	115.9364166	2, 4, 7, 8

Part V

Backmatter

LIST OF FIGURES

NOMENCLATURE

ABBREVIATIONS

ACC	Antarctic Circumpolar Current
AMOC	Atlantic Meridional Overturning Circulation
ASC	IAGA Code for Ascencion Island
ARGO	Worldwide fleet of drifting ocean profiling floats
CHAMP	CHAllenging Minisatellite Payload
CHAOS	a model of the Earth's magnetic field
CM	Comprehensive magnetic field model
CMEMS	Copernicus Marine Environment Monitoring Service
CMIP	Coupled model intercomparison project
CORA	Coriolis data set for Re-Analysis
CPC	Climate Prediction Center
CZT	IAGA Code for Crozet Archipelago
ECHAM	Atmospheric general circulation model
ECMWF	European Centre for Medium-Range Weather Forecasts
EEJ	Equatorial Electrojet
EM	Electromagnetic
EM-APEX	Electromagnetic Autonomous Profiling Explorer
EMOTS	electromagnetic oceanic tidal signals cf. TODS
ENSO	El Niño/Southern Oscillation
FFT	Fast Fourier Transform
GMT	Global mean Temperature
GRACE	Gravity Recovery And Climate Experiment
GRIMM	GFZ Reference Internal Magnetic Model
IAGA	International Association of Geomagnetism and Aeronomy

IGRF	International Geomagnetic Reference Field
IPCC	Intergovernmental Panel on Climate Change
IRLS	Iteratively reweighted least squares
ISAS	In-situ analysis system
MaNi	Magnetic Niño Index
MPIOM	Max-Planck-Institute Ocean Model
NOAA	National Oceanic and Atmospheric Administration
OGCM	Ocean General Circulation Model
OHC	Ocean heat content
OMCT	Ocean Model for Circulation and Tides
ONI	Oceanic Niño Index
Ørsted	Danish geomagnetic field satellite mission
PIRATA	Prediction and Research Moored Array in the Atlantic
RAMA	Research Moored Array for African-Asian-Australian Monsoon Analysis and Prediction
SAC-C	Scientific Application Satellite-C
SJG	IAGA code for San Juan
SSH	Sea surface height
SST	Sea surface temperature
SQ	Solar Quiet Variation
Swarm	ESA geomagnetic field satellite mission
TAO	Tropical Atmosphere Ocean project
TEOS-10	The International thermodynamic equation of seawater–2010
TODS	Tidal ocean-dynamo signal
TOPEX/Poseidon	Ocean Surface Topography from Space
TPXO	TOPEX/Poseidon global tidal model
TRITON	Triangle Trans-Ocean Buoy Network
TSA	Time series analysis
WOA	World Ocean Atlas
x3dg	3-D induction solver

$\vec{\nabla}$	Nabla-Operator
$\vec{\nabla}\vec{f}$	Gradient of $\vec{f}$
$\vec{\nabla}\cdot\vec{f}$	Divergence of $\vec{f}$
$\vec{\nabla}\times\vec{f}$	Rotation of $\vec{f}$
$\frac{\partial\vec{A}}{\partial a}$	Partical derivative of A with respect to a
$\propto$	Proportional to
$\|\|a\|\|$	Absolute value of a
$\vec{B}$	Magnetic field
$\vec{B}_r$	Radial component of ocean-dynamo induced magnetic field
Δ	Delta: Indicating a difference
$\vec{E}$	Electrical field
ϵ_0	Permittivity of the free space
$F(t)$	(Fit) function of t
f	Frequency
$\vec{F}_{\mathrm{E}}$	Electric force (part of the Lorentz force)
$\vec{F}_{\mathrm{Lorentz}}$	Lorentz Force
$\vec{F}_{\mathrm{m}}$	Magnetic force (part of the Lorentz force)
g	Gravitational Acceleration
h	Ocean depth
$\vec{j}$	Electric current density
μ_0	Permeability of the free space
N	Total number of elements
$\mathcal{O}(\ )$	Order of magnitude
ω	Angular frequency
p	Pressure
P	Pressure
ϕ	Phase
φ	Longitudinal coordinate

R^2	Coefficient of determination
r	Distance
R_E	Earth Radius
ρ	Electric charge density
S	Seawater salinity
s	Smoothing parameter
$spl(x)$	Value of a given spline at coordinate x
Σx_i	Sum of all x while individual x are identified with index i
σ	Electrical (seawater) conductivity
σ_{mean}	Depth-averaged electrical seawater conductivity
T	Seawater temperature *or* Period
T_{int}	Depth-integrated seawater temperature
t	Time
θ	Latitudinal coordinate
q	Electrical charge
$\vec{v}$	Velocity vector
$\vec{V}$	Depth-integrated and conductivity weighted velocity

BIBLIOGRAPHY

Abraham, J. P., M. Baringer, N. L. Bindoff, T. Boyer, L. J. Cheng, J. A. Church, J. L. Conroy, C. M. Domingues, J. T. Fasullo, J. Gilson, G. Goni, S. A. Good, J. M. Gorman, V. Gouretski, M. Ishii, G. C. Johnson, S. Kizu, J. M. Lyman, A. M. Macdonald, W. J. Minkowycz, S. E. Moffitt, M. D. Palmer, A. R. Piola, F. Reseghetti, K. Schuckmann, K. E. Trenberth, I. Velicogna, and J. K. Willis (2013). "A review of global ocean temperature observations: Implications for ocean heat content estimates and climate change." In: *Reviews of Geophysics* 51.3, pp. 450–483. DOI: https://doi.org/10.1002/rog.20022.

Adams, A. J. S. (1881). "Earth currents. Part 2." In: *Journal of the Society of Telegraph Engineers and of Electricians* 10.35, pp. 34–44.

Alken, Patrick, Erwan Thébault, Ciarán D Beggan, H Amit, J Aubert, J Baerenzung, TN Bondar, WJ Brown, S Califf, A Chambodut, A. Chulliat, G. A. Cox, C. C. Finlay, A. Fournier, N. Gillet, A. Grayver, M. D. Hammer, M. Holschneider, L. Huder, G. Hulot, T. Jager, C. Kloss, M. Korte, W. Kuang, A. Kuvshinov, B. Langlais, J.-M. Léger, V. Lesur, P. W. Livermore, F. J. Lowes, S. Macmillan, W. Magnes, M. Mandea, S. Marsal, J. Matzka, M. C. Metman, T. Minami, A. Morschhauser, J. E. Mound, M. Nair, S. Nakano, N. Olsen, F. J. Pavón-Carrasco, V. G. Petrov, G. Ropp, M. Rother, T. J. Sabaka, S. Sanchez, D. Saturnino, N. R. Schnepf, X. Shen, C. Stolle, A. Tangborn, L. Tøffner-Clausen, H. Toh, J. M. Torta, J. Varner, F. Vervelidou, P. Vigneron, I. Wardinski, J. Wicht, A. Woods, Y. Yang, Z. Zeren, and B. Zhou (2021). "International geomagnetic reference field: the thirteenth generation." In: *Earth, Planets and Space* 73.1, pp. 1–25. DOI: 10.1186/s40623-020-01288-x.

Andres, M., T. B. Sanford, L. R. Centurioni, and J. W. Book (2015). "Mean Structure and Variability of the Kuroshio from Northeastern Taiwan to Southwestern Japan." In: *Oceanography* 28, pp. 84–95. DOI: 10.5670/oceanog.2015.84.

Apel, J. R. (1987). *Principles of ocean physics*. Academic Press.

Ba, Jin, Noel S Keenlyside, Mojib Latif, Wonsun Park, Hui Ding, Katja Lohmann, Juliette Mignot, Matthew Menary, Odd Helge Otterå, Bert Wouters, et al. (2014). "A multi-model comparison of Atlantic multidecadal variability." In: *Climate dynamics* 43.9-10, pp. 2333–2348.

Baringer, Molly O'Neil and J. C. Larsen (2010). "Sixteen years of Florida Current Transport at 27° N." In: *Geophysical Research Letters* 28.16, pp. 3179–3182. DOI: 10.1029/2001GL013246.

Baerenzung, Julien, Matthias Holschneider, Johannes Wicht, Vincent Lesur, and Sabrina Sanchez (2020). "The Kalmag model as a candidate for IGRF-13." In: *Earth, Planets and Space* 72.1, pp. 1–13.

Bamston, Anthony G., Muthuvel Chelliah, and Stanley B. Goldenberg (1997). "Documentation of a highly ENSO related SST region in the equatorial Pacific: Research note." In: *Atmosphere-Ocean* 35.3, pp. 367–383.

Bindoff, N. L., F. E. M. Lilley, and J. H. Filloux (1988). "A Separation of Ionospheric and Oceanic Tidal Components in Magnetic Fluctuation Data." In: *Journal of geomagnetism and geoelectricity* 40.12, pp. 1445–1467. DOI: 10.5636/jgg.40.1445.

Blackman, R. B. and J. W. Tukey (1958a). "The Measurement of Power Spectra from the Point of View of Communications Engineering — Part I." In: *Bell System Technical Journal* 37.1, pp. 185–282. DOI: https://doi.org/10.1002/j.1538-7305.1958.tb03874.x.

— (Mar. 1958b). "The measurement of power spectra from the point of view of communications engineering — Part II." In: *The Bell System Technical Journal* 37.2, pp. 485–569. DOI: 10.1002/j.1538-7305.1958.tb01530.x.

Bretherton, Francis P, Russ E Davis, and CB Fandry (1976). "A technique for objective analysis and design of oceanographic experiments applied to MODE-73." In: *Deep Sea Research and Oceanographic Abstracts*. Vol. 23. 7. Elsevier, pp. 559–582.

Broun, John Allan (1874). *Observations of Magnetic Declination Made at Trevandrum and Agustia Malley in the Observatories of His Highness the Maharajah of Travancore, GCSI in the Years 1852 to 1869: Being Trevandrum Magnetical Observations Volume 1*. Vol. 1. Henry S. King & Company.

Bryden, H. L. and S. Imawaki (2001). "Chapter 6.1 Ocean heat transport." In: *Ocean Circulation and Climate*. Ed. by Gerold Siedler, John Church, and John Gould. Vol. 77. International Geophysics. Academic Press, pp. 455–474. DOI: https://doi.org/10.1016/S0074-6142(01)80134-0.

Bryden, H. L., B. A. King, G. D. McCarthy, and E. L. McDonagh (2014). "Impact of a 30% reduction in Atlantic meridional overturning during 2009 – 2010." In: *Ocean Science* 10.4, pp. 683–691. DOI: 10.5194/os-10-683-2014.

Cabanes, C., A. Grouazel, K. von Schuckmann, M. Hamon, V. Turpin, C. Coatanoan, F. Paris, S. Guinehut, C. Boone, N. Ferry, C. de Boyer Montégut, T. Carval, G. Reverdin, S. Pouliquen, and P.-Y. Le Traon (2013). "The CORA dataset: validation and diagnostics of in-situ ocean temperature and salinity measurements." In: *Ocean Science* 9.1, pp. 1–18. DOI: 10.5194/os-9-1-2013.

Cai, Wenju, Simon Borlace, Matthieu Lengaigne, Peter van Rensch, Mat Collins, Gabriel Vecchi, Axel Timmermann, Agus Santoso, Michael J McPhaden, Lixin Wu, Matthew H. England, Goujian Wang, Eric Guilyardi, and Fei-Fei Jin (2014). "Increasing frequency of extreme El Niño events due to greenhouse warming." In: *Nature Climate Change* 4.2, pp. 111–116.

Canton, John (1759). "XXXVIII. An attempt to account for the regular diurnal variation of the horizontal magnetic needle; and also for its irregular variation at the time of an Aurora Borealis." In: *Philosophical Transactions of the Royal Society of London* 51, pp. 398–445.

Cartwright, DE and RJ Tayler (1971). "New computations of the tide-generating potential." In: *Geophysical Journal International* 23.1, pp. 45–73.

Chapman, S and JCP Miller (1940). "The statistical determination of lunar daily variations in geomagnetic and meteorological elements." In: *Geophysical Supplements to the Monthly Notices of the Royal Astronomical Society* 4.9, pp. 649–669.

Chave, A. D. (1983). "On the theory of electromagnetic induction in the Earth by ocean currents." In: *Journal of Geophysical Research: Solid Earth* 88.B4, pp. 3531–3542. DOI: https://doi.org/10.1029/JB088iB04p03531.

Chave, A. D. and D. S. Luther (1990). "Low-frequency, motionally induced electromagnetic fields in the ocean: 1. Theory." In: *Journal of Geophysical Research: Oceans* 95.C5, pp. 7185–7200.

Cheng, Lijing, Kevin E. Trenberth, Matthew D. Palmer, Jiang Zhu, and John P. Abraham (2016). "Observed and simulated full-depth ocean heat-content changes for 1970–2005." In: *Ocean Science* 12.4, pp. 925–935. DOI: 10.5194/os-12-925-2016.

Civet, F. and P. Tarits (2013). "Analysis of magnetic satellite data to infer the mantle electrical conductivity of telluric planets in the solar system." In: *Planetary and Space Science* 84, pp. 102–111. DOI: https://doi.org/10.1016/j.pss.2013.05.004.

Civet, F., E. Thébault, O. Verhoeven, B. Langlais, and D. Saturnino (2015). "Electrical conductivity of the Earth's mantle from the first Swarm magnetic field measurements." In: *Geophysical Research Letters* 42.9, pp. 3338–3346. DOI: https://doi.org/10.1002/2015GL063397.

Cline, William R (1991). "Scientific basis for the greenhouse effect." In: *The Economic Journal* 101.407, pp. 904–919.

Cochran, J Kirk, Henry J Bokuniewicz, and Patricia L Yager (2019). *Encyclopedia of Ocean Sciences*. Academic Press.

Constable, S. (2013). "Review paper: Instrumentation for marine magnetotelluric and controlled source electromagnetic sounding." In: *Geophysical Prospecting* 61.s1, pp. 505–532. DOI: https://doi.org/10.1111/j.1365-2478.2012.01117.x.

Cox, C. (1980). "Electromagnetic induction in the oceans and inferences on the constitution of the earth." In: *Geophysical surveys* 4 (1), pp. 137–156. DOI: 10.1007/BF01452963.

Craven, Peter and Grace Wahba (1978). "Smoothing noisy data with spline functions." In: *Numerische mathematik* 31.4, pp. 377–403.

Cueto, M., D. McKnight, and M. Herraiz (2003). "Daily geomagnetic variations on the Iberian Peninsula." In: *Geophysical Journal International* 152.1, pp. 113–123. DOI: https://doi.org/10.1046/j.1365-246X.2003.01826.x.

Doodson, Arthur Thomas (1928). "VI. The analysis of tidal observations." In: *Philosophical Transactions of the Royal Society of London. Series A, Containing Papers of a Mathematical or Physical Character* 227.647-658, pp. 223–279.

Dostal, J, Z Martinec, and M Thomas (2012). "The modelling of the toroidal magnetic field induced by tidal ocean circulation." In: *Geophysical Journal International* 189.2, pp. 782–798. DOI: 10.1111/j.1365-246X.2012.05407.x.

Duffus, H. J. and N. R. Fowler (1974). "On Planetary Voltages, Ocean Tides, and Electrical Conductivity below the Pacific." In: *Canadian Journal of Earth Sciences* 11.7, pp. 873–892. DOI: 10.1139/e74-088.

Egbert, Gary D, Andrew F Bennett, and Michael GG Foreman (1994). "TOPEX/POSEIDON tides estimated using a global inverse model." In: *Journal of Geophysical Research: Oceans* 99.C12, pp. 24821–24852.

Egbert, Gary D and Svetlana Y Erofeeva (2002). "Efficient inverse modeling of barotropic ocean tides." In: *Journal of Atmospheric and Oceanic Technology* 19.2, pp. 183–204.

Emanuel, Kerry (2018). "100 years of progress in tropical cyclone research." In: *Meteorological Monographs* 59, pp. 15–1.

Everett, M. E., S. Constable, and C. G. Constable (2003). "Effects of near-surface conductance on global satellite induction responses." In: *Geophysical Journal International* 153.1, pp. 277–286.

Faraday, M. (1832). "VI. The Bakerian lecture. - Experimental researches in electricity. - Second series." In: *Philosophical Transactions of the Royal Society of London* 122, pp. 163–194. DOI: 10.1098/rstl.1832.0007.

Ferrari, Raffaele and David Ferreira (2011). "What processes drive the ocean heat transport?" In: *Ocean Modelling* 38.3, pp. 171–186. DOI: https://doi.org/10.1016/j.ocemod.2011.02.013.

Filloux, J. H. (1987). "Instrumentation and experimental methods for oceanic studies." In: *Geomagnetism* 3, pp. 143–247.

Finlay, Christopher C., Clemens Kloss, Nils Olsen, Magnus D. Hammer, Lars Tøffner-Clausen, Alexander Grayver, and Alexey Kuvshinov (2020). "The CHAOS-7 geomagnetic field model and observed changes in the South Atlantic Anomaly." In: *Earth, Planets and Space* 72.156. DOI: 10.1186/s40623-020-01252-9.

Finlay, Christopher C., Nils Olsen, Stavros Kotsiaros, Nicolas Gillet, and Lars Tøffner-Clausen (n.d.). "Recent geomagnetic secular variation from Swarm and ground observatories as estimated in the CHAOS-6 geomagnetic field model." In: *Earth, Planets and Space* 68.112 (). DOI: 10.1186/s40623-016-0486-1.

Flosadóttir, Á. H., J. C. Larsen, and J. T. Smith (1997). "Motional induction in North Atlantic circulation models." In: *Journal of Geophysical Research: Oceans* 102.C5, pp. 10353–10372. DOI: https://doi.org/10.1029/96JC03603.

Friis-Christensen, E., H. Lühr, and G. Hulot (2006). "Swarm: A constellation to study the Earth's magnetic field." In: *Earth, planets and space* 58.4, pp. 351–358.

Fujii, I. and H. Utada (Nov. 2000). "On Geoelectric Potential Variations Over a Planetary Scale." PhD thesis. The University of Tokyo.

Gaillard, Fabienne, Thierry Reynaud, Virginie Thierry, Nicolas Kolodziejczyk, and Karina von Schuckmann (2016). "In Situ-Based Reanalysis of the Global Ocean Temperature and Salinity with ISAS: Variability of the Heat Content and Steric Height." In: *Journal of Climate* 29.4, pp. 1305–1323. DOI: 10.1175/JCLI-D-15-0028.1.

Gillet, N., V. Lesur, and N. Olsen (2010). "Geomagnetic Core Field Secular Variation Models." In: *Space Science Reviews* 155.1, pp. 129–145.

Glazman, Roman E. and Yury N. Golubev (2005). "Variability of the ocean-induced magnetic field predicted at sea surface and at satellite altitudes." In: *Journal of Geophysical Research: Oceans* 110.C12. DOI: https://doi.org/10.1029/2005JC002926.

Glynn, PW and WH De Weerdt (1991). "Elimination of two reef-building hydrocorals following the 1982-83 El Nino warming event." In: *Science(Washington)* 253.5015, pp. 69–71.

Grayver, A. V., N. R. Schnepf, A. V. Kuvshinov, T. J. Sabaka, C. Manoj, and N. Olsen (2016). "Satellite tidal magnetic signals constrain oceanic lithosphere-asthenosphere boundary." In: *Science Advances* 2.9. DOI: 10.1126/sciadv.1600798.

Grayver, A. V., F. D. Munch, A. V. Kuvshinov, A. Khan, T. J. Sabaka, and L. Tøffner-Clausen (2017). "Joint inversion of satellite-detected tidal and magnetospheric signals constrains electrical conductivity and water content of the upper mantle and transition zone." In: *Geophysical Research Letters* 44.12, pp. 6074–6081. DOI: 10.1002/2017GL073446.

Grayver, A. V. and N. Olsen (2019). "The Magnetic Signatures of the M2, N2, and O1 Oceanic Tides Observed in Swarm and CHAMP Satellite Magnetic Data." In: *Geophysical Research Letters* 46.8, pp. 4230–4238. DOI: https://doi.org/10.1029/2019GL082400.

Griffiths, D. J. (2005). *Introduction to electrodynamics*.

Guzavina, M., A. Grayver, and A. V. Kuvshinov (2018). "Do ocean tidal signals influence recovery of solar quiet variations?" In: *Earth, Planets and Space* 70.1, p. 5. DOI: 10.1186/s40623-017-0769-1.

Haagmans, Roger and Gernot Plank (2012). *Swarm: the Earth's Magnetic Field and Environment Explorers*. URL: http://pcwww.liv.ac.uk/~holme/RAS/haagmans.pdf (visited on 09/30/2021).

Hanley, Deborah E, Mark A Bourassa, James J O'Brien, Shawn R Smith, and Elizabeth R Spade (2003). "A quantitative evaluation of ENSO indices." In: *Journal of Climate* 16.8, pp. 1249–1258.

Hansen, J., R. Ruedy, M. Sato, and K. Lo (2010). "GLOBAL SURFACE TEMPERATURE CHANGE." In: *Reviews of Geophysics* 48.4. DOI: 10.1029/2010RG000345.

Harris, Charles R., K. Jarrod Millman, Stéfan J van der Walt, Ralf Gommers, Pauli Virtanen, David Cournapeau, Eric Wieser, Julian Taylor, Sebastian Berg, Nathaniel J. Smith, Robert Kern, Matti Picus, Stephan Hoyer, Marten H. van Kerkwijk, Matthew Brett, Allan Haldane, Jaime Fernández del Río, Mark Wiebe, Pearu Peterson, Pierre Gérard-Marchant, Kevin Sheppard, Tyler Reddy, Warren Weckesser, Hameer Abbasi, Christoph Gohlke, and Travis E. Oliphant (2020). "Array programming with NumPy." In: *Nature* 585, pp. 357–362. DOI: 10.1038/s41586-020-2649-2.

Harrison, DE and Paul S Schopf (1984). "Kelvin-wave-induced anomalous advection and the onset of surface warming in El Nino events." In: *Monthly Weather Review* 112.5, pp. 923–933.

Hayes, SP, LJ Mangum, J. Picaut, A Sumi, and K Takeuchi (1991). "TOGA-TAO: A moored array for real-time measurements in the tropical Pacific Ocean." In: *Bulletin of the American Meteorological Society* 72.3, pp. 339–347.

Heirtzler, J.R (2002). "The future of the South Atlantic anomaly and implications for radiation damage in space." In: *Journal of Atmospheric and Solar-Terrestrial Physics* 64.16. Space Weather Effects on Technological Systems, pp. 1701–1708. DOI: https://doi.org/10.1016/S1364-6826(02)00120-7.

Hendershott, Myrl and Walter Munk (1970). "Tides." In: *Annual review of fluid mechanics* 2.1, pp. 205–224.

Hewson-Browne, R.C. (1973). "Magnetic effects of sea tides." In: *Physics of the Earth and Planetary Interiors* 7.2, pp. 167–186. DOI: https://doi.org/10.1016/0031-9201(73)90007-1.

Holland, Paul W. and Roy E. Welsch (1977). "Robust regression using iteratively reweighted least-squares." In: *Communications in Statistics - Theory and Methods* 6.9, pp. 813–827. DOI: 10.1080/03610927708827533.

Huber, Peter J (2004). *Robust statistics*. Vol. 523. John Wiley & Sons.

IOC, SCOR, and APSO (2010). "The International thermodynamic equation of seawater–2010: Calculation and use of thermodynamic properties, Intergovernmental Oceanographic Commission." In: *Manual and Guides* 56, 196 pp.

Irrgang, C. (2017). "Characterization of oceanic signatures in the Earth's magnetic field in view of their applicability as ocean model constraints." PhD thesis.

Irrgang, C., J. Saynisch-Wagner, and M. Thomas (2018). "Depth of origin of ocean-circulation-induced magnetic signals." In: *Annales Geophysicae* 36.1, pp. 167–180.

Irrgang, C., J. Saynisch, and M. Thomas (2016a). "Ensemble simulations of the magnetic field induced by global ocean circulation: Estimating the uncertainty." In: *Journal of Geophysical Research: Oceans* 121.3, pp. 1866–1880.

— (2016b). "Impact of variable seawater conductivity on motional induction simulated with an ocean general circulation model." In: *Ocean Science* 12.1, pp. 129–136. DOI: 10.5194/os-12-129-2016.

— (2017). "Utilizing oceanic electromagnetic induction to constrain an ocean general circulation model: A data assimilation twin experiment." In: *Journal of Advances in Modeling Earth Systems* 9.3, pp. 1703–1720.

— (2019). "Estimating global ocean heat content from tidal magnetic satellite observations." In: *Scientific Reports* 9.7893, pp. 2045–2322. DOI: 10.1038/s41598-019-44397-8.

Jackson, J. D. (2009). "Classical electrodynamics." In: *American Institute of Physics* 15.11, pp. 62–62.

Jager, T, Jean-Michel Léger, F Bertrand, I Fratter, and JC Lalaurie (2010). "SWARM Absolute Scalar Magnetometer accuracy: analyses and measurement results." In: *2010 IEEE Sensors*. IEEE, pp. 2392–2395. DOI: 10.1109/ICSENS.2010.5690960.

Ji, Ming, Richard W. Reynolds, and David W. Behringer (2000). "Use of TOPEX/Poseidon Sea Level Data for Ocean Analyses and ENSO Prediction: Some Early Results." In: *Journal of Climate* 13.1, pp. 216–231.

Jin, Jian-Ming (2015). *Theory and computation of electromagnetic fields*. John Wiley & Sons.

Junge, A. (Dec. 1988). "The telluric field in northern Germany induced by tidal motion in the North Sea." In: *Geophysical Journal International* 95.3, pp. 523–533. DOI: 10.1111/j.1365-246X.1988.tb06701.x.

Kauristie, K, Achim Morschhauser, Nils Olsen, Christopher C. Finlay, RL McPherron, JW Gjerloev, and Hermann J Opgenoorth (2017). "On the usage of geomagnetic indices for data selection in internal field modelling." In: *Space Science Reviews* 206.1-4, pp. 61–90. DOI: 10.1007/s11214-016-0301-0.

Kelbert, Anna, Alexey Kuvshinov, Jakub Velímský, Takao Koyama, Joseph Ribaudo, Jin Sun, Zdenek Martinec, and Chester J. Weiss (2014). "Global 3-D electromagnetic forward modelling: a benchmark study." In: *Geophysical Journal International* 197.2, pp. 785–814. DOI: 10.1093/gji/ggu028.

Kelley, Michael C (2009). *The Earth's ionosphere: plasma physics and electrodynamics*. Academic press.

Kreil, Karl (1852). *Einfluss des Mondes auf die magnetische Declination*. Vol. 1. Kaiserlich-Königlichen Hof-und Staatsdruckerei.

Kruglyakov, M. and A. Kuvshinov (2020). "Introducing new global electromagnetic modeling solver." In:

Kuvshinov, A. V. (2008). "3-D Global Induction in the Oceans and Solid Earth: Recent Progress in Modeling Magnetic and Electric Fields from Sources of Magnetospheric, Ionospheric and Oceanic Origin." In: *Surveys in Geophysics* 29.2, pp. 139–186.

Kuvshinov, A. V., D. B. Avdeev, O. V. Pankratov, S. A. Golyshev, and N. Olsen (2002). "Chapter 3 Modelling electromagnetic fields in a 3D spherical earth using a fast integral equation approach." In: *Three-Dimensional Electromagnetics*. Ed. by Michael S. Zhdanov and Philip E. Wannamaker. Vol. 35. Methods in Geochemistry and Geophysics. Elsevier, pp. 43–54. DOI: https://doi.org/10.1016/S0076-6895(02)80085-3.

Kuvshinov, A. V., A. Junge, and H. Utada (2006). "3-D modelling the electric field due to ocean tidal flow and comparison with observations." In: *Geophysical Research Letters* 33.6. DOI: 10.1029/2005GL025043.

Kuvshinov, A. V. and N. Olsen (2005). "3-D Modelling of the Magnetic Fields Due to Ocean Tidal Flow." In: *Earth Observation with CHAMP: Results from Three Years in Orbit*. Ed. by Christoph Reigber, Hermann Lühr, Peter Schwintzer, and Jens Wickert. Berlin, Heidelberg: Springer Berlin Heidelberg, pp. 359–365. DOI: 10.1007/3-540-26800-6_57.

Larsen, J. C. and T. B. Sanford (1985). "Florida Current volume transports from voltage measurements." In: *Science* 227.4684, pp. 302–304. DOI: 10.1126/science.227.4684.302.

Larsen, J. C. and F. T. Smith (1992). "Transport and heat flux of the Florida Current at 27 degrees N derived from cross-stream voltages and profiling data: theory and observations." In: *Philosophical Transactions of the Royal Society A: Mathematical, Physical and Engineering Sciences* 338.1650, pp. 169–236. DOI: 10.1098/rsta.1992.0007.

Larsen, J.C. (1973). "An introduction to electromagnetic induction in the ocean." In: *Physics of the Earth and Planetary Interiors* 7.3, pp. 389–398. DOI: https://doi.org/10.1016/0031-9201(73)90063-0.

Laske, G. and G. Masters (1997). "A Global Digital Map of Sediment Thickness." In: *EOS Transactions AGU*. Vol. 78(46). Fall Meeting Supplement, Abstract S4E1-01. F483.

Lesur, Vincent, Ingo Wardinski, Mohamed Hamoudi, and Martin Rother (2010). "The second generation of the GFZ reference internal magnetic model: GRIMM-2." In: *Earth, planets and space* 62.10, pp. 765–773.

Lesur, Vincent, Ingo Wardinski, Martin Rother, and Mioara Mandea (2008). "GRIMM: the GFZ Reference Internal Magnetic Model based on vector satellite and observatory data." In: *Geophysical Journal International* 173.2, pp. 382–394.

Levitus, S., J. I. Antonov, T. P. Boyer, O. K. Baranova, H. E. Garcia, R. A. Locarnini, A. V. Mishonov, J. R. Reagan, D. Seidov, E. S. Yarosh, and M. M. Zweng (2012). "World ocean heat content and thermosteric sea level change (0-2000 m), 1955-2010." In: *Geophysical Research Letters* 39.10. DOI: 10.1029/2012GL051106.

Levitus, S., J. I. Antonov, J. Wang, T. L. Delworth, K. W. Dixon, and A. J. Broccoli (2001). "Anthropogenic Warming of Earth's Climate System." In: *Science* 292.5515, pp. 267–270. DOI: 10.1126/science.1058154.

Liang, Yu-Chiao, Jin-Yi Yu, Eric S. Saltzman, and Fan Wang (2017). "Linking the Tropical Northern Hemisphere Pattern to the Pacific Warm Blob and Atlantic Cold Blob." In: *Journal of Climate* 30.22, pp. 9041–9057. DOI: 10.1175/JCLI-D-17-0149.1.

Lilley, F. E. M., J. H. Filloux, P. J. Mulhearn, and I. J. Ferguson (1993). "Magnetic Signals from an Ocean Eddy." In: *Journal of geomagnetism and geoelectricity* 45.5, pp. 403–422. DOI: 10.5636/jgg.45.403.

Lilley, F. E. M., A. P. Hitchman, P. R. Milligan, and T. Pedersen (Nov. 2004). "Sea-surface observations of the magnetic signals of ocean swells." In: *Geophysical Journal International* 159.2, pp. 565–572. DOI: 10.1111/j.1365-246X.2004.02420.x.

Locarnini, Ricardo A, Alexey V Mishonov, John I Antonov, Timothy P Boyer, Hernan E Garcia, Olga K Baranova, Melissa M Zweng, Christopher R Paver, James R Reagan, Daphne R Johnson, et al. (2013). "World ocean atlas 2013. Volume 1, Temperature." In: *NOAA Atlas NESDIS*.

Loeb Norman G.and Lyman, John M., Gregory C. Johnson, Richard P. Allan, David R. Doelling, Takmeng Wong, Brian J. Soden, and Graeme L. Stephens (2012). "Observed changes in top-of-the-atmosphere radiation and upper-ocean heating consistent within uncertainty." In: *Nature Geoscience* 5. DOI: 10.1038/ngeo1375.

Lomb, N. R. (1976). "Least-squares frequency analysis of unequally spaced data." In: *Astrophysics and Space Science* 39.11, pp. 447–462. DOI: 10.1007/BF00648343.

Longuet-Higgins, M. S. and G. E. R. Deacon (1949). "The Electrical and Magnetic Effects of Tidal Streams." In: *Geophysical Journal International* 5.8, pp. 285–307. DOI: https://doi.org/10.1111/j.1365-246X.1949.tb02945.x.

Lorrain, Paul, Francois Lorrain, and Stephane Houle (2006). "Ohm's Law for Moving Conductors." In: *Magneto-Fluid Dynamics: Fundamentals and Case Studies of Natural Phenomena*. New York, NY: Springer New York, pp. 73–86. DOI: 10.1007/978-0-387-47290-4_6.

Love, J. J. and Arnaud Chulliat (2013). "An International Network of Magnetic Observatories." In: *Eos, Transactions American Geophysical Union* 94.42, pp. 373–374. DOI: 10.1002/2013EO420001.

Love, J. J. and E. J. Rigler (Apr. 2014). "The magnetic tides of Honolulu." In: *Geophysical Journal International* 197.3, pp. 1335–1353. DOI: 10.1093/gji/ggu090.

Ludescher, Josef, Armin Bunde, Shlomo Havlin, and Hans Joachim Schellnhuber (2019). *Very early warning signal for El Niño in 2020 with a 4 in 5 likelihood*. arXiv: 1910.14642 [physics.ao-ph].

Macdonald, Alison M. and Molly O. Baringer (2013). "Chapter 29 - Ocean Heat Transport." In: *Ocean Circulation and Climate*. Ed. by Gerold Siedler, Stephen M. Griffies, John Gould, and John A. Church. Vol. 103. International Geophysics. Academic Press, pp. 759–785. DOI: https://doi.org/10.1016/B978-0-12-391851-2.00029-5.

Malin, S. R. C. (Dec. 1970). "Separation of Lunar Daily Geomagnetic Variations into Parts of Ionospheric and Oceanic Origin." In: *Geophysical Journal International* 21.5, pp. 447–455. DOI: 10.1111/j.1365-246X.1970.tb01781.x.

Manoj, C., A. Kuvshinov, S. Maus, and H. Lühr (2006). "Ocean circulation generated magnetic signals." In: *Earth, Planets and Space* 58.4, pp. 429–437. DOI: 10.1186/BF03351939.

Marsland, Simon J, Helmuth Haak, Johann H Jungclaus, Mojib Latif, and Frank Röske (2003). "The Max-Planck-Institute global ocean/sea ice model with orthogonal curvilinear coordinates." In: *Ocean modelling* 5.2, pp. 91–127.

Matsushita, S. (1967). "Lunar Tides in the Ionosphere." In: *Geophysics III. / Encyclopedia of Physics*. Ed. by J. Bartel. Springer. Chap. 2, pp. 547–602.

Maus, S. and A. V. Kuvshinov (2004). "Ocean tidal signals in observatory and satellite magnetic measurements." In: *Geophysical Research Letters* 31.15. DOI: https://doi.org/10.1029/2004GL020090.

Maus, S., M. Rother, K. Hemant, C. Stolle, H. Lühr, A. Kuvshinov, and N. Olsen (Feb. 2006). "Earth's lithospheric magnetic field determined to spherical harmonic degree 90 from CHAMP satellite measurements." In: *Geophysical Journal International* 164.2, pp. 319–330. DOI: 10.1111/j.1365-246X.2005.02833.x.

McCarthy, Gerard D., Ivan D. Haigh, Joël J.-M. Hirschi, Jeremy P. Grist, and David A. Smeed (2015). "Ocean impact on decadal Atlantic climate variability revealed by sea-level observations." In: *Nature* 521, pp. 508–510. DOI: 10.1038/nature14491.

McKnight, J. D. (Dec. 1995). "Lunar daily geomagnetic variations in New Zealand." In: *Geophysical Journal International* 122.3, pp. 889–898. DOI: 10.1111/j.1365-246X.1995.tb06844.x.

McPhaden, Michael J. (1999). "Genesis and Evolution of the 1997-98 El Niño." In: *Science* 283.5404, pp. 950–954.

Meinen, Christopher S and Michael J McPhaden (2000). "Observations of warm water volume changes in the equatorial Pacific and their relationship to El Niño and La Niña." In: *Journal of Climate* 13.20, pp. 3551–3559.

Meng, Jun, Jingfang Fan, Josef Ludescher, Ankit Agarwal, Xiaosong Chen, Armin Bunde, Jürgen Kurths, and Hans Joachim Schellnhuber (2020). "Complexity-based approach for El Niño magnitude forecasting before the spring predictability barrier." In: *Proceedings of the National Academy of Sciences* 117.1, pp. 177–183. DOI: 10.1073/pnas.1917007117.

Meyssignac, Benoit, Tim Boyer, Zhongxiang Zhao, Maria Z Hakuba, Felix W Landerer, Detlef Stammer, Armin Köhl, Seiji Kato, Tristan L'Ecuyer, Michael Ablain, et al. (2019). "Measuring Global Ocean Heat Content to estimate the Earth Energy Imbalance." In: *Frontiers in Marine Science* 6, p. 432. DOI: 10.3389/fmars.2019.00432.

Minami, T. (2017). "Motional Induction by Tsunamis and Ocean Tides: 10 Years of Progress." In: *Surveys in Geophysics* 38.5, pp. 1097–1132.

Minami, T., N. R Schnepf, and H. Toh (2021). "Tsunami-generated magnetic fields have primary and secondary arrivals like seismic waves." In: *Scientific reports* 11.1, pp. 1–8. DOI: 10.1038/s41598-021-81820-5.

Minami, T., H. Toh, and R. H. Tyler (2015). "Properties of electromagnetic fields generated by tsunami first arrivals: Classification based on the ocean depth." In: *Geophysical Research Letters* 42.7, pp. 2171–2178. DOI: https://doi.org/10.1002/2015GL063055.

Mitchell, John FB (1989). "The "greenhouse" effect and climate change." In: *Reviews of Geophysics* 27.1, pp. 115–139.

Müller, Malte, Josef Y. Cherniawsky, Michael G. G. Foreman, and Jin-Song von Storch (2014). "Seasonal variation of the M2 tide." In: *Ocean Dynamics* 64.2, pp. 159–177. DOI: 10.1007/s10236-013-0679-0.

NOAA (2017). *Cold & Warm Episodes by Season*. last accessed: 2018-06-18. URL: http://www.cpc.ncep.noaa.gov/products/analysis%5C_monitoring%5C%5C/ensostuff/ensoyears2011.shtml.

Null, Jan (2017). *El Niño and La Niña years and intensities*. 2018-06-18. URL: http://ggweather.com/enso/oni.htm.

Ocean Studies Board, National Research Council (US) (2000). *50 Years of Ocean Discovery: National Science Foundation 1950-2000*. Washington (DC): National Academies Press (US).

Olsen, N., E. Friis-Christensen, R. Floberghagen, P. Alken, C. D. Beggan, A. Chulliat, E. Doornbos, J. T. da Encarnação, B. Hamilton, G. Hulot, J. van den IJssel, A. Kuvshinov, V. Lesur, H. Lühr, S. Maus Macmillan, M. Noja, P. E. H. Olsen, J. Park, G. Plank, C. Püthe, J. Rauberg, P. Ritter, M. Rother, T. J. Sabaka, R. Schachtschneider, O. Sirol, C. Stolle, E. Thébault, A. W. P. Thomson, L. Tøffner-Clausen, J. Velímský, P. Vigneron, and P. N. Visser (2013). "The Swarm Satellite Constellation Application and Research Facility (SCARF) and Swarm data products." In: *Earth, Planets and Space* 65 (11). DOI: 10.5047/eps.2013.07.001.

Palshin, N. A. (1996). "Oceanic electromagnetic studies: a review." In: *Surveys in Geophysics* 17.4, pp. 455–491.

Pankratov, O. V., D. B. Avdeyev, and A. V. Kuvshinov (1995). "Electromagnetic field scattering in a heterogeneous Earth: A solution to the forward problem." In: *Solid Earth* 31, pp. 201–209.

Pankratov, O. V., A. V. Kuvshinov, and D. B. Avdeev (1997). "High-Performance Three-Dimensional Electromagnetic Modelling Using Modified Neumann Series. Anisotropic Earth." In: *Journal of geomagnetism and geoelectricity* 49.11-12, pp. 1541–1547. DOI: 10.5636/jgg.49.1541.

Parker, Bruce B (2007). *Tidal analysis and prediction.*

Pavón-Carrasco, F. Javier and Angelo De Santis (2016). "The South Atlantic Anomaly: The Key for a Possible Geomagnetic Reversal." In: *Frontiers in Earth Science* 4. DOI: 10.3389/feart.2016.00040.

Petereit, J., J. Saynisch-Wagner, C. Irrgang, and M. Thomas (2019). "Analysis of Ocean Tide-Induced Magnetic Fields Derived From Oceanic In Situ Observations: Climate Trends and the Remarkable Sensitivity of Shelf Regions." In: *Journal of Geophysical Research: Oceans* 124.11, pp. 8257–8270. DOI: 10.1029/2018JC014768.

Petereit, J., J. Saynisch, C. Irrgang, T. Weber, and M. Thomas (2018). "Electromagnetic characteristics of ENSO." In: *Ocean Science* 14.3, pp. 515–524. DOI: 10.5194/os-14-515-2018.

Philander, SGH (1983). "Meteorology: Anomalous El Niño of 1982–83." In: *Nature* 305.5929, pp. 16–16.

Phillips, Norman A. (1963). "Geostrophic motion." In: *Reviews of Geophysics* 1.2, pp. 123–176. DOI: https://doi.org/10.1029/RG001i002p00123.

Picaut, J., Eric Hackert, Antonio J. Busalacchi, Ragu Murtugudde, and Gary S. E. Lagerloef (2002). "Mechanisms of the 1997-1998 El Niño-La Niña, as inferred from space-based observations." In: *Journal of Geophysical Research: Oceans* 107.C5, pp. 5-1–5-18.

Picaut, J., M. Ioualalen, C. Menkes, T. Delcroix, and M. J. McPhaden (1996). "Mechanism of the Zonal Displacements of the Pacific Warm Pool: Implications for ENSO." In: *Science* 274.5292, pp. 1486–1489.

Preisendorfer, Rudolph W, Jack C Larsen, and Michael A Sklarz (1974). *Electromagnetic fields induced by plane-parallel internal and surface ocean waves*. Vol. 74. 7. Hawaii Institute of Geophysics, University of Hawaii.

Press, William H, H William, Saul A Teukolsky, William T Vetterling, A Saul, and Brian P Flannery (2007). *Numerical recipes 3rd edition: The art of scientific computing*. Cambridge university press.

PRICE, A. T. (Jan. 1950). "ELECTROMAGNETIC INDUCTION IN A SEMI-INFINITE CONDUCTOR WITH A PLANE BOUNDARY." In: *The Quarterly Journal of Mechanics and Applied Mathematics* 3.4, pp. 385–410. DOI: 10.1093/qjmam/3.4.385.

Pugh, D. (Jan. 1987). *Tides, surges and mean sea level*. URL: https://www.osti.gov/biblio/5061261.

Pugh, D. and P. Woodworth (2014). *Sea-level science: understanding tides, surges, tsunamis and mean sea-level changes*. Cambridge University Press.

Püthe, C. and A. V. Kuvshinov (2013). "Determination of the 3-D distribution of electrical conductivity in Earth's mantle from Swarm satellite data: Frequency domain approach based on inversion of induced coefficients." In: *Earth, Planets and Space* 65 (11). DOI: 10.5047/eps.2013.09.004.

— (2014). "Mapping 3-D mantle electrical conductivity from space: a new 3-D inversion scheme based on analysis of matrix Q-responses." In: *Geophysical Journal International* 197.2, pp. 768–784. DOI: 10.1093/gji/ggu027.

Püthe, C., A. V. Kuvshinov, A. Khan, and N. Olsen (2015). "A new model of Earth's radial conductivity structure derived from over 10 yr of satellite and observatory magnetic data." In: *Geophysical Journal International* 203.3, p. 1864. DOI: 10.1093/gji/ggv407.

Roeckner, E, K Arpe, L Bengtsson, M Christoph, M Claussen, L Dümenil, M Esch, M Giorgetta, U Schlese, and U Schulzweida (1996). "The atmospheric general circulation model ECHAM-4: Model description and simulation of present-day climate." In: *Max Planck Inst. Meteorol., Hamburg, Germany* 218, p. 90.

Roemmich, Dean, Gregory C. Johnson, Stephen Riser, Russ Davis, John Gilson, W. Brechner Owens, Silvia L. Garzoli, Claudia Schmid, and Mark Ignaszewski (2009). "The Argo Program: Observing the Global Ocean with Profiling Floats." In: *Oceanography* 22. DOI: 10.5670/oceanog.2009.36.

Sabaka, T. J., Lars Tøffner-Clausen, Nils Olsen, and Christopher C. Finlay (2018). "A comprehensive model of Earth's magnetic field determined from 4 years of Swarm satellite observations." In: *Earth, Planets and Space* 70.1, p. 130. DOI: 10.1186/s40623-018-0896-3.

Sabaka, T. J., R. H. Tyler, and N. Olsen (2016). "Extracting ocean-generated tidal magnetic signals from Swarm data through satellite gradiometry." In: *Geophysical Research Letters* 43.7, pp. 3237–3245.

Sabaka, T. J., R. H. Tyler, N. Olsen, and A. V. Kuvshinov (2015). "CM5, a pre-Swarm comprehensive geomagnetic field model derived from over 12 yr of CHAMP, Ørsted, SAC-C and observatory data." In: *Geophysical Journal International* 200.3, pp. 1596–1626. DOI: 10.1093/gji/ggu493.

Sabine, Edward (1857). "I. On the evidence of the existence of the decennial inequality in the solar-diurnal magnetic variations, and its non-existence in the lunar-diurnal variation, of the declination at Hobarton." In: *Philosophical Transactions of the Royal Society of London* 147, pp. 1–8.

Sachl, L., Z. Martinec, J. Velímský, C. Irrgang, J. Petereit, J. Saynisch, D. Einspigel, and N. R. Schnepf (2019). "Modelling of electromagnetic signatures of global ocean

circulation: physical approximations and numerical issues." In: *Earth, Planets and Space* 71.1, p. 58. DOI: 10.1186/s40623-019-1033-7.

Sanford, T. B. (1971). "Motionally induced electric and magnetic fields in the sea." In: *Journal of Geophysical Research* 76.15, pp. 3476–3492. DOI: https://doi.org/10.1029/JC076i015p03476.

Sanford, T. B., J.H. Dunlap, J.A. Carlson, D.C. Webb, and J.B. Girton (June 2005). "Autonomous velocity and density profiler: EM-APEX." In: *Proceedings of the IEEE/OES Eighth Working Conference on Current Measurement Technology, 2005.* Pp. 152–156. DOI: 10.1109/CCM.2005.1506361.

Sanford, T. B., J. F. Price, and J. B. Girton (2011). "Upper-Ocean Response to Hurricane Frances (2004) Observed by Profiling EM-APEX Floats." In: *Journal of Physical Oceanography* 41.6, pp. 1041–1056. DOI: 10.1175/2010JPO4313.1.

Sanford, T. B., J. F. Price, J. B. Girton, and D. C. Webb (2007). "Highly resolved observations and simulations of the ocean response to a hurricane." In: *Geophysical Research Letters* 34.13. DOI: https://doi.org/10.1029/2007GL029679.

Saynisch-Wagner, J., J. Petereit, C. Irrgang, and M. Thomas (2020). "Phase Changes of Electromagnetic Oceanic Tidal Signals." In: *Journal of Geophysical Research: Oceans* 125.4. e2019JC015960 10.1029/2019JC015960, e2019JC015960. DOI: https://doi.org/10.1029/2019JC015960.

Saynisch, J., C. Irrgang, and M. Thomas (2018). "On the Use of Satellite Altimetry to Detect Ocean Circulation's Magnetic Signals." In: *Journal of Geophysical Research: Oceans* 123.3, pp. 2305–2314. DOI: https://doi.org/10.1002/2017JC013742.

Saynisch, J., J. Petereit, C. Irrgang, A. V. Kuvshinov, and M. Thomas (2016). "Impact of climate variability on the tidal oceanic magnetic signal - A model-based sensitivity study." In: *Journal of Geophysical Research: Oceans* 121.8, pp. 5931–5941.

Saynisch, J., J. Petereit, C. Irrgang, and M. Thomas (2017). "Impact of oceanic warming on electromagnetic oceanic tidal signals: A CMIP5 climate model-based sensitivity study." In: *Geophysical Research Letters* 44.10, pp. 4994–5000.

Scargle, J.D. (Dec. 1982). "Studies in Astronomical Time Series Analysis. II. Statistical Aspects of Spectral Analysis of Unevenly Spaced Data." In: *The Astrophysical Journal* 263, pp. 835–853.

Schmelz, M, R Stolz, V Zakosarenko, T Schönau, S Anders, L Fritzsch, M Mück, and HG Meyer (2011). "Field-stable SQUID magnetometer with sub-fT Hz- 1/2 resolution based on sub-micrometer cross-type Josephson tunnel junctions." In: *Superconductor Science and Technology* 24.6, p. 065009. DOI: 10.1016/j.physc.2012.06.005.

Schnepf, N. R., A. Kuvshinov, and T. Sabaka (2015). "Can we probe the conductivity of the lithosphere and upper mantle using satellite tidal magnetic signals?" In: *Geophysical Research Letters* 42.9, pp. 3233–3239. DOI: 10.1002/2015GL063540.

Schnepf, N. R., C. Manoj, C. An, H. Sugioka, and H. Toh (2016). "Time–frequency characteristics of tsunami magnetic signals from four Pacific Ocean events." In: *Global Tsunami Science: Past and Future, Volume I*. Springer, pp. 3935–3953.

Schnepf, N. R., C. Manoj, A. Kuvshinov, H. Toh, and S. Maus (2014). "Tidal signals in ocean-bottom magnetic measurements of the Northwestern Pacific: observation versus prediction." In: *Geophysical Journal International* 198.2, pp. 1096–1110. DOI: 10.1093/gji/ggu190.

Schnepf, N. R., M. Nair, A. Maute, N. M. Pedatella, A. Kuvshinov, and A. D. Richmond (2018). "A Comparison of Model-Based Ionospheric and Ocean Tidal Magnetic Signals With Observatory Data." In: *Geophysical Research Letters* 45.15, pp. 7257–7267. DOI: https://doi.org/10.1029/2018GL078487.

Schureman, Paul (1958). *Manual of harmonic analysis and prediction of tides*. Vol. 4. US Government Printing Office.

Segawa, J. and H. Toh (1992). "Detecting fluid circulation by electric field variations at the Nankai Trough." In: *Earth and planetary science letters* 109.3-4, pp. 469–476.

Shimizu, Hisayoshi, Asami Yoneda, Kiyoshi Baba, Hisashi Utada, and Nikolay A. Palshin (2011). "Sq effect on the electromagnetic response functions in the period range between 104 and 105 s." In: *Geophysical Journal International* 186.1, pp. 193–206. DOI: 10.1111/j.1365-246X.2011.05036.x.

Singer, B Sh and EB Fainberg (1995). "Generalization of the iterative dissipative method for modeling electromagnetic fields in nonuniform media with displacement currents." In: *Journal of applied geophysics* 34.1, pp. 41–46.

Smith, J. T. (Oct. 1996a). "Conservative modeling of 3-D electromagnetic fields, Part I: Properties and error analysis." In: *Geophysics* 61.5, pp. 1308–1318. DOI: 10.1190/1.1444054.

— (Oct. 1996b). "Conservative modeling of 3-D electromagnetic fields, Part II: Biconjugate gradient solution and an accelerator." In: *Geophysics* 61.5, pp. 1319–1324. DOI: 10.1190/1.1444055.

Stephenson, D. and K. Bryan (1992). "Large-scale electric and magnetic fields generated by the oceans." In: *Journal of Geophysical Research: Oceans* 97.C10, pp. 15467–15480. DOI: https://doi.org/10.1029/92JC01400.

Stride, A. H. (1983). "Offshore Tidal Sands: Processes and Deposits." In: *Journal of the Marine Biological Association of the United Kingdom* 63.3, pp. 738–738. DOI: 10.1017/S0025315400071149.

Sulzbach, Roman, H Dobslaw, and M Thomas (2021). "High-Resolution Numerical Modelling of Barotropic Global Ocean Tides for Satellite Gravimetry." In: *Journal of Geophysical Research: Oceans*, e2020JC017097.

Szuts, Z. B. (2012). "Using motionally-induced electric signals to indirectly measure ocean velocity: Instrumental and theoretical developments." In: *Progress in Oceanography* 96.1, pp. 108–127. DOI: https://doi.org/10.1016/j.pocean.2011.11.014.

Taylor, Karl E, Ronald J Stouffer, and Gerald A Meehl (2012). "An overview of CMIP5 and the experiment design." In: *Bulletin of the American Meteorological Society* 93.4, pp. 485–498.

Thébault, Erwan, Christopher C. Finlay, Ciarán D. Beggan, Patrick Alken, Julien Aubert, Olivier Barrois, Francois Bertrand, Tatiana Bondar, Axel Boness, Laura Brocco, Elisabeth Canet, Aude Chambodut, Arnaud Chulliat, Pierdavide Coïsson, François Civet, Aimin Du, Alexandre Fournier, Isabelle Fratter, Nicolas Gillet, Brian Hamilton, Mohamed Hamoudi, Gauthier Hulot, Thomas Jager, Monika Korte, Weijia Kuang, Xavier Lalanne, Benoit Langlais, Jean-Michel Léger, Vincent Lesur, Frank J. Lowes, Susan Macmillan, Mioara Mandea, Chandrasekharan Manoj, Stefan Maus, Nils Olsen, Valeriy Petrov, Victoria Ridley, Martin Rother, Terence J. Sabaka, Diana Saturnino, Reyko Schachtschneider, Olivier Sirol, Andrew Tangborn, A. Thomson, Lars Tøffner-Clausen, Pierre Vigneron,

Ingo Wardinski, and Tatiana Zvereva (2015). "International Geomagnetic Reference Field: the 12th generation." In: *Earth, Planets and Space* 67.1, p. 79. DOI: 10.1186/s40623-015-0228-9.

Thomas, M. (2002). "Ozeanisch induzierte Erdrotationsschwankungen: Ergebnisse eines Simultanmodells für Zirkulation und ephemeridische Gezeiten im Weltozean." PhD thesis. Staats-und Universitätsbibliothek Hamburg Carl von Ossietzky.

Thomson, D. J., L. J. Lanzerotti, L. V. Medford, C. G. Maclennan, A. Meloni, and G. P. Gregori (1986). "Study of tidal periodicities using a Transatlantic telecommunications cable." In: *Geophysical Research Letters* 13.6, pp. 525–528. DOI: 10.1029/GL013i006p00525.

Thomson, R. E and W. J Emery (2014). *Data analysis methods in physical oceanography*. Newnes.

Tilbrook, Bronte, Elizabeth B. Jewett, Michael D. DeGrandpre, Jose Martin Hernandez-Ayon, Richard A. Feely, Dwight K. Gledhill, Lina Hansson, Kirsten Isensee, Meredith L. Kurz, Janet A. Newton, Samantha A. Siedlecki, Fei Chai, Sam Dupont, Michelle Graco, Eva Calvo, Dana Greeley, Lydia Kapsenberg, Marine Lebrec, Carles Pelejero, Katherina L. Schoo, and Maciej Telszewski (2019). "An Enhanced Ocean Acidification Observing Network: From People to Technology to Data Synthesis and Information Exchange." In: *Frontiers in Marine Science* 6, p. 337. DOI: 10.3389/fmars.2019.00337.

Toh, H., K. Satake, Y. Hamano, Y. Fujii, and T. Goto (2011). "Tsunami signals from the 2006 and 2007 Kuril earthquakes detected at a seafloor geomagnetic observatory." In: *Journal of Geophysical Research: Solid Earth* 116.B2. DOI: https://doi.org/10.1029/2010JB007873.

Torres, Carlos E., Ignacia Calisto, and Dante Figueroa (2019). "Magnetic Signals at Easter Island During the 2010 and 2015 Chilean Tsunamis Compared with Numerical Models." In: *Pure and Applied Geophysics* 176 (7), pp. 3167–3183. DOI: 10.1007/s00024-018-2047-y.

Trossman, D. S. and R. H. Tyler (2019). "Predictability of Ocean Heat Content From Electrical Conductance." In: *Journal of Geophysical Research: Oceans* 124.1, pp. 667–679. DOI: 10.1029/2018JC014740.

Tyler, R. H., T. P. Boyer, T. Minami, M. M. Zweng, and J. R. Reagan (2017). "Electrical conductivity of the global ocean." In: *Earth, Planets and Space* 69.1, p. 156. DOI: 10.1186/s40623-017-0739-7.

Tyler, R. H., S. Maus, and H. Lühr (2003). "Satellite Observations of Magnetic Fields Due to Ocean Tidal Flow." In: *Science* 299.5604, pp. 239–241.

Tyler, R. H. and L. A. Mysak (1995). "Motionally-induced electromagnetic fields generated by idealized ocean currents." In: *Geophysical & Astrophysical Fluid Dynamics* 80.3-4, pp. 167–204.

Tyler, R. H., L. A. Mysak, and J. M. Oberhuber (1997). "Electromagnetic fields generated by a three dimensional global ocean circulation." In: *Journal of Geophysical Research: Oceans* 102.C3, pp. 5531–5551. DOI: https://doi.org/10.1029/96JC03545.

VanderPlas, Jacob T. (May 2018). "Understanding the Lomb–Scargle Periodogram." In: *The Astrophysical Journal Supplement Series* 236.1, p. 16. DOI: 10.3847/1538-4365/aab766.

Velímský, J. (2010). "Electrical conductivity in the lower mantle: Constraints from CHAMP satellite data by time-domain EM induction modelling." In: *Physics of the Earth and Planetary Interiors* 180.3. Transport properties of the lower mantle, pp. 111–117. DOI: https://doi.org/10.1016/j.pepi.2010.02.007.

— (2013). "Determination of three-dimensional distribution of electrical conductivity in the Earth's mantle from Swarm satellite data: Time-domain approach." In: *Earth, Planets and Space* 65 (11). DOI: 10.5047/eps.2013.08.001.

Velímský, J., A. Grayver, A. Kuvshinov, and L. Šachl (2018). "On the modelling of $M2$ tidal magnetic signatures: effects of physical approximations and numerical resolution." In: *Earth, Planets and Space* 70.1, p. 192. DOI: 10.1186/s40623-018-0967-5.

Velímský, J. and Z. Martinec (Apr. 2005). "Time-domain, spherical harmonic-finite element approach to transient three-dimensional geomagnetic induction in a spherical heterogeneous Earth." In: *Geophysical Journal International* 161.1, pp. 81–101. DOI: 10.1111/j.1365-246X.2005.02546.x.

Velímský, J., L. Šachl, and Z. Martinec (2019). "The global toroidal magnetic field generated in the Earth's oceans." In: *Earth and Planetary Science Letters* 509, pp. 47–54. DOI: https://doi.org/10.1016/j.epsl.2018.12.026.

Vincent, Emmanuel M, Matthieu Lengaigne, Christophe E Menkes, Nicolas C Jourdain, Patrick Marchesiello, and Gurvan Madec (2011). "Interannual variability of the South Pacific Convergence Zone and implications for tropical cyclone genesis." In: *Climate Dynamics* 36.9-10, pp. 1881–1896.

Virtanen, Pauli, Ralf Gommers, Travis E. Oliphant, Matt Haberland, Tyler Reddy, David Cournapeau, Evgeni Burovski, Pearu Peterson, Warren Weckesser, Jonathan Bright, Stéfan J. van der Walt, Matthew Brett, Joshua Wilson, K. Jarrod Millman, Nikolay Mayorov, Andrew R. J. Nelson, Eric Jones, Robert Kern, Eric Larson, C J Carey, İlhan Polat, Yu Feng, Eric W. Moore, Jake VanderPlas, Denis Laxalde, Josef Perktold, Robert Cimrman, Ian Henriksen, E. A. Quintero, Charles R. Harris, Anne M. Archibald, Antônio H. Ribeiro, Fabian Pedregosa, Paul van Mulbregt, and SciPy 1.0 Contributors (2020). "SciPy 1.0: Fundamental Algorithms for Scientific Computing in Python." In: *Nature Methods* 17, pp. 261–272. DOI: 10.1038/s41592-019-0686-2.

Vivier, F., E. Maier-Reimer, and R. H. Tyler (2004). "Simulations of magnetic fields generated by the Antarctic Circumpolar Current at satellite altitude: Can geomagnetic measurements be used to monitor the flow?" In: *Geophysical Research Letters* 31.10. DOI: https://doi.org/10.1029/2004GL019804.

Vos, Rob, Margarita Velasco, and Edgar Labastida (1999). "Economic and social effects of "El Niño" in Ecuador, 1997-8." In: *ISS Working Paper Series/General Series* 292, pp. 1–55.

Wang, Chunzai and J. Picaut (2013). "Understanding Enso Physics-A Review." In: *Earth's Climate*. American Geophysical Union, pp. 21–48.

Weaver, J. T. (Jan. 1971). "The General Theory of Electromagnetic Induction in a Conducting Half-Space." In: *Geophysical Journal International* 22.1, pp. 83–100. DOI: 10.1111/j.1365-246X.1971.tb03584.x.

Wilhite, Donald A, DA Wood, and SJ Meyer (1987). "The societal impacts associated with the 1982-83 worldwide climate anomalies." In: National Center for Atmospheric

Research. Chap. 13: Climate-related impacts in the United States during the 1982-83 El Niño, pp. 75–78.

Winch, D. E. (1970). "Geomagnetic Lunar Partial Tides." In: *Journal of geomagnetism and geoelectricity* 22.3, pp. 291–318. DOI: 10.5636/jgg.22.291.

Winch, D. E. and Paul Harry Roberts (1981). "Spherical harmonic analysis of geomagnetic tides, 1964-1965." In: *Philosophical Transactions of the Royal Society of London. Series A, Mathematical and Physical Sciences* 303.1473, pp. 1–104. DOI: 10.1098/rsta.1981.0193.

Wollaston, C (1881). "Discussion of the paper by AJS Adams "earth Currents"(2nd paper)." In: *J. Soc. Telegr. Eng. Electricians* 10, pp. 50–51.

Woolf, Harold M (1968). *On the computation of solar elevation angles and the determination of sunrise and sunset times*. National Aeronautics and Space Administration.

Wright, J., A. Colling, and D. Park (1999). *Waves, tides and shallow-water processes*. Vol. 4. Gulf Professional Publishing.

Young, F.B., H. Gerrard, and W. Jevons (1920). "XIII. On electrical disturbances due to tides and waves." In: *The London, Edinburgh, and Dublin Philosophical Magazine and Journal of Science* 40.235, pp. 149–159. DOI: 10.1080/14786440708636105.

Zheng, Zeyu, Yang Fu, Kaizhou Liu, Rui Xiao, Xiaohui Wang, and Haibo Shi (2018). "Three-stage vertical distribution of seawater conductivity." In: *Scientific reports* 8.1, pp. 1–10.

Zweng, Melissa M, James R Reagan, John I Antonov, Ricardo A Locarnini, Alexey V Mishonov, Timothy P Boyer, Hernan E Garcia, Olga K Baranova, Daphne R Johnson, Dan Seidov, et al. (2013). "World ocean atlas 2013. Volume 2, Salinity." In: *NOAA Atlas NESDIS*.

Es gibt viele Dinge zum Promotionsprozess zu sagen.
Wenige davon lassen sich in ihrer Gänze begreifen,
wenn man den Prozesse nicht selbst durchlebt hat.

DANK

Nun, da sich die Promotion ihrem Ende nähert, ist es Zeit einen Schritt zurück zu treten und die letzten Jahre Revue passieren zu lassen. Ich wäre vermutlich nie an diesem Punkt angelangt ohne die immense Unterstützung, die ich erfahren habe. Ich möchte mich an dieser Stelle aufrichtig bei allen unterstützenden Personen bedanken. Wohlwissend, dass eine namentliche Nennung aller Personen nicht möglich ist, möchte ich mich doch bei einigen persönlich bedanken.

Lieber Maik, ich danke dir, meinem Doktorvater, zu allererst dafür, dass Du diese Reise zusammen mit Jan und mir angetreten bist. Ich weiß sowohl das entgegengebrachte Vertrauen als auch die Freiheit mich in meinem eigenen Tempo und zu meinen eigenen Bedingungn weiterentwickeln zu dürfen zu schätzen. In angedenk der verstrichenen Zeit hoffe ich, dass dein Vertrauen in mich letzten Endes berechtigt war und die strapazierte Geduld belohnt wurde.

Lieber Jan, als fachlicher Betreuer gibt es viele große und kleine Dinge für die ich Dir danken möchte. Neben der Bereitschaft mich beim Promotionsprozess zu begleiten und mich in das Handwerk der Wissenschaffenden einzuführen, danke ich Dir für die Bereitschaft klare Gedanken aus meinen wirren Worten zu formen und immer deutliche Worte zu finden, wenn es notwendig war. In besonderer Erinnerung wird mir dein Einsatz für mich bleiben, als der Editor meines ersten Papers seine Kompetenzen überschätzt hat und mir die Erfahrung und das Vertrauen gefehlt hat es selbst zu tun.

Milena, after all the years in our office at the end of the corridor and all the shared successes and failures, I am dearly happy we went this part of the journey together. You treated me and my entire family to many serbian

specialties. Thank you. Bog te jebo, I am excited to see where the winds will take you.

Liebe Erdsystem-Modellierungssektion des GFZ, ich werde mich auch in Zukunft gern an euch zurück erinnern. An die guten Gespräche mit und die große Unterstützung durch Veronika und Dana. Die gemeinsame Zeit mit den anderen Promovierenden. Jorge, Chris, Carina, Lea, Cate, Roman, Tobias, Aaron und Peter, einige haben es schon hinter sich und andere noch vor sich, meine Promotionszeit wäre ohne euch um viele schöne Momente ärmer gewesen. Das gleiche gilt auch für die anderen Wissenschaftskollegen, wie die in den Kreis der Doktoranden adoptierte Meike, das Rollenmodell für den Einklang von Familie und Forschung Robert, Henryk den Waldläufer und Experten für die Prozessierung realer Satellitenbeobachtungen, den Chorknaben Volker, Alexey mit einer unnachahmlichen Gabe die wichtigen Fragen zu stellen und noch viele weitere. Auch dir Ronny bin ich zu Dank verpflichtet. Nicht nur für deine Unterstützung als Systemadministrator, sondern auch für die intensive Zeit im gemeinsamen Büro, während der ich vieles aus einer neuen Perspektive kennenlernen durfte.

Allen die mir geholfen haben die zweite Luft zu finden, als die Pandemie mit häuslichen Kinderbetreuung und neuem Tätigkeitsfeld den Fortschritt der Promotion deutlich gebremst haben, schulde ich eingen großen Dank. Dazu gehören meine neuen Kolleg:innen im allgemeinen und Anke, Annett, Rose, Lydia und Pia im speziellen. Gleiches gilt außerdem auch für dich Christian. Du hast wahrscheinlich das größte Interesse an der Arbeit und ihrem Fortschritt gezeigt und maßgeblich zum Fortkommen auf den letzten Metern beigetragen.

Besonderer Dank geht an meine gesamte Familie, dass sie mich zu dem gemacht haben, was ich heute bin. Mutsch, Vaddern, Flori, Omsen, Opsen, Tantchen, Maik und Sophie ohne euch wäre ich sicherlich kein Träumer geworden. Nun da sich das vorhaben dem Ende nähert, kann ich die Last der hohen Erwartungen ablegen. Ich habe mit dem Bären gerungen und bin siegreich zurückgekehrt um davon zu berichten. Vermutlich hätte ich einiges anders gemacht, hätte ich gewusst worauf ich mich einlasse.

Liebe Pauli, dir kann ich gar nicht genug danken. Angefangen mit dem von Urmel und Gunni angeführten Team von zusätzlichen Unterstützern, über unzählige Stunden die du mir freigehalten hast um zu denken, arbeiten und schreiben, bis hin zur Liebe und Fürsorge die du mir entgegen gebracht hast, gibt es vieles wofür ich dir an dieser Stelle danken möchte. Inwiefern Kinder die Dauer des Promotionsprozesses verkürzen können, stelle ich an dieser Stelle anheim. Wichtig ist, ohne dich wäre es für mich unmöglich gewesen unsere kleine Familie zu gründen und die Promotion zum Abschluss zu bringen. Danke.

Zu allerletzt danke ich meinen Kindern Frieda und Rosa, welche genau wie ihre Mutter viel Geduld und Verständnis aufgebracht und auf viel gemeinsame Zeit verzichtet haben. Mein Abschluss ist unser kollektiver Erfolg. Oder wie es an andere Stelle besser gesagt wurde: *Ohana* means family. Family means nobody gets left behind or forgotten.

EIDESSTATTLICHE ERKLÄRUNG

Hiermit erkläre ich an Eides statt, dass die vorliegende Arbeit alleinig von mir persönlich unter der Verwendung der angegebenen Quellen und Hilfsmittel angefertigt wurde. Alle Zitate wurden von mir als solche gekennzeichnet. Ein Promotionsverfahren wurde weder zu einem früheren Zeitpunkt, einer anderen Hochschule oder in einem anderen Fachbereich beantragt.

Berlin, 9. Februar 2022

Johannes Petereit